A Feasibility Study: Positioning a Lenlset Array Above a Target Using MEMS to Specify Three or Four Degrees of Freedom

Feras S. J. Michael

Department of Electrical and Computer Engineering
McGill University
Montreal, Canada
August, 2000

This thesis is submitted to the Faculty of Graduate Studies and Research in partial fulfillment of the requirements of the degree of Master of Engineering.

0-612-70243-X

Abstract

A feasibility study investigating the development of an automated Micro-Electro-Mechanical System (MEMS) permitting the accurate placement of a lenslet array in three or four degrees of freedom will be conducted. In particular, various MEMS actuators will be analyzed and published actuation strategies will be studied to ultimately develop MEMS that can support a 32.3 mg lenslet array. In addition to withstanding the optical element's weight, the MEMS will be required to optimally align the lenslet array with a Photo Detector (PD) or a Vertical-Cavity Surface-Emitting Laser (VSCEL) in the traditional X, Y, Z, and θ (rotational) directions. In addition, the actuators' controlling signals will be delivered by on-chip electronic and optical feedback mechanisms by using the already present photo detectors and built-in alignment schemes.

Sommaire

Une étude de faisabilité recherchant le développement d'un Système Micro-Électro-Mécanique (Micro-Electro-Mechanical System, MEMS) automatisé qui permettrait le placement précis d'une matrice de lentille en trois ou quatre degrés de liberté sera entrepris. En particulier, une analyse de plusieurs actionneurs MEMS ainsi que des stratégies d'actionnement seront étudiées afin d'éventuellement développer un MEMS qui supporterait une matrice de lentille ayant une masse de 32.3 mg. En plus de résister a la masse de l'élément optique, le MEMS sera requis de l'aligner de façon optimal avec un photo-détecteur (PD) ou un Laser a Émetteur de Surface a Cavité Verticale (Vertical-Cavity Surface-Emitting Laser, VSCEL) dans les orientations traditionnelles X, Y, Z et θ (en rotation). En plus, les signaux controlant les actionneurs lui seront livrés par des mécanismes de retour d'information électronique et optiques en utilisant les photo-détecteurs et les systèmes d'alignment optiques déja présents.

Acknowledgments

I would like to dedicate this thesis to the memory of my dear Nana Mireille. My Judoo Habib and her raised me for the first four years of my life in Basrah, Iraq. I am who I am thanks to them and I love them dearly. My loving parents Samir and Gloria and sister Noor have supported and encouraged me from the beginning with my university education at McGill. I would also like to thank my loving fiancée Sema for encouraging me when things got tough towards the end with all the testing and writing converging upon me.

I would also like to thank my supervisor Dr. Andrew Kirk for giving me the opportunity to join the Photonic Systems Group despite my performance as an undergraduate. Thanks for taking the group towards MEMS because I have no found what I truly love...a 50-50 split between Mechanical and Electrical Engineering disciplines.

I especially want to acknowledge the confidence Michael Ayliffe and David Rolston placed in me. I will always remember the work we did together and my home away from home...the Annex. I would like to mention the encouragement and support of all PSG members (past and present) with whom I have had the privilege to work. Guillaume Boisset was an inspiring TA who was the first to invite me for a tour of the lab. That positive attitude was only fueled by Dr. David Plant's enthusiasm as a teacher.

I have had the distinct honor of working with some of the finest engineers and people. I new that I would love this experience when I did my project lab with the PSG and I was right. Should our paths cross once again, I already look forward to working with all of you in the future.

My sincerest thanks and love to one and all.

This work was supported by CITR (the Canadian Institute for Telecommunications Research) and the McGill University Graduate Faculty.

Feras S. J. Michael I

ABSTRACT II

SOMMAIRE III

ACKNOWLEDGMENTS IV

1 Introduction 1

1.1 MOTIVATION 1

1.2 OUTLINE 3

1.3 REFERENCES 5

2 General System Specifications 6

2.1 MEMS IN PHOTONICS: A BRIEF HISTORY 6

2.2 SYSTEM LEVEL DESCRIPTION 9

2.3 REQUIREMENTS FOR MAINTAINING AND ACHIEVING OPTICAL ALIGNMENT 13

2.4 REFERENCES 18

3 Fabrication Processes 20

3.1 INTRODUCTION 20

3.2 HIGH ASPECT RATIO MACHINING (HARM) 21

3.2.1 Bulk Micromachining *21*

3.2.2 Deep Reactive Ion Etching (DRIE) *23*

3.2.3 "LIthographie Galvanoformung Abformung" (LIGA) *24*

3.3 SURFACE MICROMACHINING 26

3.3.1 Multi-User MEMS Process (MUMPs) *27*

3.3.2 Sandia Ultra-planar Multi-level MEMS Technology (SUMMiT) *28*

3.3.3 Integrated MicroElectroMechanical Systems (IMEMS) *29*

3.4 CORNER COMPENSATION 30

3.5 MICROSCOPIC WEAR IN MEMS 31

3.6 STICTION AND MEMS 32

3.7 REFERENCES 33

4 Actuation Methods 38

4.1 INTRODUCTION 38

4.2 SCALING OF FORCES 39

4.3 LATERAL ACTUATION TECHNIQUES 39

4.3.1 Electrostatic Actuation *39*

4.3.1.1 Comb Drive Actuator (CDA) 39

4.3.1.2 Scratch Drive Actuator (SDA) 42

4.3.2 Thermal Actuation *43*

4.4 VERTICAL ACTUATION TECHNIQUES 48

4.4.1 Electrostatic Actuation *48*

4.4.2 Thermal Actuation *50*

4.4.2.1 Backward Bending Thermal Actuator 50
4.4.2.2 Forward Bending Thermal Actuator 51
4.5 REFERENCES 57
5 The Selection of a Fabrication Process and an Actuation Scheme 62
5.1 INTRODUCTION 62
5.2 SCHEMATIC OF THE PACKAGED LENSLET POSITIONING MEMS 62
5.3 FABRICATION PROCESSES 63
5.4 ACTUATION SCHEMES 63
5.4.1 Lateral and Rotational Actuation 64
5.4.2 Vertical Actuation 66
5.5 REFERENCES 66
6 Decoupled Actuation Analysis 67
6.1 INTRODUCTION 67
6.2 LATERAL MOTION IN THE X-Y PLANE 67
6.3 ROTATIONAL MOTION (Θ) IN THE X-Y PLANE 74
6.4 VERTICAL MOTION (Z) 77
6.5 REFERENCES 83
7 Lenslet Positioning Stages 84
7.1 THE [X - Y – Θ] STAGE 84
7.1.1 Discussion 84
7.1.2 Implementation and Control Strategy 85
7.2 THE [X - Y - Θ – Z] STAGE 87
7.2.1 Discussion 87
7.2.2 Implementation and Control Strategy 87
7.3 PACKAGING AND ASSEMBLY 89
7.3.1 Introduction 89
7.3.2 The Package and its Components 90
7.3.3 Package Assembly Process 91
7.4 REFERENCES 93
8 MEMS: Current Needs and Future Challenges 95
8.1 MOTIVATION 95
8.2 COMMERCIALIZING MEMS 96
8.3 REFERENCES 98
9 Conclusions 100

1 Introduction

1.1 Motivation

Over the past three decades, certain research efforts have tended towards increasing data transmission rates, through fiber optic links, by using methods such as Dense Wavelength Division Multiplexing (DWDM). An alternate approach to interlacing signals along a common link is to optically couple parallel fibers to a Surface-Emitting Laser array (SEL) [1] as shown in Figure 1.1 below. Dense parallel optical beam interconnects can be achieved by using large-scale integration of SELs. However, if coupling efficiencies greater than 35% are to be obtained discrete optical elements will have to replace the passive guide holes and optical fibers used in [1] to eliminate the signal-to-fiber juncture. In so doing, a parallel Free-Space Optical Interconnect (FSOI) will be established. With this scheme, correctly aligning the array of optical links becomes more of an issue than exhausting the capacity of a single link based system [2].

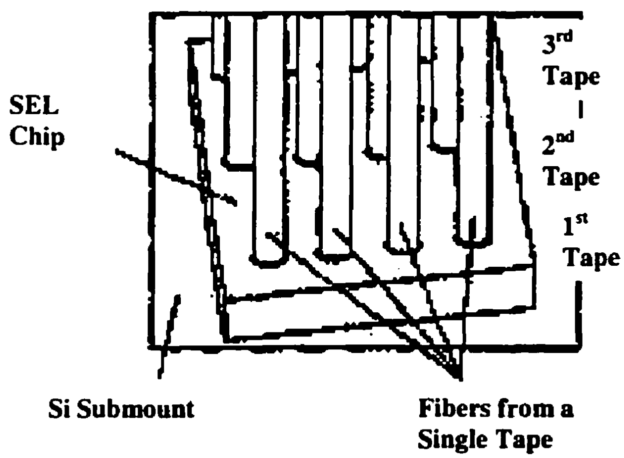

Figure 1.1: Schematic drawing of optical fibers inserted into guiding holes formed on the backside of the SEL array chip.

Within this FSOI, the Vertical-Cavity Surface-Emitting Laser (VCSEL) array outputs inherently divergent circular beams of light. Consequently, it must be coupled and guided by optical elements, such as a bulk lens or microlens array, to preserve the data stream's integrity. A low-cost bulk lens would simultaneously collimate hundreds of independent parallel connections [3]. Similarly, an array of microscopic lenses, known as lenslets, could accommodate high beam densities as shown by their applications in [4] and [5] and demonstrated in Figure 1.2. Lenslet arrays distinguish themselves from their macroscopic counterparts in more than one way.

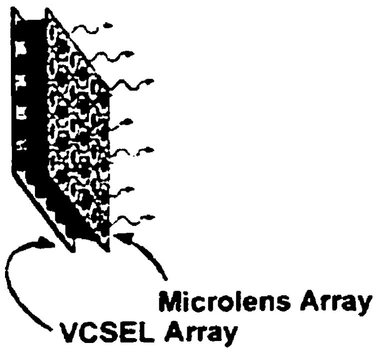

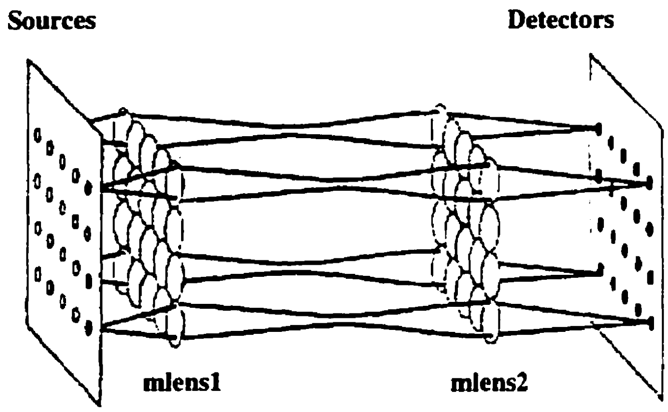

Figure 1.2: 3-D [7] and sectional views [6] of a typical VCSEL-Lenslet array pair.

Firstly, individual optical relay systems are provided for each I/O window, or pixel, rather than funneling the beams through a single optical element. Secondly, unlike bulk lenses, a high Space Bandwidth Product (SBWP) is not necessary because resolution is provided only locally in the vicinity of the lenslet and VCSEL source where it is needed. In addition, the short focal length and small diameters of the microlenses may allow for a compact design [6].

Despite these perhaps useful differences, the primary disadvantage is the intolerance to misalignment microlenses exhibit in every design, be it mechanical or optical in nature. The misalignment tolerance of an optical element is a specification that has a direct impact upon the precision with which it must be initially positioned prior to being used efficiently.

One way of increasing an optical system's immunity to misalignment is through the use of spatial redundancy [8, 9]. It effectively increases a FSOI's misalignment tolerance by transmitting the same data stream over more than one relay. Consequently, the probability of establishing at least one properly aligned beam relay increases.

Another possible solution to the inadequate misalignment tolerance, inherent to lenslet arrays, is using Microelectromechanical Systems (MEMS) to optimally align the lenslet array's position relative to the underlying VCSEL array. A new alignment strategy is developed using this hybrid technique. It involves firstly manually depositing the lenslet array, onto a MEMS-populated substrate, to within 10.0 μm of its optimal location. Next, the MEMS will take over and determine the final position of the array via optical feedback generated by on-chip control mechanisms. The objective is to design automated optical MEMS that can support the weight of an optical element, namely a lenslet array, while positioning it to within 0.1 μm of its optimal location.

1.2 Outline

In the process of fulfilling the above mentioned goal, this thesis will inform the reader about the quickly evolving field of Microelectromechanical Systems while establishing an understanding of the different stages involved in the design of MEMS. Micro- Electro-Mechanical Systems may comprise a collection of devices or refer to a single structure, which can range from an actuator to a pressure sensor. Given the large number of possibilities, the contents of this thesis will revolve around a feasibility study of the MEMS described in the last section.

The acronym for Micro- Electro-Mechanical Systems, "MEMS", was only recently suggested by Professor Roger Howe in 1989 at a Micro-Tele-Operated Robotics Workshop in Salt Lake City after an hour of heated debate [10]. In the same spirit a minor note with regards to the terminology must be made, before proceeding. The reader should be aware that the MEMS acronym might stand for Microelectromechanical **Systems** or Microelectromechanical **System**. These two possibilities are used interchangeably in literature and the same tendency will be observed throughout this thesis.

Given the unavoidable lack of precision mentioned earlier and the presence of an increasingly demanding telecommunications market, the need for a commercially viable and reliable automated alignment solution is immediate. MEMS answer that need by offering powerful actuators that cost no more than a conventional microchip to produce.

The discussion will commence with a brief history of MEMS, Chapter 2, within the field of Photonic Systems in order to provide the reader with a feel for the field's novelty. Next, an overview of the system under study is presented followed by the optical alignment specifications that the MEMS must satisfy if they will be useful. The role of MEMS actuators in achieving an alignment that respects the aforementioned alignment tolerances is then justified.

Prior to investigating the details of various actuation strategies, two fundamentally distinct MEMS fabrication approaches are reviewed in Chapter 3. In so doing, an appreciation for the manufacturing related limitations constraining a given design can be acquired. In Chapter 4, different methodologies and actuation strategies for MEMS actuators are presented via analysis. The actuation stratagems and mechanisms for both lateral and vertical are discussed; electrostatic and thermal actuation schemes in particular. At this point, a helpful foundation will have had been laid out and ready to be used. Thus, in Chapter 5 a fabrication process and a suitable number of actuation schemes will be chosen amongst those studied. The selections, which are motivated by a common desire to efficiently position the lenslet array, are justified herein.

Following the identification of a fitting actuator, a quantitative description of each of the resulting devices is noted in Chapter 6. The latter is accomplished by way of theoretical and experimental. Firstly the X-Y motion will be examined followed by rotational motion, θ, and lastly, motion in the vertical Z-direction.

The latter three uncoupled actuators are brought together to form two separate MEMS that control three or four degrees of freedom, respectively. The proposed lenslet positioning Microelectromechanical Systems that result are examined in Chapter 7. A decision concerning the feasibility of the two MEMS introduced will conclude each sub-section. Finally, Chapter 8 presents current and future challenges faced by the industry with respect to the fabrication and reliability of MEMS. In Chapter 9, a review of the justifying arguments dictating the viability of the two proposed Microelectromechanical Systems are be stated followed by concluding remarks.

1.3 References

1. K. Matsuda, T. Chino, T. Yoshida, Y. Kobayashi, and K. Hatada, "Passive Optical Alignment of Stacked Multi-Fiber Tapes to a Two-Dimensional Surface-Emitting Laser Array", IEEE, IEDM'95, pp.587-590, 1995.
2. V. N. Morozov, Y.-C. Lee, J. A. Neff, D. O'Biren, T. S. McLaren, and H. Zhou, "Tolerance Analysis for Three-Dimensional Optoelectronic Systems Packaging", Journal of Optical Engineering, Vol. 35, No. 7, pp. 2034-2044, July 1996.
3. James Gourlay, Tsung-Yi Yang, Julian A.B. Dines, John F. Snowdon, and Andrew C. Walker, "Development of free-space digital optics in computing", Computer, Vol. 31, Issue 2, pp. 38-44, February 1998.
4. A.G. Kirk, F.K. Lacroix, M.H. Ayliffe, E. Bernier, D. F-Brosseau, M. Chateauneuf, B. Robertson, F.A.P. Tooley, and D.V. Plant, "A multistage free-space optical interconnect for backplane applications: implementation issues", Lasers and Electro-Optics Society Annual Meeting, 1998, IEEE. Vol.: 2, 1998, pp. 149 –150.
5. E.M. Strzelecka, D.A. Louderback, K. Bertilsson, B.J. Thibeault, M. Mondry, and L.A. Coldren, "Free-Space Optical Link Realized with Microlensed Components" 1997 Electronic Components and Technology Conference, pp. 376-381.
6. F. B. McCormick, F. A. P. Tooley, T. J. Cloonan, J. M. Sasian, H. S. Hinton, K. O. Mersereau, and A. Y. Feldblum, "Optical Interconnections Using Microlens Arrays", Optical and Quantum Electronics, Vol. 24, pp. S465-S477, 1992.
7. H.-L. Chen, D. Francis, T. Nguyen, W. Yuen, G. Li, and C. C.-Hasnain, "Collimating Diode Laser Beams from a Large-Area VCSEL-Array Using Microlens Array", IEEE Photonics Technology Letters, Vol. 11, No. 5, pp.506-508, May 1999.
8. Frank A. P. Tooley, "Challenges in Optically Interconnecting Electronics", Journal of Quantum Electronics, Vol. 2, No. 1, pp. 3-13, April 1996.
9. M. Mony, M. Salzberg, P. Popescu, E. Bernier, E. Bisaillon, D.V. Plant, and A.G. Kirk, "1Gb/s, 9×1 optical receiver array, for an adaptive redundant interconnect system, using NT25 technology", OC'2000. [Accepted for publication].
10. An Introduction to Microelectromechanical Systems Engineering, Nadim Maluf, Microelectromechanical Systems Series, Artech House, Boston, p. xiii, 2000.

2 General System Specifications

2.1 MEMS in Photonics: A Brief History

During a lecture on the 26th of December 1959, Richard P. Feynman asked the following question, "Why cannot we write the entire 24 volumes of the Encyclopaedia Britannica on the head of a pin?" [1]. The intuitionist and physicist posed this at an annual meeting of the American Physical Society while hypothesizing about a field "in which little has been done, but in which an enormous amount can be done in principle" [1]. Mr. Feynman was planting the seeds of a novel research area that has become known as the field of MEMS. Much like the transistor, Microelectromechanical Systems have recently been described as a disruptive technology that have the potential to radically change the way things are done [2].

This revolutionary technology is finding niches in numerous industries that range from microscopic locking devices [3] to artificial retinas [4, 5]. Table 2.1 on the next page lists a few more areas of interest along with their respective predicted demand. One of the earliest indications of a partnership between the realms of Micromechanics and Photonics was cited in work done in 1985 by Venkatesh and Culshaw [7]. Their work described the use of light to optically induce vibrations in an otherwise immobile micromachined silica structure. Soon thereafter, Fatah et al. proposed the idea of integrating such silicon micromechanical resonators into a fibre optic system [8]. The same research group went on to develop an all fibre-optic microresonator sensor system the following year [9]. Soon thereafter, they achieved mechanical resonance via optical feedback by emulating a Fabry-Pérot cavity within a fiber optic loop [10].

Year	Automotive ($ 000,000)	Medical ($ 000,000)	Information Technology & Industrial ($ 000,000)	Military & Aerospace ($ 000,000)	Total ($ 000,000)
1994	255.7	129.5	438.3	49.1	872.5
1995	298.0	146.1	459.0	54.8	957.9
1996	355.0	164.4	492.8	62.2	1074.3
1997	419.0	187.0	527.0	71.6	1204.6
1998	491.5	216.7	575.3	79.6	1363.1
1999	562.0	245.7	645.9	95.8	1549.4
2000	645.7	291.3	733.3	110.7	1781.0
2001	758.5	354.8	836.0	133.3	2082.5
2002	879.6	444.7	995.1	156.9	2476.3
2003	1019.0	562.9	1222.0	176.7	2980.4
2004	1172.0	716.0	1514.0	202.7	3604.5
CAGR	16%	21%	16%	16%	17%

Table 2.1: Analysis and Forecast of U.S. Markets (in Millions of U.S. Dollars) [6]

The communications industry has become the primary beneficiary of the current MEMS research. This fact is demonstrated in the field of telecommunications where MEMS variable attenuators [11] and optical switches [12] are being realized fundamentally through the use of micromirrors. Despite the success of the latter at transmitting data streams, digitally controlled micromirrors fulfill a more entertaining role as part of Digital Cinema (D-cinema). This device is a collection of over 1.3 million aluminum micromirrors [13]. Figure 2.1 shows the construction and sub-components of two Deformable Mirror Devices (DMD™) [14].

Texas Instruments

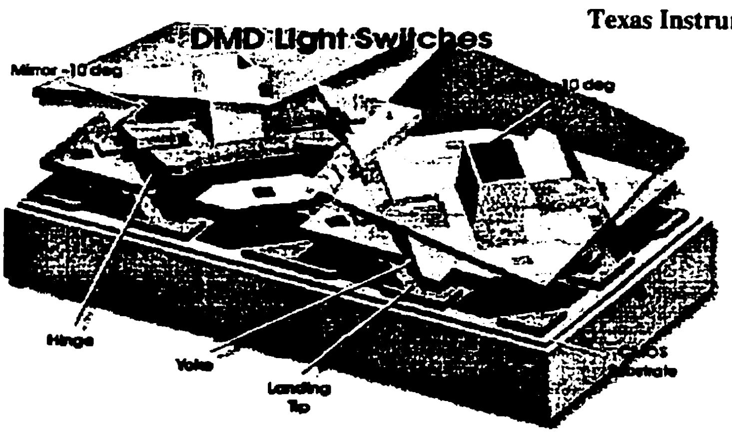

Figure 2.1: Illustration of a single DMD™ pixel in its actuated state. [15].

According to a recent study, MEMS involvement in other areas will continue to grow as shown in Figure 2.2 below.

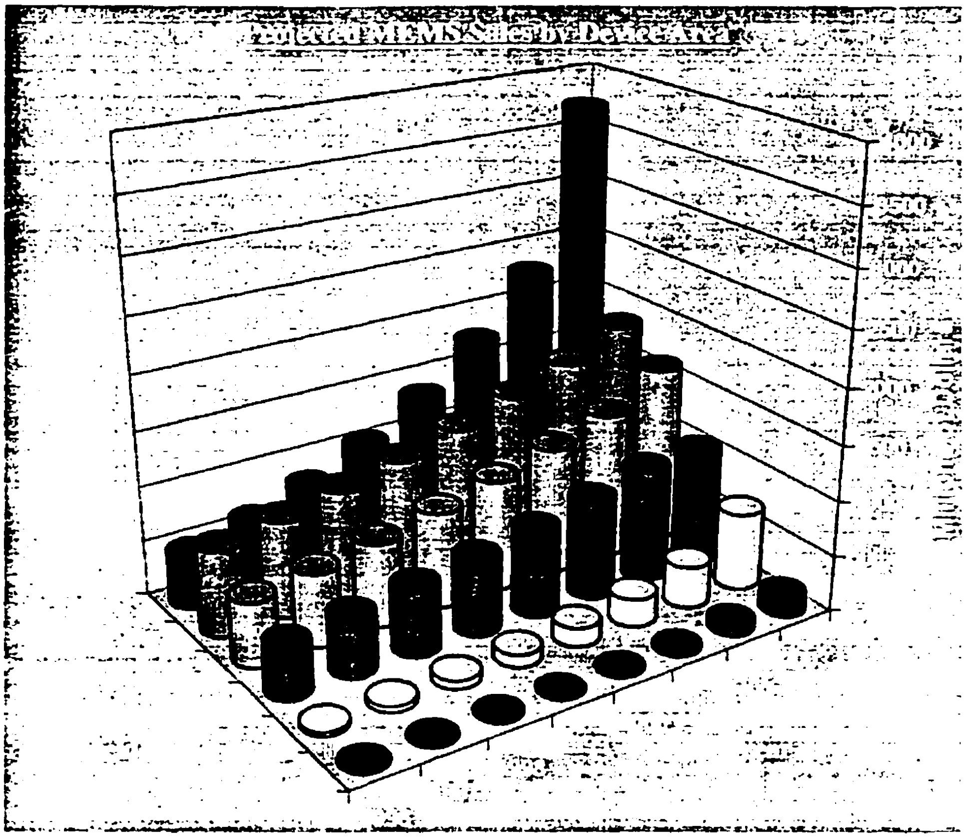

Figure 2.2: Estimated device sales by technological area based upon [16].

Micromirrors are a very useful component of many photonic applications but they exhibit a fundamental limitation in so far as their travel distance is concerned, because of the actuation strategy used [17]. As a result, the design and construction of micromirror-based MEMS is not a trivial matter [18].

The key to building any useful MEMS is the precision with which the system can be actuated. An in-plane X-Y-Z stage that can position a laser beam with a resolution of 1.0 μm upon an adjacent diffractive microlens was built by Wu et al. [19]. A feasibility study of an out-of-plane lenslet positioning system with a comparable accuracy will now be conducted.

2.2 System Level Description

The lenslet array was designed to collimate light, originating from a VCSEL beneath it, onto a Photo Detector (PD) above it on an independent chip. The mirrored situation was also accounted for whereupon light is focused by the microlens onto a PD beneath it [20]. These two scenarios are illustrated in Figure 2.3 below. A representative drawing of the lenslet, or microlens array, around which the design of this system is centered is shown in Figure 2.4.

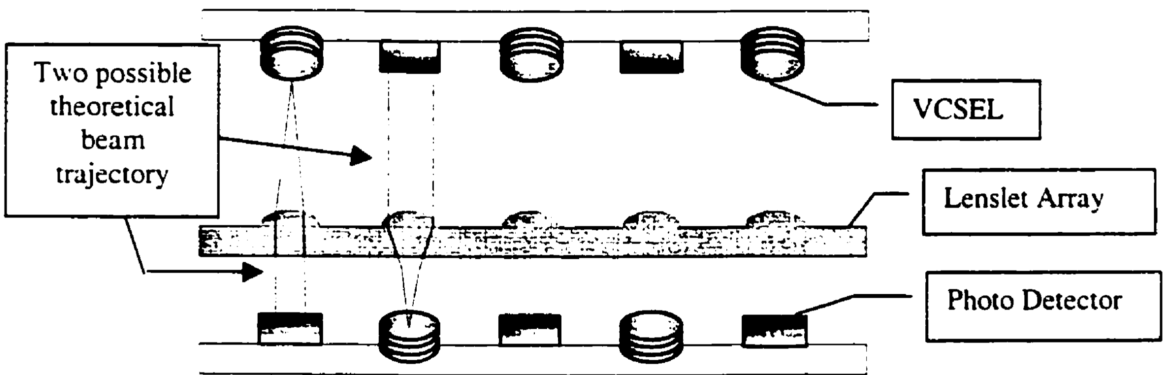

Figure 2.3: Schematic of the lenslet array's theoretical performance requirements.

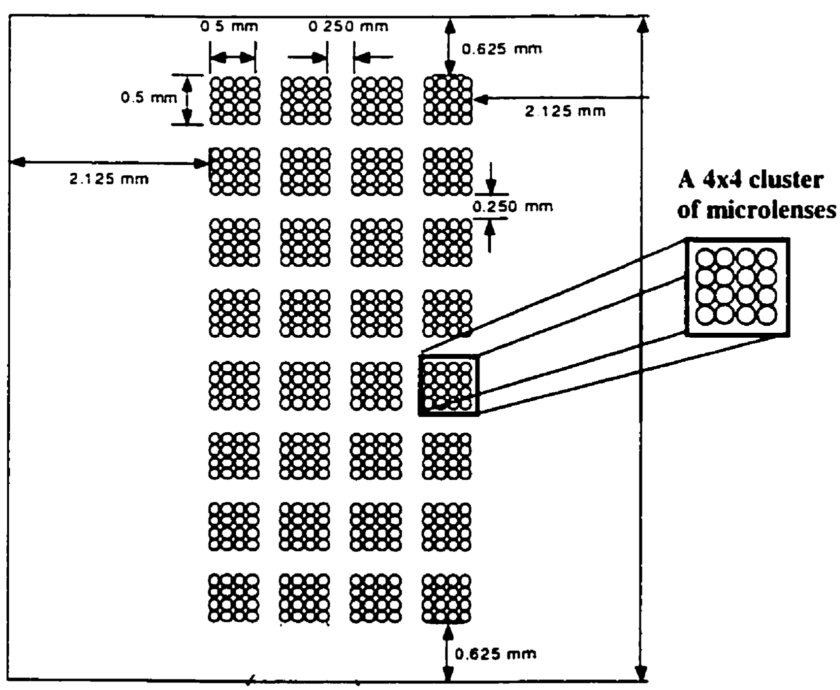

Figure 2.4: Lenslet or Microlens Array schematic [21].

The lenslet array was fabricated using thermal reflow of photoresist whereby cylindrical islands of photoresist are melted and surface tension forms the molten resist into a spherical shape. The primary disadvantage of this process is the lack of control over the final shape of the surface. Nevertheless, it was selected due to lower production costs. Since the diameter of the lens will influence its focal length, insuring control of the lens' shape would have lead to a calculated diameter and hence a predictable focal length [22].

The lenslet array possesses many features that enable different alignment schemes, which will be discussed in the next section. Table 2.2 lists the technical specifications for the lenslet array motivating this design.

Lens Type	High NA / Fast Refractive
Array Size	8x 4array of 4 x 4 clusters
Cluster Pitch	750 μm
Lens Pitch (within a cluster)	125 μm
Diameter	120 μm
Focal Length	250 μm
Surface Profile	Spherical
f / #	2.0
Index of Refraction (at 850 nm)	1.452
NA ($n_o \sin\theta_{ma}$)	0.25
Material	Fused Silica
Substrate Thickness	300 μm

Table 2.2: Microlens Specifications

The primary feature of the lenslet array that influenced the design of the MEMS was its mass. The dimensions of the microlens array were 3.0 mm in width and 6.0 mm in length. With a thickness of 300 μm, it had a volume of 5.40 x 10^9 μm^3. A mass of 32.3 mg was calculated using a density of 2200 kg/m^3 for fused silica [23]. It should be noted that Figure 2.4 is an authentic representation of the lenslet, despite the noticeable difference between it and the optical element layout of Figure 2.5 where a 6 x 4, instead of an 8 x 4, array is drawn.

In order to appreciate the task of aligning the lenslet with the underlying PD and VCSEL arrays, a schematic of the positioning system is presented in Figure 2.5. The lenslet array, containing the spherical microlenses, is placed upon a foundation, which is composed of three other major components. The optical system's base consists of a spacer and the substrate, which are fixed to one another. Interlaced columns of photo detectors and VCSELs are located on the substrate as shown in Figure 2.5. Lastly, the MEMS are located on the spacer top surface.

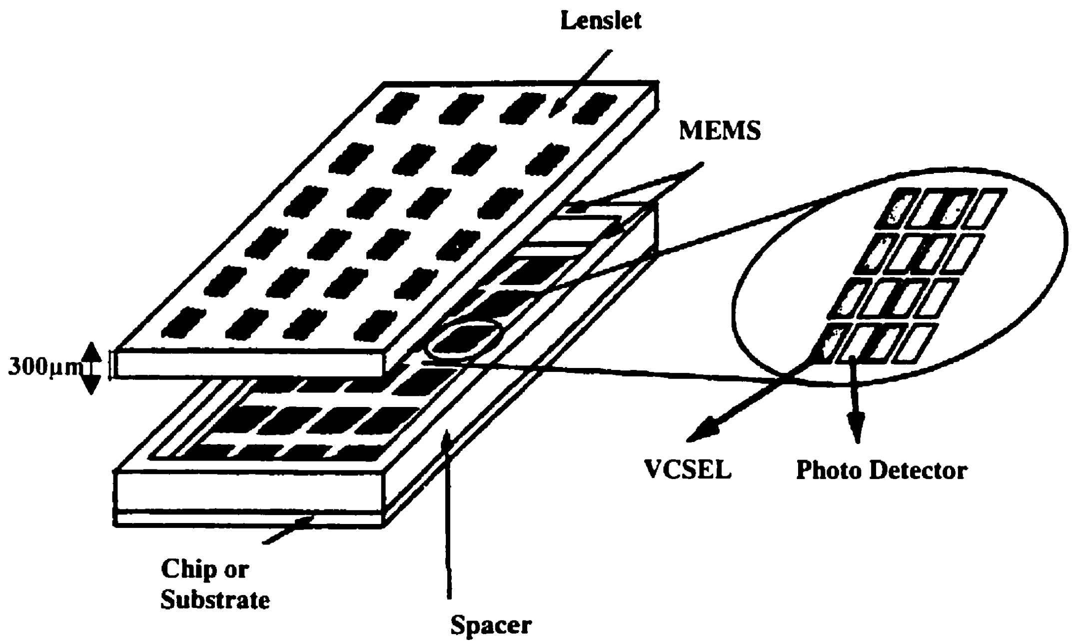

Figure 2.5: A representative schematic of the lenslet positioning system.

The displacement resolution of MEMS, which is 0.1 μm, makes them good candidates for the demanding alignment task. However, MEMS cannot comfortably elevate the 32.3 mg lenslet more than 10 μm above the substrate's surface without consuming a large amount of power or being permanently deformed due to reasons that will be discussed further on. The need for a vertical displacement larger than that producible by the MEMS is due to the optical characteristics of the pre-designed microlens array.

Theoretically, the lenslet array's ideal vertical position (VP) is obtained from the following equation,

$$f_A = \left({l_1}/{n_1} \right) + \left({l_2}/{n_2} \right)$$
$$f_A = \left({l_1}/{n_1} \right) + VP \qquad \text{Equation 2.1}$$

where l_1 and l_2 are the optical path lengths (OPL) in mediums 1 and 2, which are fused silica and air, respectively. l_1 represents the lenslet's thickness. The focal length of the microlens in air is denoted by f_A and equals 250 μm. n_1 and n_2 are the indices of refraction of the mediums they describe. The effective OPL in air of the microlens can be determined by substituting the values for l_1 and n_1 from Table 2.2. After isolating *VP*, a value of 43.39 μm is obtained. Therefore, an initial lenslet elevation of at least 40.0 ± 2.0 μm is desired.

To provide the MEMS with a higher point of reference relative to the substrate's surface, a calculated number of layers that are provided by the fabrication process could be used to form post-like structures. Using otherwise releasable layers would reduce the number of layers available to the design. The MEMS that will be designed are involved and require as much versatility as possible to construct actuators. In addition, the thickness of each layer, which are process-specific, do not satisfy the 40.0 ± 2.0 μm initial elevation needed. Creating a cavity during the fabrication of the opto-electronic chip would complicate the process, increase costs, and possibly compromise the performance of any already built structures. Hence it too is not an acceptable solution.

By the same token, the chip can be fabricated inside a cavity within the substrate or inside a separately fabricated bushing. A post-fabrication nitride layer, with an appropriate thickness and hole dimension, could be placed on top of the opto-electronic device in order to emulate a true cavity. To the same end, a thicker nitride layer could be placed beneath the MEMS polysilicon substrate to implement the desired pseudo-cavity. The latter two alternatives can be considered only if the chosen fabrication process permits the variation of this parameter.

However, the needed elevation could be provided an independently machined rectangular spacer. Although it would incur further packaging needs, it would be the only plausible option should the two previously mentioned ones be inaccessible. Such assembly and packaging issues will be developed further in section 7.3. When this important initial condition is satisfied and the lenslet is placed upon the pseudo-cavity, the MEMS will take over and complete the alignment task.

2.3 Requirements for Maintaining and Achieving Optical Alignment

The need for an alignment system was motivated by the onset of one or more of the undesirable scenarios described in Figure 2.6. To avoid any preliminary positioning errors, the lenslet was made rectangular and optically and geometrically symmetric. Traditionally, mechanical structures, such as dowel pins, are used to fix or eliminate degrees of freedom. In this case, a few macroscopic characteristics of the microlens array and the optoelectronic chip facilitated its initial placement by the user. In so far as the system under study was concerned, four mutually independent optically based alignment schemes exist.

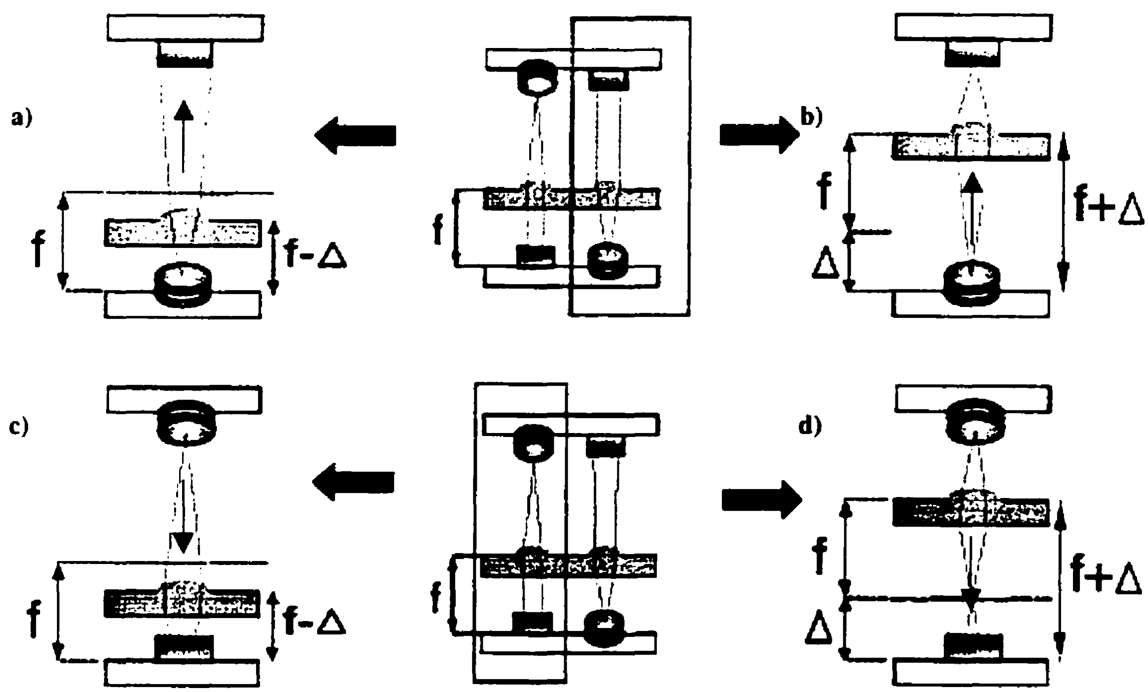

Figure 2.6: Four possible misalignment scenarios. In (a) and (c) the lenslet is behind it's focal plane whereas in (b) and (d) it is in front of it.

The majority of alignment features were located at the opposing edges of the opto-electronic chip as shown in Figure 2.7. They are numbered in the order they will be discussed. The crossed boxes represent a cluster of opto-electronic devices.

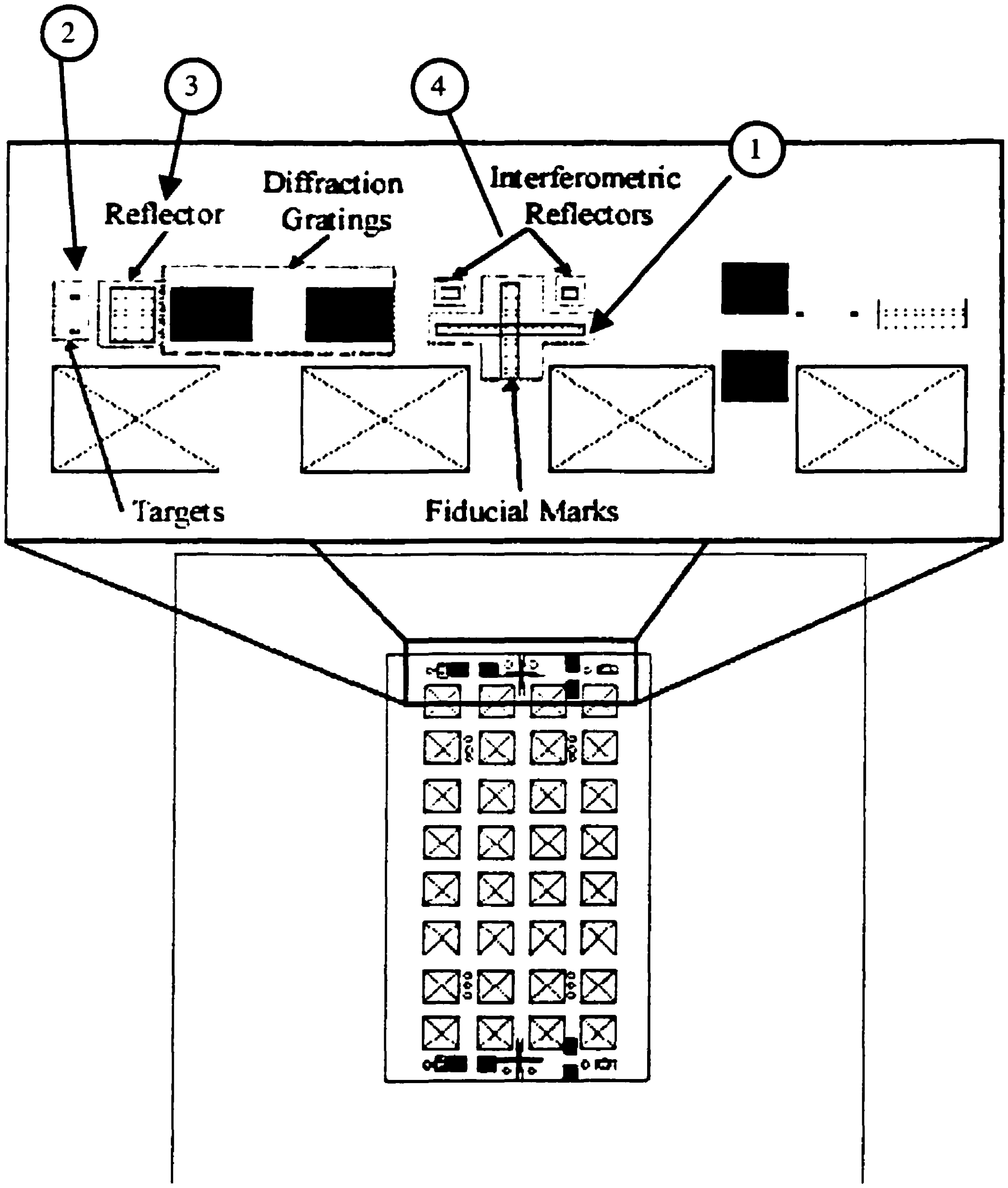

Figure 2.7: Overview of on-chip alignment features. [25]

The first alignment feature consisted of two cross-hairs, which was suitable for coarse alignment in X, Y, and rotation, θ. Using the top metal layer on the opto-electronic chip, a cross was laid out. The latter was placed between solid etched lines, of the correct pitch, on the lenslet array substrate as shown in Figure 2.8.

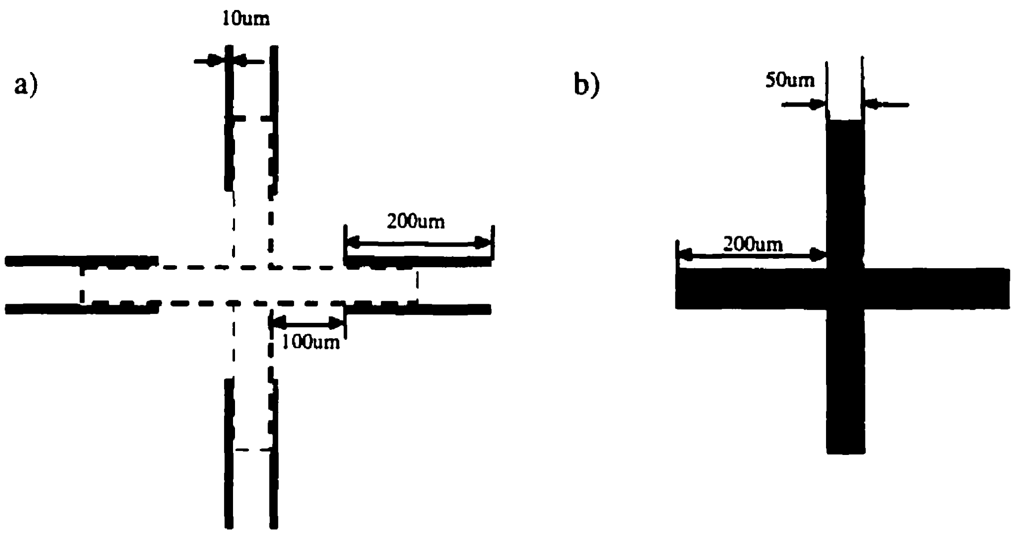

Figure 2.8: Fiducial marks as they appear on the a) Lens array and b) Optoelectronic chip. [24]

Due to the relative locations of the alignment features on the chip substrate and the lenslet array in the second and third schemes, it was necessary to use an off-axis lens to image the target properly. Since it is not possible to manufacture an off-axis refractive lens using thermal reflow, diffractive optics were used to direct an incoming beam of collimated light onto the target. Once the vertical position of best focus was reached, Z alignment had been achieved. By the same token, X and Y alignment was performed by aligning the focussed spot onto the target's center. Using one or more of these features simultaneously aligned the lenslet in tilt and θ.

In the first case, the target was situated on the chip surface and on the microlens substrate in the second instance. Aside from the feature location, the only difference between these two alignment strategies is the required focal length of the diffractive lens, as shown in Figure 2.9 and Figure 2.10.

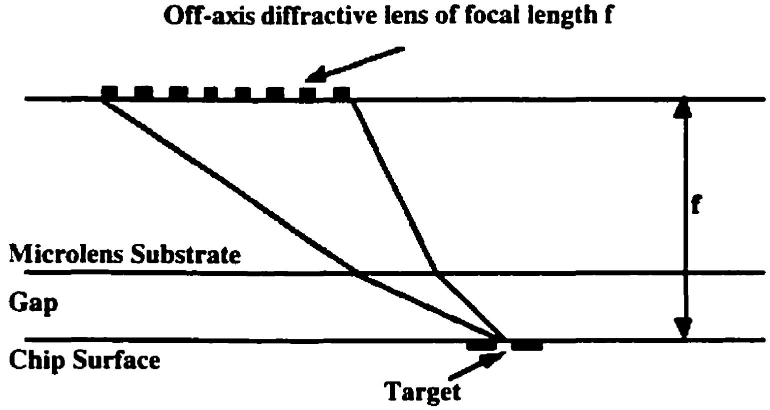

Figure 2.9: Single throw off-axis lens. [24]

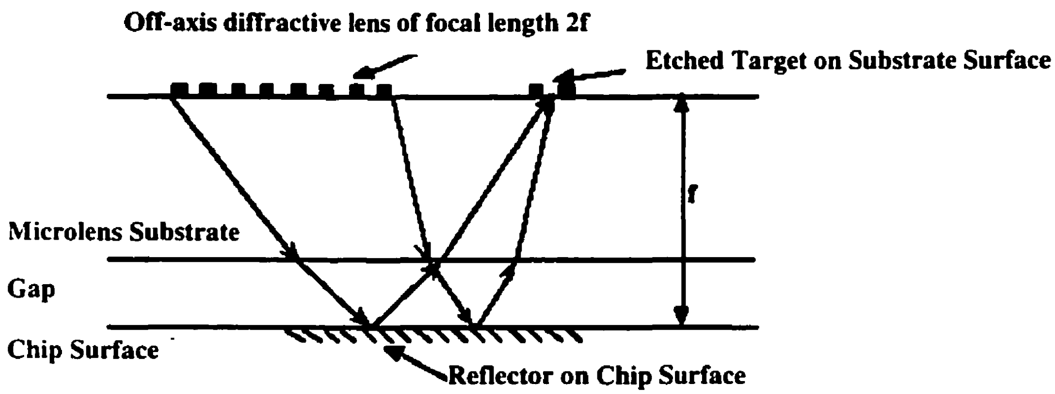

Figure 2.10: Double throw off-axis lens. [24]

The next alignment plan used interferometry to characterize the lenslet alignment status in the Z-direction. This setup required two pairs of reflectors situated in the vicinity of the fiducial markers examined at the beginning. Using the arrangement shown in Figure 2.11, an incident wavefront from a plane wave source and reflected one from an on-chip mirror interfered with one another. A quasi-Michelson interferometer combined wavefronts and output fringe patterns that corresponded to the degree of Z alignment. If the system was correctly aligned, widely spaced circular fringes were observed. Contrarily, many adjacent fringes, due to a non-planar reflected wavefront, were noted when the microlens array was not aligned [24].

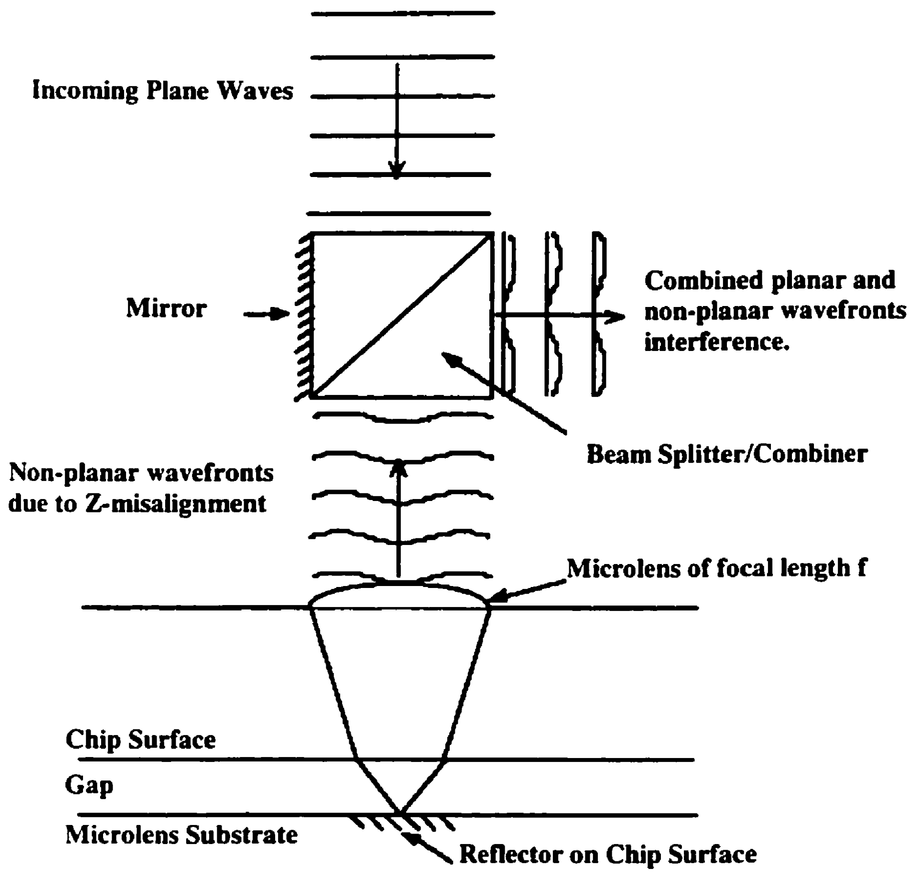

Figure 2.11: Arrangement for interferometric method. [24]

Optimal alignment was confirmed by combining the results of one or more of the alignment schemes simultaneously. The steps involved in aligning the lenslet will be described further on. Because the user was capable of placing the microlens array no closer than 10 μm from its ideal location, the MEMS were required to travel at least the same distance in any direction relative to that starting position.

2.4 References

1. R.P. Feynman, "There's Plenty of Room at the Bottom", Journal of Microelectromechanical Systems, Vol. 1, No. 1, pp. 60-66, March 1992.
2. A. Leonard, "As the MEMS Revolution Takes Off, Small is Getting Bigger Every Day", Wired, pp.162-164, January 2000.
3. O. Blum, M.E. Warren, H.Q. Hou, R.F. Carson, K.D. Choquette, M.S. Rodgers, and J.J. Sniegowsky, "Combined Photonics and MEMS function demonstration", SPIE, Vol. 3286, pp.57-61.
4. H.K. Trieu, L. Ewe, W. Mokwa, M. Schwarz, and B.J. Hosticka, "Flexible silicon structures for a retina implant", Micro Electro Mechanical Systems, 1998. MEMS 98. Proceedings, pp. 515-519, 1998.
5. K. Hoshino, F. Mura, and I. Shimoyama, "Design and Performance of a Micro-Sized Biomorphic Compound Eye with a Scanning Retina", Journal of Microelectromechanical Systems, pp. 32-37, March 2000.
6. An Introduction to Microelectromechanical Systems Engineering, Nadim Maluf, Microelectromechanical Systems Series, Artech House, Boston, p. 7, 2000.
7. S. Venkatesh and B. Culshaw, "Optically activated vibrations in a micromachined silica structure", Electron. Lett., No. 21, pp. 315-317 1985.
8. R.M.A. Fatah, N.A.D. Stokes, and S. Venkatesh, "Activation of silicon micromechanical resonators in fibre optic systems", Proceedings of EFCO 89, Amsterdam, pp. 418-422, 1989.
9. R.M.A. Fatah, N.A.D. Stokes, "All fibre-optic microresonator sensor system", New Materials and their Applications 1990 IOP Conference Series No. 111, Norfolk, 1990.
10. N.A.D. Stokes, R.M.A. Fatah, and S. Venkatesh, "Self-Excited Vibrations of Optical Microresonators", Electron. Lett., Vol. 24, No. 13, pp. 777-778, June 1998.
11. V.A. Aksyuk, C.R. Giles, A. Dentai, E.C. Burrus, C.A. Burrus, L. Stulz and D. Bishop, "Optically-Powered Optical Power Limiter for use in Lightwave Networks", IEEE, pp.344-348, 1999.
12. L.Y. Lin, E.L. Goldstein, and R.W. Tkach, "Free-Space Micromachined Optical Switches for Optical Networking", Journal of Selected Topics in Quantum Electronics, Vol.. 5, No. 1, pp. 4-9, 1999.

13. P. D. Lubell, "A coming attraction: D-cinema", IEEE Spectrum, pp. 72-78, March 2000.
14. J.M. Younse, "Mirrors on a Chip", IEEE Spectrum, pp.27-31, November 1993.
15. Elias Towe, "Digital-Micromirror-Display (DMD) Engine", Defense Advanced Research Projects Agency, http://www.darpa.mil/MTO/MOEMS/dmd/index.html.
16. SPC 1999 MEMS Markey Roadmap.
17. L.M. Castañer, and S.D. Senturia, "Speed-Energy Optimization of Electrostatic Actuators Based on Pull-In", Journal of Microelectromechanical Systems, Vol. 8, No. 3, pp.290-298, September, 1999.
18. M.A. Michalicek, D.E. Sene, and V.M. Bright, "Advanced Modeling of Micromirror Devices", Air Force Institute of Technology, Ohio.
19. L.Y. Lin, J.L. Shen, S.S. Lee, and M.C. Wu, "Surface-Micromachined Micro-XYZ Stages for Free-Space Microoptical Bench", IEEE Photonics Technology Letters, Vol. 9, No.3, pp. 345-347, March 1997.
20. McGill University Photonic Systems Group, "Demo 1: Microlens array specifications and alignment features", February 1999.
21. IBID, 20, p.4.
22. H.O. Sankur, M.E. Motamedi, R. Hall, W. Gunning, and M. Khoshnevisan, "Fabrication of refractive microlens arrays", Miniature and Micro-Optics and Micromechanics Proc. of SPIE, Vol. 2383, pp. 179-183, 1995.
23. The Practical Application of Light, Melles-Griot Incorporated, p. 4.13 of Material Properties, 1999. http://www.mellesgriot.com.
24. IBID, 20, pp.5-9.
25. IBID, 20, pp.10 and 11.

3 Fabrication Processes

3.1 Introduction

Microfabrication is the tool through which current MEMS and their associated applications have become possible. The material of choice is silicon for numerous reasons. Firstly, it is widely available due to its dominant presence in the microelectronics industry. Next, it exhibits excellent mechanical properties and has a stable oxide despite the oxide's high intrinsic stress. The oxide is electrically and thermally insulating while being relatively easy to produce [1]. This being said, MEMS devices can be manufactured following one of many different fabrication processes. Combining two or more of the processes discussed in this chapter can optimize the production of a device in particular. The number of releasable mechanical layers, whether or not both facets of the wafer can be used, and the number of required chemical treatments are only a few of the items that may distinguish one process from another [2, 3]. Consequently, emphasis will be placed upon the fundamental processes through which the majority of the MEMS devices on the market today are produced.

Firstly, bulk micromachining followed by other high aspect ratio machining techniques such as deep reactive ion etching (DRIE) and LIGA will be studied. Next, surface micromachining methods like the Multi-User MEMS Process (MUMPs) and Sandia Ultra-planar Multi-level MEMS Technology (SUMMiT) will be presented. Thirdly, techniques such as corner compensation, which protect MEMS structures from being over etched, will be mentioned. Lastly, issues pertaining to the wear and stiction of MEMS structures will be briefly introduced.

3.2 High Aspect Ratio Machining (HARM)

3.2.1 Bulk Micromachining

The simplicity and efficiency of this micromachining method explains its dominant presence in past and current commercial MEMS, such as pressure sensors, despite the increased etching resolution of silicon micromachining [4]. Bulk silicon etching is used to remove significant amounts of silicon from substrates using controlled interactions of an etchant with one of the substrate's crystalline plane directions. Only the areas that are unprotected by a silicon dioxide mask will be affected. Amongst the many available resists on the market [5] silicon dioxide is used due to the nature of the fabrication process. Firstly, a resist enables multiple structural layers to be lithographically patterned [6] whereas using silicon dioxide alone does not. However, since a substrate may be bulk micromachined only once, no more than one etch-resistant layer is required. So rather than use a photoresist that will both increase production cost and complicate the fabrication process, a single layer of readily available silicon dioxide is used. Lastly, most commercially available photoresists are polymers [7]. Since polymers do not have well defined lattices, but rather simple repeating units called monomers [8], the etching directionality required for bulk micromachined components is lost if a photoresist is used.

Recent advances in silicon bulk micromachining provide the designer with two virtual structural layers by taking advantage of the different etch rates of silicon nitride and silicon dioxide [11]. Although bulk micromachining is a popular choice, it utilizes aggressive chemicals that interact in one of two ways with the substrate; isotropically or anisotropically.

An isotropic reaction implies the uniform removal of silicon in the vicinity of the etchant regardless of the silicon structure's crystalline orientation at that location. Due to the undesired uniformity of the resulting isotropic etch, an anisotropic etchant is often used. In this case, the etch rate is selective as per the direction in which it is acting as illustrated in Figure 3.1 on the next page. In fact, the etch rate of potassium hydroxide (KOH) and tetramethylammonium hydroxide (TMAH), two common anisotropic etchants, is thirty and fifty times faster [2] in the <100> and <110>, respectively, than in the <111> directions [12]. Another key difference between etchants is the phase of the reactants be it a liquid, vapor, or plasma. A reactant in the liquid phase is referred to as a "wet" etchant whereas those in the vapor and plasma phases are considered to be "dry" etchants [4].

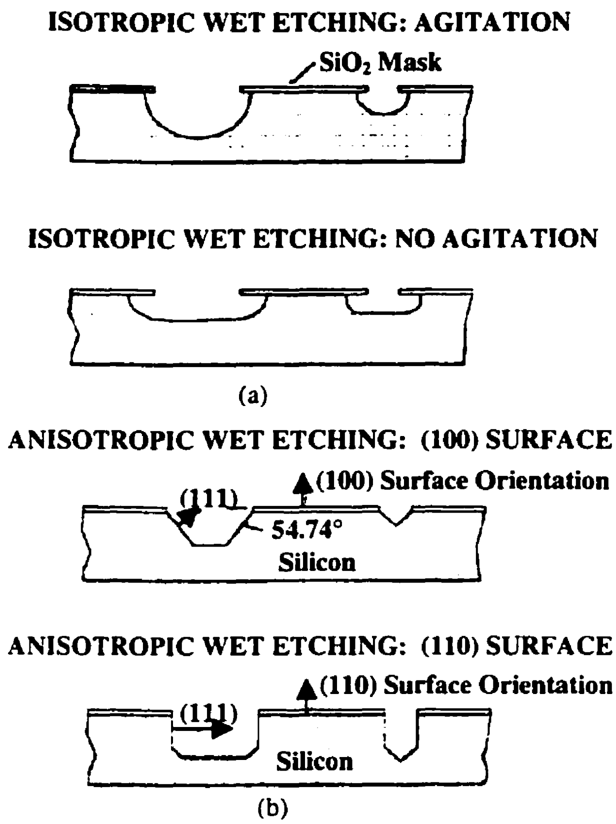

Figure 3.1: (a) Rounded anisotropically etched pits in a silicon substrate (b) Pyramidal pits etched into (100) and (110) silicon using anisotropic wet etchants, bounded by (111) crystal planes [4].

This micromachining approach can be used to create three-dimensional structures such as V-grooves to fulfill optical fiber packaging alignment needs for example [13]. Furthermore, the aggressive chemical etchants used in bulk micromachining do not alter on-chip Complementary Metal-Oxide-Semiconductor (CMOS) circuitry that may have been formed during a previous manufacturing stage. Consequently many more marketable MEMS can be created [4].

3.2.2 Deep Reactive Ion Etching (DRIE)

DRIE is an extension of bulk micromachining through which the formation of anisotropically etched randomly shaped and located features in single crystal silicon with high aspect ratios (depth/width) are accomplished [12]. The combination of dry etching of silicon using plasma systems and anisotropic processes, which are based on halogen/oxygen chemistry, are known as Reactive Ion etching (RIE) [2]. The latter grouping allows for the particles to impact the substrate at nearly normal incidence by controlling their motion through the use of an external electric or magnetic field [9]. As a result, well-defined edges and walls that are almost perpendicular to the substrate characterize the structures formed through RIE processes [10].

DRIE encountered three major obstacles on its way to becoming a potent micromachining tool. Firstly, low etch rates, on the order of 1 μm/min, meant it would take over five hours to etch to a depth of 300 μm. Furthermore, DRIE was initially unable to sustain structures with aspect ratios greater than five. Thirdly, masking layers had been ineffective in protecting surfaces from etchants [14]. These issues have been addressed by two commercially available dry etching systems.

The first is a system provided by Alcatel that is not very present in literature partially because it requires cryogenic cooling of the wafer holding apparatus. The second more popular process is offered by Surface Technology Systems (STS). It uses an inductively coupled plasma source to etch the silicon while using photoresist as a masking agent with a selectivity of 50:1. By using only 6 μm of photoresist, it is possible to etch to a depth of 300 μm yielding a height-to-width aspect ratio of approximately 100:1 [14]. The steps are shown in Figure 3.2 on the next page.

The processes' ability to form very high aspect structures has made DRIE a candidate in enhancing other low-etch micromachining methods. Recently, research has focussed upon combining the deep etching capabilities of DRIE with other micromachining processes such as surface micromachining [15].

Despite the relatively large resulting MEMS geometries, demanding tasks such as constructing an XY-stage covering a 160 μm x 160 μm area with a resolution of 1.0 μm has been demonstrated by C. S. B. Lee et al. [16].

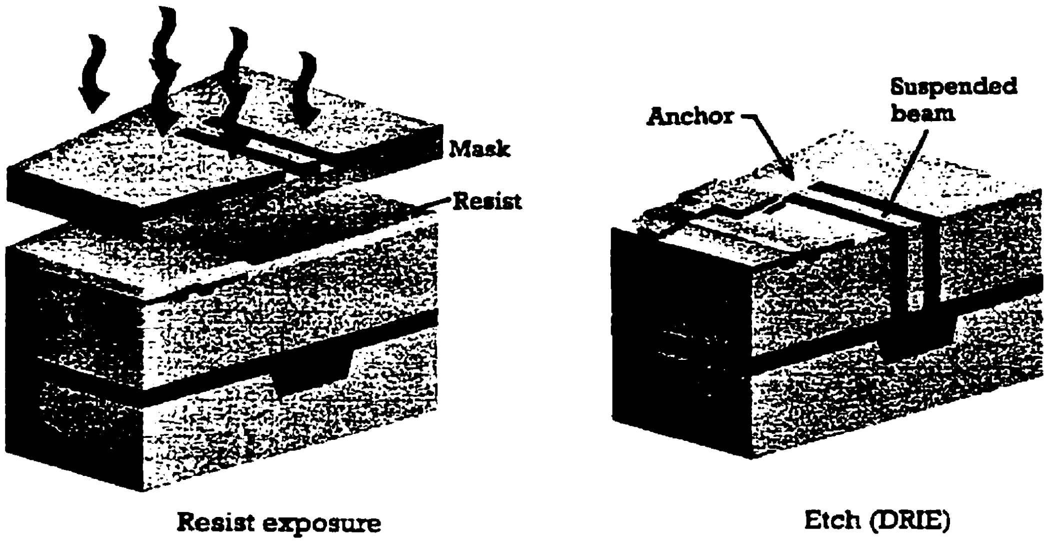

Figure 3.2: Fabrication process for deep reactive ion etching adpated from [17].

3.2.3 "LIthographie Galvanoformung Abformung" (LIGA)

LIGA is a German acronym that describes a micromachining technique that is based upon deep lithography, and replication processes such as microelectroforming and micromoulding. It permits the creation of extremely high aspect ratio devices from materials such as metals, polymers, glasses, and ceramic [18]. Structures may reach heights up to 1000 μm and height-to-width aspect ratios of 100:1 to 1000:1 [19]. Notwithstanding this fact, LIGA is still based upon the use of a single two-dimensional mask. Enhancements to the LIGA process have been proposed where a second structural layer is added [20] or the working surface area is increased [21].

Initially, a stable metal substrate plate, on top of which up to 1000 μm photoresist is deposited by conventional spin-coating techniques, is prepared. The most commonly used positive resist is Polymethylmethacrylate (PMMA). The ensuing drying process must be monitored to ensure that stresses within the PMMA are minimized. Otherwise, the resist might break off should this stress become too large. Next, deep-etch lithography is performed by exposing the resist to highly collimated X-rays as shown in Figure 3.3. After, the resist is exposed and developed, the resulting voids are filled via an electrodeposition process. Once the cavities have been filled, the remaining photoresist is etched away leaving behind an entirely metallic microstructure [19].

Microactuation benefits greatly not only from the deep etching resources of the LIGA process [22] but also from the large number of materials that are compatible with this fabrication technique. In addition, unlike bulk micromachining, the metallic and ceramic structures fabricated using LIGA may be used as molds that will facilitate manufacturing and reduce costs. As a result, MEMS made using LIGA have more applications than those which are bulk micromachined [23].

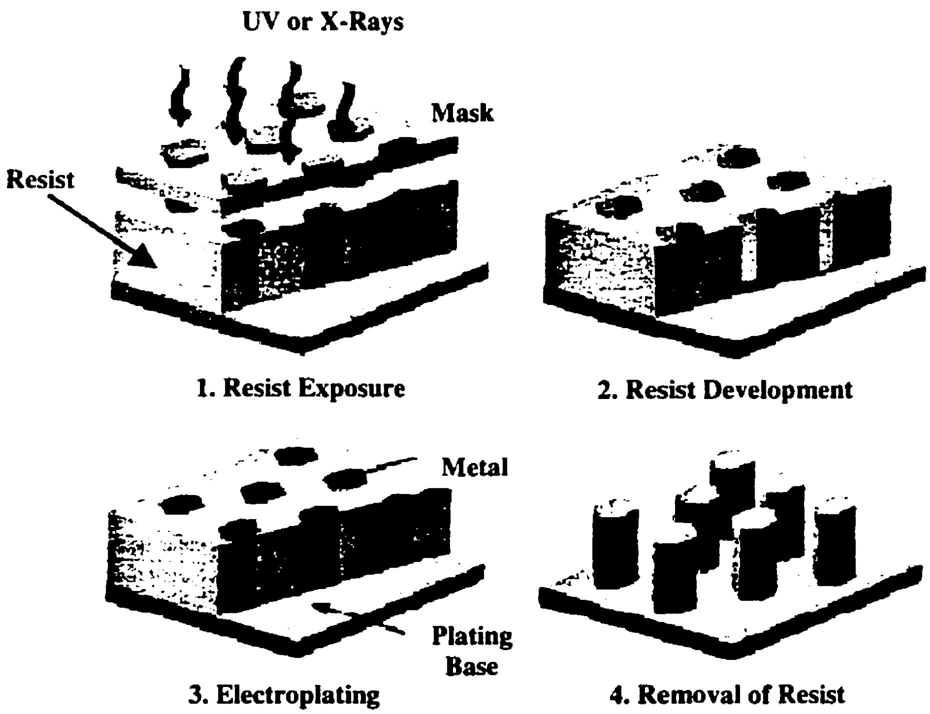

Figure 3.3: Illustration of mold formation using either optical or x-ray lithography and electroplating (LIGA) [24].

3.3 Surface Micromachining

Bulk micromachined components range typically from 100 μm to 500 μm in height whereas silicon micromachined components can attain a height of no more than 20 μm [14]. More importantly, unlike High Aspect Ratio Machining (HARM) techniques where structures are part of the substrate and etchants must be used to expose them, surface micromachining relies upon the sequential deposition of alternating structural and sacrificial layers [12]. Through the use of sacrificial masking layers, patterns are selectively etched into the unprotected areas of the polysilicon substrate. The process is illustrated in Figure 3.4.

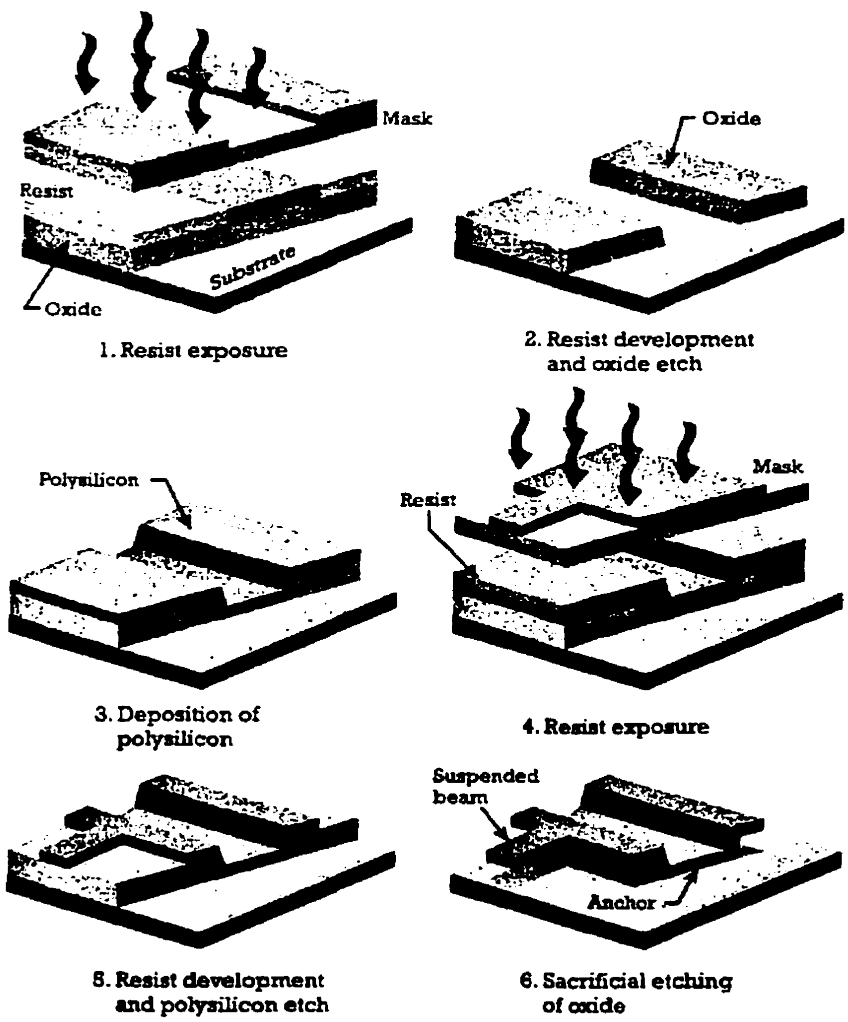

Figure 3.4: Schematic illustration of the basic process steps in surface micromachining [25].

3.3.1 Multi-User MEMS Process (MUMPs)

All the experimental data obtained for this work comes from devices that were manufactured using the MUMPs process. It is currently available to academic institutions through an agreement between the Canadian Microelectronics Corporation (CMC) and Cronos Integrated Microsystems. Three structural layers, shown in Figure 3.5, characterize this fabrication technique where only the top two are releasable. The bottom most layer, POLY0, may be used for wiring devices to power sources whereas POLY1 and POLY2 are dedicated to building mobile mechanical structures. In addition, a metal layer can be deposited onto POLY2 after the polysilicon structures are annealed at high temperatures to relieve stress [26].

One structural layer is sufficient when designing sensors and a supplementary layer enables the creation of simple actuators. Despite the use of process enhancing silicon dioxide and polysilicon microfabricated molds [27], two-layer processes become inadequate when MEMS such as geared motors are needed. The next discussed processes have temporarily satisfied the latter need.

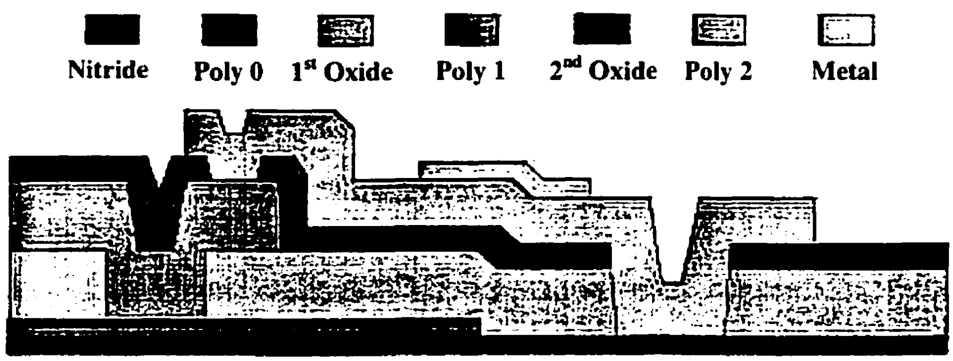

Figure 3.5: Cross sectional view showing all 7 layers of the MUMPs™ process [28].

3.3.2 Sandia Ultra-planar Multi-level MEMS Technology (SUMMiT)

The complexity of the micromachines that can be built with a given process is directly related to the number of available structural polysilicon layers the technology provides. Sandia National Laboratories (SNL) offers the world's only four layer process called SUMMiT [29] and another five structural layer one named SUMMiT V where up to three and four layers are releasable, respectively [31]. As demonstrated in Figure 3.6, the SUMMiT process requires a total of eleven individual masks [29] whereas the SUMMiT V technique requires a total of fourteen [31]. Improvements in residual film stress relief and surface planarity have permitted the addition of these structural layers.

Residual film stress results in structures that bow out of the plane. They are consequently difficult to calibrate and use. Next, the surface planarity, or topography, of a given structural layer will impact the correct deposition of a subsequent layer. As a result, proprietary techniques to mitigate both residual stress and surface planarization, via Chemical-Mechanical Polishing (CMP), have been developed at SNL [29]. The commercially available [30] SUMMiT processes have already been used successfully to design and characterize both micromirrors [33] and electrothermal actuator arrays [34].

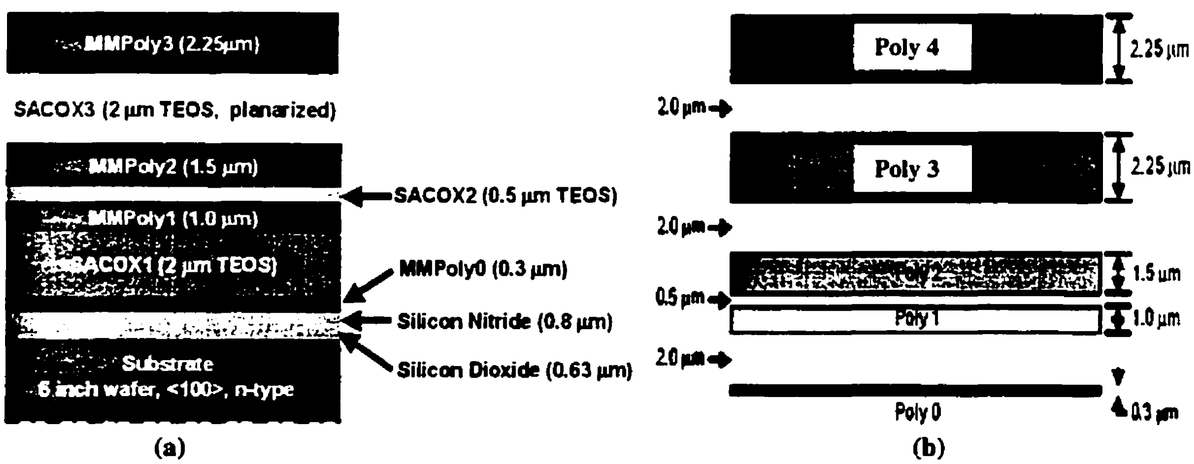

Figure 3.6: Cross sectional views showing all layers of the (a) SUMMiT [29] and (b) SUMMiT V [31] processes.

3.3.3 Integrated MicroElectroMechanical Systems (IMEMS)

Thus far, no single process has successfully batch fabricated both CMOS circuitry and MEMS devices onto the same wafer. An innovative procedure, originating from SNL, called IMEMS enables the formation of both mechanical and electronic sections on the same polysilicon substrate. IMEMS not only reduces the cost of production but also augments system reliability by lowering the number of packaging steps. The damaging effects of the high temperature annealing process upon the polysilicon CMOS interconnects further motivated research within the microfabrication community.

The fabrication process begins with the creation of a 12 μm deep trench within which the MEMS devices are built using previously discussed techniques such as SUMMiT. The devices are annealed and the trench is then filled with silicon dioxide, to protect them from the next fabrication step and then planarized with CMP as shown in Figure 3.7. After the CMOS circuits are fabricated, both subsystems are electrically connected. Now that a link has been established, the protective silicon dioxide is etched away to reveal an operational CMOS-MEMS chip [34].

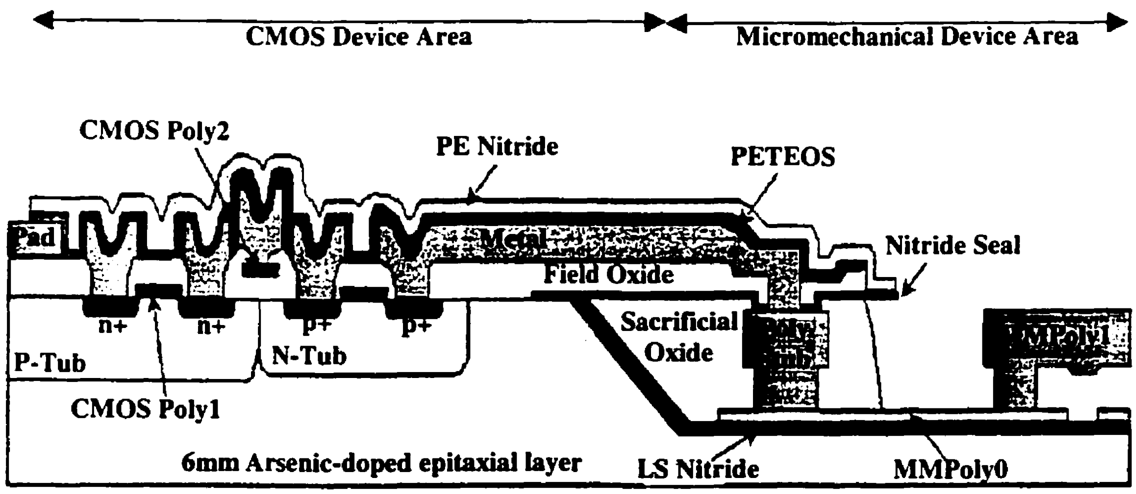

Figure 3.7: Cross sectional view of the IMEMS process showing both CMOS and MEMS layers [34].

3.4 Corner Compensation

Aligning a ball lens to maximize the light coupled into a target fiber often entails the use of precisely etched structures such as right-angled corners. Anisotropic wet etches are aggressive and therefore make the definition of such shapes difficult. By using corner compensation, powerful etchants may dissolve non-functional structures, such as those in Figure 3.8(i), while releasing and preserving useful MEMS structures [35].

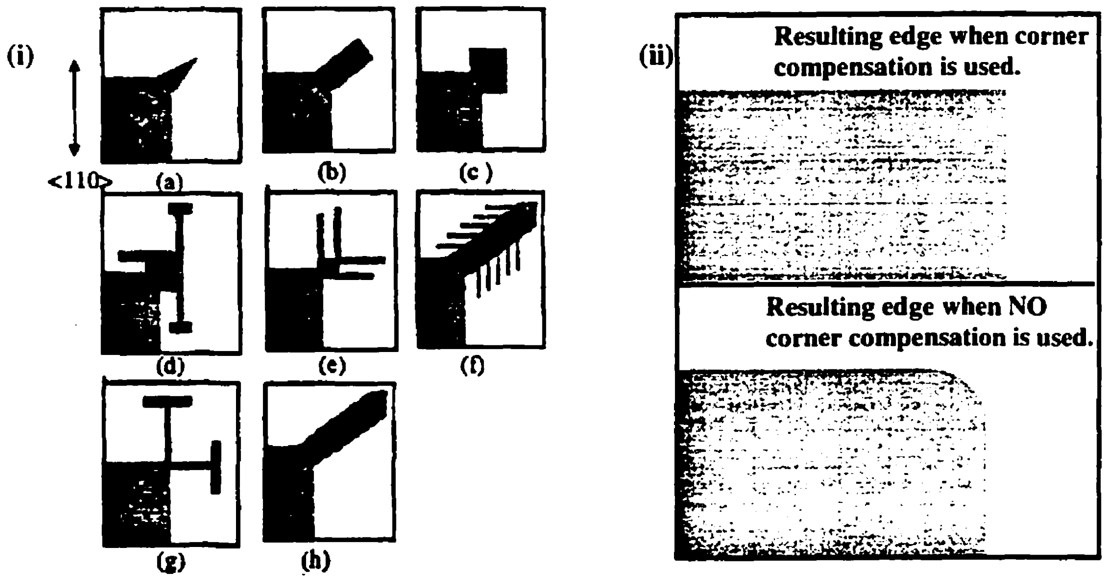

Figure 3.8: (i) Various corner compensation designs [35] and (ii) a schematic of both a protected and unprotected corner.

For a corner compensating structure to be effective (Figure 3.8(ii)) in preserving geometries, it must be properly designed and selected in accordance with the etchant used [37]. To this end, much research has been focussed upon acquiring knowledge about the chemical interaction between a variety of reactants and potential structural materials [36]. Potassium hydroxide (KOH) [37] and tetramethylammonium hydroxide (TMAH) [38] are two of the most commonly used agents. Although it is effective, corner compensation is not always practical because it occupies space that may be needed for structural components.

3.5 Microscopic Wear in MEMS

The proper operation of airbag deployment systems and certain navigational equipment currently rely upon MEMS. Before such innovative structures became common place, they were extensively tested to determine their durability. Wear at the microscopic level, at which MEMS operate, must be understood if mechanically reliable devices are to be created and marketed. The wear of a MEMS device can be assessed in one of two ways. Firstly after the prototype MEMS device has been constructed or with the use of macroscopic test structures, on the order of millimeters.

The latter analysis approach is most commonly adopted since it bypasses all prototyping costs of in situ measurements. The fabrication of these macroscopic test structures must be done using the same processes and materials that will be utilized to build the micromachined elements. This is necessary to ensure that the obtained results are representative of the MEMS device's true tribological behavior. The need for knowledge regarding the materials being used has motivated studies examining the mechanical properties of polysilicon [39] and the characteristics of silicon carbide (SiC) coatings [40]. The effects of ion implantation upon the wear of silicon in addition to dry versus lubricated sliding conditions as well as rotationally induced gear wear have been investigated.

Two wear mechanisms were identified, asperity fracture and asperity deformation. Despite these microscopic apparatuses, the hardest materials still exhibited the lowest amount of stress regardless of the method it was applied, much like in the macroscopic domain [41].

3.6 Stiction and MEMS

MEMS devices may fail due to friction-induced failures [42]. Stiction, adhesion, and static friction are all terms that refer to a common phenomenon whereby a mobile structure is prevented from moving from a given position. Stiction that is observed after the chemical wet etch structural release phase is called "release stiction". In addition, "in-use stiction" relates to adhesion observed while a device is operating [43].

The causes of release stiction are inter-linked but may be traced to a fundamental source, which is the substrate drying phase that follows the wet etch and rinse. At the microscopic level, the dominant forces [44] are related to rubbing and contact as opposed to gravitational forces, which are insignificant. When the wafer is pulled out of the etchant or rinsing bath, menisci are formed at the residual liquid-air interfaces between released components and the substrate. These remnants of the sacrificial layer removal phase pull moveable structures down into contact with the substrate via capillary forces [45]. The latter are governed by the summed contributions of surface tension and a Laplace pressure component. [46]

When menisci no longer inhibit motion, in-use stiction becomes an issue. It is brought upon by surface roughness and ambient humidity. Given the typically anisotropic topology of a moveable surface and that of the underlying substrate, friction becomes a directional quantity [47]. Excessive surface coarseness at the interface of a moveable structure and a stationary one will bring upon in-use stiction.

It can be remedied through the use of lubricants [47], avoiding contamination [48], and by polishing the various contact surfaces. High relative humidity [49] levels must be controlled and avoided by monitoring the operating conditions closely and isolating the vulnerable structures, respectively. Eliminating menisci, and hence release stiction, may be accomplished by modeling [46] and improving drying processes [50]. Using stiction-reducing monolayer films [51] and modifying device geometries [45] to prevent the formation of menisci are also common practice. By carefully understanding and subsequently optimizing the fabrication process, appropriate stiction-related detection and locating features may be integrated into MEMS [52]. These elements will ensure the validity of the final testing phase and in so doing, guarantee that the production line's output is functionally successful.

3.7 References

1. An Introduction to Microelectromechanical Systems Engineering, Nadim Maluf, Microelectromechanical Systems Series, Artech House, Boston, p. 23, 2000.
2. D. Wood, "The Fabrication of Silicon Microsystems", IEE Electronics & Communication Engineering Journal, pp.253-260, December 1999.
3. D. F. Moore and R. R. A. Syms, "Recent Developments in Micromachined Silicon", IEE Electronics & Communication Engineering Journal, pp.261-270, December 1999.
4. G. T. A. Kovacs, N. I. Maluf, and K. E. Petersen, "Bulk Micromachining of Silicon", Proceedings of the IEEE, Vol. 86, No.8, pp. 1536-1551, August 1998.
5. C. G. Wilson, in Introduction to Microlithography, edited by L. F. Thompson, C. G. Wilson, and M. J. Bowden, American Chemical Society Publishing, p. 139, 1994.
6. M. S. Hibbs, in Introduction to Microlithography, edited by L. F. Thompson, C. G. Wilson, and M. J. Bowden, American Chemical Society Publishing, p. 1, 1994.
7. B. W. Smith, in Introduction to Microlithography, edited by L. F. Thompson, C. G. Wilson, and M. J. Bowden, American Chemical Society Publishing, p. 519, 1994.
8. R. Chang, Chemistry, fourth edition, McGraw-Hill Inc., p. 1026, 1991.
9. R. R. Kunz, in Microlithography Science and Technology, edited by J. R. Sheats and B. W. Smith, Marcel Decker Inc., New York, p.616, 1998.
10. IBID, 1, p.68.
11. Resnik, D., Aljancic, U., Vrtacnik, D., and Amon, S, "A New Approach to Silicon Bulk Micromachining", Mediterranean Electrotechnical Conference, 1998. MELECON 98., 9th , Volume: 1 , 1998 Page(s): 330 -334 vol.1
12. M. C. Wu, "Micromachining for Optical and Optoelectronic Systems", Proceedings of the IEEE, Vol. 85, No.11, pp. 1833-1856, November 1997.
13. H. Han, J. E. Schramm, J. Mathews, and R. A. Boudreau, "Micromachined Silicon Structures for Single Mode Passive Alignment", Proceedings of SPIE Optoelectronic Packaging, Vol. 2691, pp. 118-123, February 1996.

14. E. H. Klaassen, K. Petersen, J. M. Noworoloski, J. Logan, N. I. Maluf, J. Brown, C. Storemont, W. McCulley, and G. T. A. Kovacs, "Silicon Fusion Bonding and Deep Reactive Ion Etching; A New Technology for Microstructures", 8th International Conference on Solid-State Sensors and Actuators, pp.556-559, June 1995.
15. J.-L. A Yeh, H. Jiang, and N. C. Tien, "Integrated Polysilicon and DRIE Bulk Silicon Micromachining for an Electrostatic Torsional Actuator", Journal of Microelectromechanical Systems, Vol. 8, No.4, pp. 456-465, December 1999.
16. C. S. B. Lee, S. Han, and N. C. MacDonald, "Single Crystal Silicon (SCS) XY-Stage Fabricated by DRIE and IR Alignment", Micro Electro Mechanical Systems, 2000. MEMS 2000, pp. 28 –33.
17. IBID, 1, p.80.
18. W. Ehrfeld, M. Abraham, U. Ehrfeld, M. Lacher, and H. Lehr, "Materials for LIGA Products", Micro Electro Mechanical Systems, 1994, MEMS '94, pp. 86 –90.
19. M. McCormick, E. Chowanietz, and A. Lees, "Microengineering Design and Manufacture Using the LIGA Process", Engineering Science and Education Journal, pp. 255-262, December 1994.
20. S. Massoud-Ansari, P. S. Mangat, J. Klein, and H. Guckel, "A Multi-Level, LIGA-Like Process for Three Dimensional Actuators", Micro Electro Mechanical Systems 1996 Proceedings, IEEE, pp. 285 -289, 1996.
21. C. Marques, Y. M. Desta, J. Rogers, M. C. Murphy, and K. Kelly, "Fabrication of High-Aspect-Ratio Microstructures on Planar and Nonplanar Surfaces sing a Modified LIGA Process", Journal of Microelectromechanical Systems, Vol. 6, No.4, pp. 329-336, December 1997.
22. R. Kondo, K. Suzuki, S. Sugiyama, "Study on Fabrication of High Aspect Ratio Electrostatic Micro Actuators Using the LIGA Process", International Symposium on Mechatronics and Human Science, pp. 155-160, 1998.
23. H. Debeda, T. V. Freyhold, J. Mohr, U. Wallrabe,and J. Wengelink, "Development of Miniaturized Piezoelectric Actuators for Optical Applications Realized Using LIGA Technology", Journal of Microelectromechanical Systems, Vol. 8, No.3, pp. 258-263, September 1997.

24. IBID, 1, p.76.

25. IBID, 1, p.78.

26. J. H. Comtois, M. A. Michalicek, and C. G. Barron, "Fabricating Micro-Instruments in Surface-Micromachined Polycrystalline Silicon", Proceedings of the 43rd International Instrumentation Symposium, pp.169-179, 1997.

27. A. A. Yasseen, C. A. Zorman, and M. Mehregany, "Surface Micromachining of Polycrystalline SiC Films Using Microfabricated Molds of SiO_2 and Polysilicon", Jrnl. of Microelectromechanical Systems, Vol. 8, No.3, pp. 237-242, September 1999.

28. D. A. Koester, R. Mahadevan, A. Shishkoff, and K. W. Markus, "MUMPS™ Design Handbook", Cronos Integrated Microsystems, p.1, May 1999.

29. J. McBrayer, "SUMMiT Technology", Sandia National Laboratories Intelligent Micromachine Initiative, http://www.mdl.sandia.gov/micromachine/trilevel.html.

30. Based upon a conversation with Mr. John McBrayer.

31. J. Sniegowski, "SUMMiT V Technology", Sandia National Laboratories Intelligent Micromachine Initiative, http://www.mdl.sandia.gov/micromachine/summit5.html.

32. M. A. Michalicek, J. H. Comtois, and C. C. Barron, "Design and Characterization of Next-Generation Micromirrors Fabricated in a Four-Level, Planarized Surface-Micromachined Polycrystalline Process", Proceedings of Innovative Systems in Silicon, pp. 144 –154, 1997.

33. J. H. Comtois, M. A. Michalicek, and C. C. Barron, "Characterization of Electrothermal Actuators and Arrays Fabricated in a Four-Level Planarized Surface-Micromachined Polycrystalline Process", Conference on Solid-State Sensors and Actuators, pp. 769-772, June 1997.

34. S. Montague and J. Jakubczak, "Integrated MicroElectroMechnical Systems", Sandia National Laboratories Intelligent Micromachine Initiative, http://www.mdl.sandia.gov/micromachine/integrated.html.

35. L.-S. Huang, S.-S. Lee, E. Motamedi, M. C. Wu, and C.-J. Kim, "MEMS Packaging for Micro Mirror Switches", IEEE Electronic Components and Technology Conference, pp. 592-597, 1998.

36. K. R. Williams and R. S. Muller, "Etch Rates for Micromachining Processing", Jrnl. of Microelectromechanical Systems, Vol. 5, No.4, pp. 329-336, December 1996.

37. H. Sandmaier, H. L. Offereins, K. Kühl, and W. Lang, "Corner Compensation Techniques in Anisotropic Etching of (100)-Silicon Using Aqueous KOH", IEEE Solid-State Sensors and Actuators, pp. 456-459, 1991.

38. B. Nikpour, L. M. Landsberger, T. J. Hubbard, M. Kahrizi, and A. Iftimie, "Patterns for Concave Corner Compensation Between Vertical (010)-(001) Planes on Si(100) Anistropically Etched in TMAH", Conference on Solid-State Sensors and Actuators, pp. 691-694, June 1997.

39. W. N. Sharpe, B. Yuan, R. Vaidyanathan, and R. L. Edwards, "Measurements of Young's Modulus, Poisson's Ratio, and Tensile Strength of Polysilicon", IEEE Proceedings of MEMS ' 97, pp: 424 –429.

40. M. Mehregany, L. Tong, L. G. Matus, and D. J. Larkin, "Internal Stress and Eleastic Modulus Measurements on Micromachined 3C-SiC Thin Films", IEEE Transactions on Electronic Devices, Vol. 44, No. 1, pp. 74-79, January 1997.

41. B. Beerschwinger, T. Albrecht, D. Mathieson, R. L. Reuben, S. J. Yang, and M. Taghizadeh, "Wear at Microscopic Scales and Light Loads for MEMS Applications", Elsevier Science S. A., pp. 426-435, 1995.

42. R. Maboudian and R. T. Howe, "Critical Review: Adhesion in Surface Micromechanical Structures", Journal of Vacuum Science Technology, Section B, Vol. 15, No. 1, pp. 1-20, 1997.

43. B.-H. Kim, C.-H. Oh, K. Chun, T.-K. Chung, J.-W. Byun, and Y.-S. Lee, "A New Class of Surface Modifiers for Stiction Reduction", Proceedings of the International Conference on Micro Electro Mechanical Systems, pp. 189-193, 1999.

44. F. M. Serry, D. Walliser, and G. J. Maclay, "The Anharmonic Casimir Oscillator (ACO) – The Casimir Effect in a Model Microelectromechanical System", Journal of Microelectromechanical Systems, Vol. 4, No.4, pp. 193-205, December 1995.

45. S. L. Miller, M. S. Rodgers, G. LaVigne, J. J. Sniegowski, P. Clews, D. M. Tanner, and K. A. Peterson, "Failure Modes in Surface Micromachined MicroElctroMechanical Actuators", Proceedings of the 36th Annual International Reliability Physics Symposium, pp. 17-25, 1998.

46. T. Abe, W. C. Messner, and M. L. Reed, "Effective Methods to Prevent Stiction During Post-Release-Etch Processing", Proceedings of the International Conference on Micro Electro Mechanical Systems, pp. 94-99, 1995.
47. B. Bhushan, "Nanotribology and Nanomechanics of MEMS Devices", Proceedings of the International Conference on Micro Electro Mechanical Systems, pp. 91-98, 1996.
48. A. J. Kolpekwar, T. Jiang, R. D. Blanton, "CARAMEL: Contamination And Reliability Analysis of MicocroElectromechanical Layout" Journal of Microelectromechanical Systems, Vol. 8, No.3, pp. 309-318, September 1999.
49. M. Ohtsu, K. Minami, M. Esashi, "Fabrication of Packaged Thin Beam Structures by an Improved Drying Method", Proceedings of the International Conference on Micro Electro Mechanical Systems, pp. 228-233, 1996.
50. S. T. Patton, W. D. Cowan, and J. S. Zabinski, "Performance and Reliability of a New MEMS Electrostatic Lateral Output Motor", Proceedings of the 37th Annual International Reliability Physics Symposium, pp. 179-188, 1999.
51. U. Srinivasan, M. R. Houston, R. T. Howe, and R. Maboudian, "Alkyltrichlorosilane-Based Self-Assembled Monolayer Films for Stiction Reduction in Silicon Micromachines", Journal of Microelectromechanical Systems, Vol. 7, No.2, pp. 252-260, December 1995.
52. A. Kolpekwar, R. D. Blanton, and D. Woodilla, "Failure Modes for Stiction in Surface-Micromachined MEMS", Proceedings of the 1998 International Test Conference, pp. 551-556.

4 Actuation Methods

4.1 Introduction

The design of MEMS actuators represents a unique challenge in that it depends highly upon the intended application, the available wafer space, and the power budget. However, the available fabrication process is the dominant limiting factor. Motivated by these and other factors, current MEMS actuators have been designed to overcome different subsets of the latter obstacles. Despite the numerous solutions, these schemes can be reduced to a few fundamental actuator designs, which will be introduced and analyzed in this chapter.

An actuator's dynamic performance is characterized by the repeatability, linearity, precision, accuracy, and speed of its motion in addition to its load-bearing capability, stiffness, and cost [1]. Repeatability and precision are two specifications that are especially significant, within this context. Repeatability is a measure of the deviation of an actuator's motion relative to a reference displacement versus current or voltage curve. The choice of reference depends upon the nature of the actuation method. A low repeatability is commonly due to hysteresis where either a complete lack of motion, deadband, (Figure 4.1a) or a continuous curve (Figure 4.1b) is observed [2]. Next, precision is defined as the ratio of displacement range (in microns) to resolution with which an actuator can move (in microns) [3].

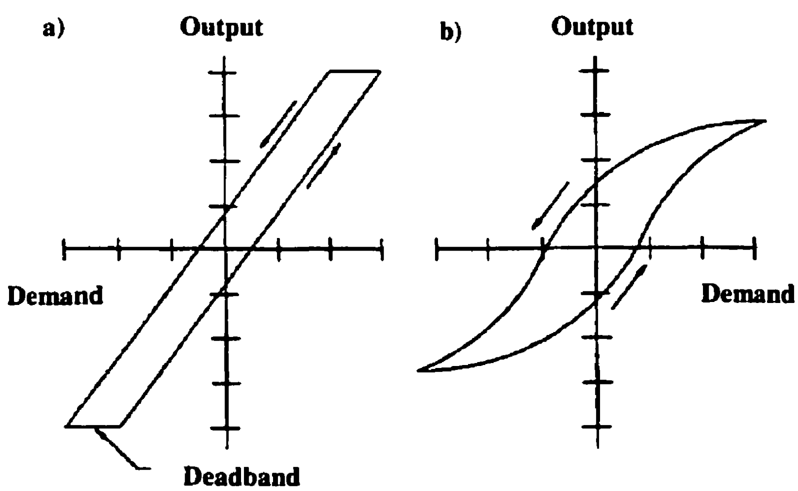

Figure 4.1: Hysteresis in displacement actuators. a) deadband and b) continuous [2].

Actuators may be placed in one of two categories. The first group is called in-plane actuators, since they induce motion in the plane parallel to the wafer, and an out-of-plane motion along the vertical Z-axis characterizes the second. In both cases, electrostatically and thermally operating devices will be considered.

4.2 Scaling of Forces

Prior to investigating the actuators of interest, a brief mention with regards to the scaling of forces must be made. The physical behavior and impact of forces at the microscopic level may be enhanced or inhibited by fundamental scaling properties. As a result, their performance at the microscopic level depends greatly on the factor by which the system is scaled down. For example, electrostatic forces are more potent in the realm of micromachined devices than are magnetic forces [4]. Understanding the effects of scaling is key to building accurate and useful device models.

4.3 Lateral Actuation Techniques

4.3.1 Electrostatic Actuation

In general, electrostatic actuation is a non-contact actuation scheme. Two electrostatically operated actuators will be examined to motivate the latter. Firstly, the Comb Drive Actuator (CDA) followed by the Scratch Drive Actuator (SDA).

4.3.1.1 Comb Drive Actuator (CDA)

Comb drive actuators are MEMS that take advantage of the fact that electrostatic forces scale down well. Comb drive actuators have been used in resonant microstructures for sensing purposes [5], micromirror scanning and positioning [6], microvibromotors [7], and the actuation of XY-stages [8].

A generic model of a CDA resonator is shown in Figure 4.2 on the next page. It is composed of primarily three structures, a stator, a rotor, and an underlying ground plane connected to "Pad 2". Lateral motion is induced electrostatically by overlapping a movable set of comb fingers (rotor) and a stationary set of fingers (stator). If "Pad 1" and "Pad 2" provide the CDA with voltages that are 90° out of phase with respect to one another, the rotor will oscillate along the y-axis [5]. The rotor's motion along the positive y-axis, illustrated in Figure 4.2, represents the instance when a non-zero, and therefore attractive (Eq. 4.2), potential is provided to the oscillator through "Pad 1".

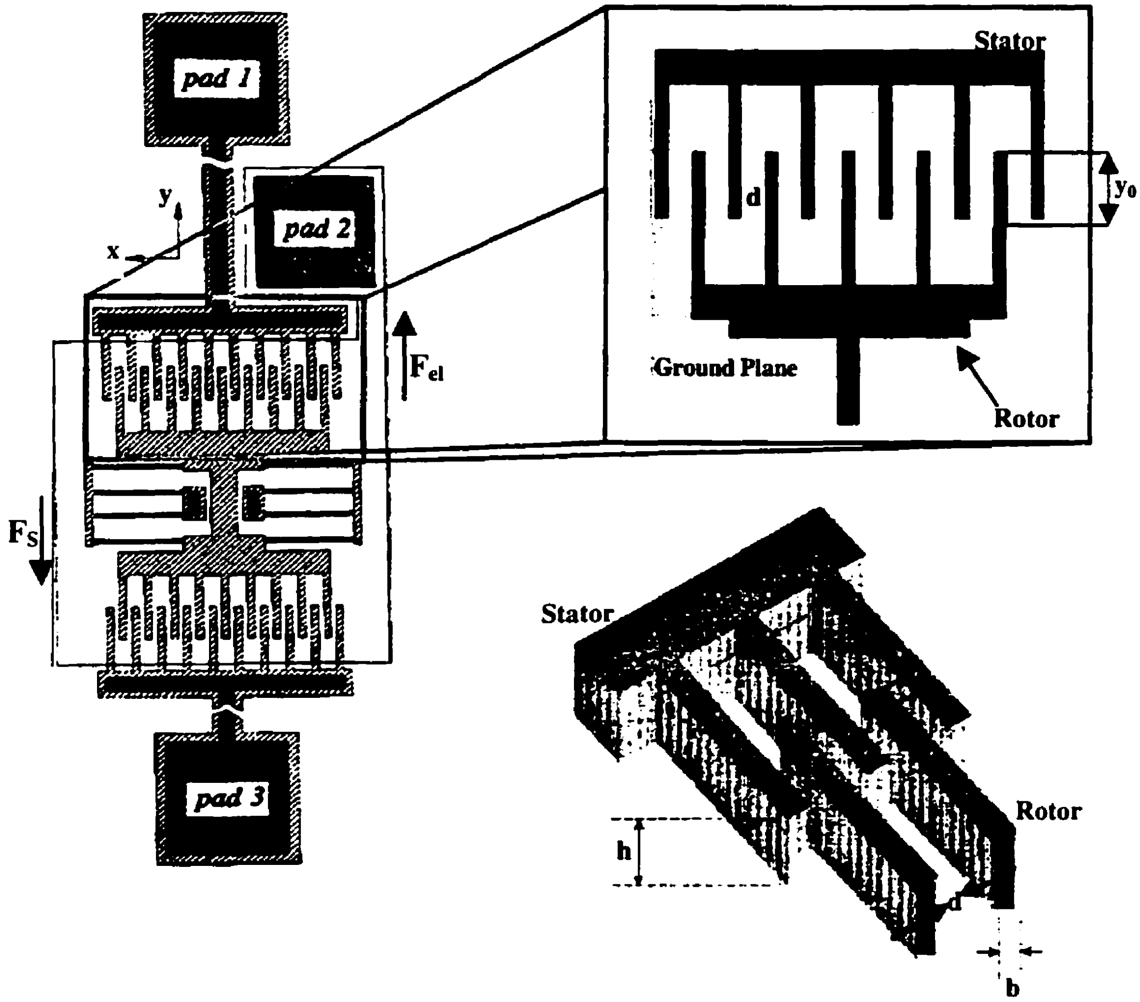

Figure 4.2: Comb Drive Actuator (CDA) schematic [11] and a modified 3-D close-up [12].

Ultimately, it is the capacitance generated between the rotor and the stator that will determine the magnitude of the observed force and displacement [9]. The plane beneath the overall structure is usually set to the same potential as the rotor in order to avoid electrostatic pull-down forces to the substrate [9]. Next, to prevent the movable comb structure from being permanently propelled away from the stator, spring-like structures are included to supply the necessary restoring force. These springs [9] are beams that flex in response to and oppose the generated electrostatic force as pointed out in Figure 4.2.

For a spring, the restoring force F_S may be expressed as the product of the spring constant k and the displacement Δx. The electrostatically induced lateral force F_{el} [10] in the y-direction depends upon the capacitance generated by the overlapping plates, the inter finger gap d, and the applied voltage V. The capacitance C between the stator and the rotor may be expressed as:

$$C = \frac{2n\varepsilon_0 b(y + y_0)}{d} \qquad \text{Equation 4.1}$$

F_{el} is equal to:

$$F_{el} = \frac{1}{2} \cdot \frac{\partial C}{\partial y} \cdot V^2 = \frac{n\varepsilon_0 b}{d} \cdot V^2 \qquad \text{Equation 4.2}$$

then the displacement will equal:

$$y = \frac{n\varepsilon_0 b}{kd} \cdot V^2 \qquad \text{Equation 4.3}$$

where n is the number of fingers, ε_0 is the dielectric constant in air, b is the width of the comb fingers, y_0 is the initial comb finger overlap, y is the comb displacement [9], and h is the finger thickness.

The theory that has been presented pertains to a comb drive that has symmetric stator and rotor finger geometries. Asymmetric comb drives [12] are useful for both lateral and vertical actuation. To further enhance the symmetric CDA's efficiency, the comb fingers may be optimally shaped [13] and angled [14]. Next, compensating for the device's structural stress [15], tuning the stiffness coefficients [16], and minimizing out-of-plane comb finger deflection [11] will maximize the inter comb finger overlap area, which will increase the generated capacitance C and hence the output force. The generated force may be further augmented by reducing inter comb finger spacing, d [17].

Lastly, inter comb finger isolation will reduce the comb drive's power consumption by reducing current leakage to the underlying ground plane [18].

4.3.1.2 Scratch Drive Actuator (SDA)

Scratch drive actuators must be in contact with the substrate in order to achieve lateral motion by "scratching" in the desired direction. Because of the latter and the fact that it is an electrostatically based device, the area below the SDA must be electrically insulated from the substrate in order to enable electrostatic actuation. The operation of a scratch drive actuator is demonstrated in Figure 4.3 below.

During the rising voltage edge, the plate is pulled downwards with the exception of the device's front end, due to bushing (Figure 4.3c). As a result, elastic strain energy is temporarily stored. While the pulse falls, the plate begins to detach from the surface and in so doing, displaces the tail forward (Figure 4.3d). On the subsequent rising edge, the plate, which is already partially in contact with the substrate, is quickly pulled down once again. Therefore, the bushing is pushed forward due to the deformation of the plate. [19]

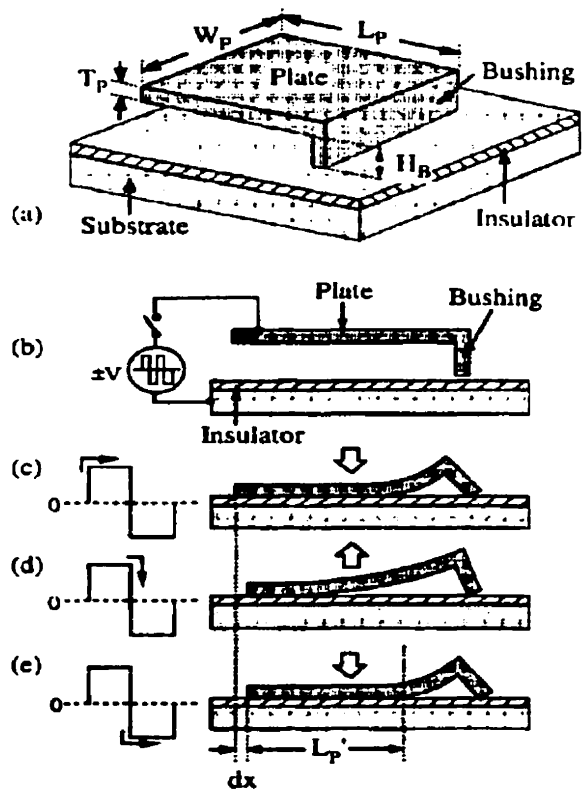

Figure 4.3: (a) SDA structure with dimension definition and (b)-(e) the evolution of the plate deformation during actuation. [19]

Scratch drive actuators are capable of producing an output force of up to 100 μN and moving over a distance of 500 μm in increments of 0.1 μm. Moreover, adjusting the applied pulse's amplitude and frequency can control the device's motion and velocity, respectively [19]. Scratch drive actuators have been used to position a mirror in the X-Y plane [20] and for assembling complex 3-D structures [22]. In fact, driving forces of up to 100 000 μN have been reported using 6.0 mm^2 polysilicon sheets that integrate up to 1430 scratch drive actuators [23].

4.3.2 Thermal Actuation

Electrostatic devices require either an operating voltage as high as 100 V, narrow capacitative gaps, as discussed previously with the CDA, or a large device surface area. The heat-drive actuator, which is also called a heatuator and is shown in Figure 4.4, is a MEMS that can achieve lateral actuation while avoiding the latter limitations. It can operate within an area as small as 200 x 18 μm^2 with an input power of less than 25 mW and yield a deflection greater than 10 μm [24]. As a result, the lateral thermal actuator has been used successfully in many arrayed configurations [31, 32].

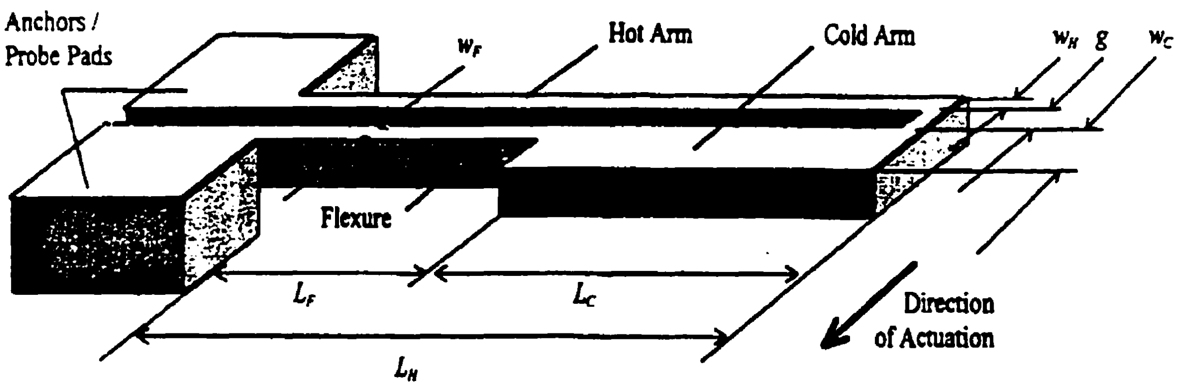

Figure 4.4: Geometry of a heat-drive actuator or heatuator. [24]

A heat-driven actuator is composed primarily of a wide "cold arm", a narrower "hot arm", and a flexure. The variables w and L refer to the width and length, respectively, of either the hot arm, cold arm, or flexure. The latter may be differentiated through the use of a subscripted "c", "h", or "f" that relate to the cold arm, hot arm, and the flexure properties, respectively.

A heatuator may be constructed using only one releasable layer. The flexure acts as a joint that facilitates the observed lateral bending motion. Both arms are connected to one another at the moveable extremity while each arm is also connected to an independent anchor. The theory of operation relies upon the fact that the hot arm will heat up faster than the cold arm, upon passing a DC current through the structure, since the hot arm has a smaller cross-sectional area than the wider cold arm. Due to the differential Joule heating, the hot arm will expand at a higher rate than the cold arm. Consequently, the hot arm will deflect the heatuator's tip, while using the flexure as a pivoting point, in the direction shown in Figure 4.4. In fact, any modification to a thermally based actuator that increases the temperature difference between the hot and cold arm will automatically increase the device's overall efficiency.

In addition to is relatively simple design and operating principles, the lateral thermal actuator can exert a significant amount of force at its moveable tip. The modeling of the actuation force simplifies the 2-D system to a 1-D one by decomposing the thermal actuator into three serially interconnected lineshape microbeams. The objective of this analysis is to determine the heat distribution along each of these three basic components. The heat transfer boundary conditions are such that the MEMS anchors are fixed at room temperature and heat dissipation occurs primarily through air to the substrate. In addition, equation 4.4 above assumes that resistive heating power generated inside a differential element of length Δx, width w, and thickness h is equal to heat conduction out of the element under steady-state conditions. The model is based upon Laplace's equation for heat conduction with internal heat generation [25, 26] as noted in work done by N. K. S. Lee et al. [27].

$$-k_p wh\left[\frac{dT}{dx}\right]_x + J^2 \rho wh \cdot \Delta x = -k_p wh\left[\frac{dT}{dx}\right]_{x+\Delta x} + S \cdot \Delta x w \frac{T - T_S}{R_T} \qquad \text{Equation 4.4}$$

where T is the operating temperature, T_s is the substrate temperature, k_p is the thermal conductivity of polysilicon, J is the current density, S is the shape factor, R_T is the thermal resistance between the polysilicon microbeam and the substrate, and ρ is the thermally dependant resistivity of polysilicon. The shape factor accounts for the effect of a given element's shape upon heat conduction to the substrate. Taking the limit as $\Delta x \rightarrow 0$, we obtain the following:

$$k_p \frac{d^2T}{dx^2} + J^2\rho = \frac{S(T - T_S)}{hR_T}$$

Equation 4.5

Changing variables for equation 4.5 results with:

$$\frac{d^2\theta}{dx^2} - m^2\theta(x) = 0$$

Equation 4.6

Resulting with the following substitutions:

$$\theta(x) = T(x) - T_\theta$$

Equation 4.7

$$T_\theta = T_S + \frac{J^2\rho_0}{k_p m^2}$$

Equation 4.8

$$m^2 = \frac{S}{k_p h R_T} - \frac{J^2\rho_0\xi}{k_p}$$

Equation 4.9

where ξ is the linear temperature coefficient and is related to ρ. Upon solving equation 4.6 and applying the solution to the hot arm, cold arm, and the flexure, we obtain the three following temperature distribution functions:

$$T_h(x) = T_H + c_1 e^{m_h x} + c_2 e^{-m_h x}$$

Equation 4.10

$$T_C(x) = T_C + c_3 e^{m_C x} + c_4 e^{-m_C x}$$

Equation 4.11

$$T_f(x) = T_f + c_5 e^{m_f x} + c_6 e^{-m_f x}$$

Equation 4.12

It should be noted that equations 4.7 to 4.9 are generic and apply equally to the hot arm, cold arm, and flexure. Hence, the expressions for the variables used in equations 4.10 to 4.12 are obtained by substituting in the correct component-specific values for m and T_θ. The expressions for c_1 to c_6 are expressed in a matrix format in [27].

Once the expressions specifying the temperature distribution have been obtained, the change in the length, due to thermal expansion, of the hot arm, cold arm, and the flexure may be expressed as follows:

$$\Delta L_h = \alpha L_h (T_{hav} - T_S) \qquad \text{Equation 4.11}$$

$$\Delta L_c = \alpha L_c (T_{cav} - T_S) \qquad \text{Equation 4.12}$$

$$\Delta L_f = \alpha L_f (T_{fav} - T_S) \qquad \text{Equation 4.13}$$

where α is the coefficient of thermal expansion of polysilicon. T_{hav}, T_{cav}, and T_{fav} are the average temperatures [27] of the hot arm, cold arm, and the flexure, respectively. The expressions for T_{hav}, T_{cav}, and T_{fav} depend upon the previously calculated values of c_1 through c_6 and are a function of the current density J, after all other variables are replaced by their numerical values. Hence, the link between the fundamental properties of polysilicon, device geometry, observed expansion, and the subsequent deflection.

Once ΔL_h, ΔL_c, and ΔL_f are known, both the deflection force and the tip displacement may be calculated. The expected force [21] is the product of the difference in length between the expanded hot and cold arms, DT, and a spring-like restoring coefficient, k.

$$F = k \cdot DT \qquad \text{Equation 4.14}$$

$$DT = (L_h + \Delta L_h) - (L_c + \Delta L_c) \qquad \text{Equation 4.15}$$

$$k = \frac{EA}{L} \qquad \text{Equation 4.16}$$

where E is Young's modulus for polysilicon and equals 160 GPa [24], A is the cross-sectional area of the hot arm, and L is its original unstretched length. The design of a heatuator is incomplete without knowledge of the estimated tip displacement, D. Using the method of virtual work [28], an expression for D may be derived. The displacement, which depends on the hot arm's moment of inertia I_h, length L_h, and Young's Modulus through the following equation:

$$D = \frac{L_h^2}{6EI_h}\left(X_1 L_h - 3X_3\right) \qquad \text{Equation 4.17}$$

where

$$I_h = \frac{hw_h^3}{12} \qquad \text{Equation 4.18}$$

and X_1 and X_3, which are called "redundants" [27], are a function of the thermally induced changes in the lengths of the heatuator, ΔL_h, ΔL_c, and ΔL_f.

After further examination, the interdependence of the variables and their impact upon device performance characteristics becomes clear. Design tradeoffs include decreasing the maximum tip deflection versus increasing the output force by lengthening the flexure [24]. Next, a decrease in the gap, g, between the cold and hot arms will increase the observed deflection while reducing the output force of the actuator [24]. The lateral thermal actuator can be customized for a given design by optimizing [30] the values assigned to the aforementioned variables. Actually, the ratio of the hot and cold arms widths should be greater than four but smaller than seven since no great gain is made in either force or observed displacement otherwise [24]. Despite the fact that both a relatively high displacement and deflection force cannot be realized simultaneously through one design, the heatuator has nevertheless found applications in many areas. The latter is due to the thermal actuator's versatility, high reliability, and long useful life [24].

The actuation of gear-driven systems [33] and the control of scanning micro mirrors [36] are only a couple of the ways in which a lateral thermal actuator may be put to work. Thermally induced lateral motion has also been accomplished through controlled resistive heating [34] and by taking advantage of the deformations produced by localized thermal stresses in the structure [35].

4.4 Vertical Actuation Techniques

4.4.1 Electrostatic Actuation

In section 4.3.1.1, vertical deflection of comb drive fingers was being suppressed such that almost all of the generated electrostatic force could be used for lateral actuation. Electrostatically operated parallel plate actuators apply the same theory to optimize vertical motion. In general, only one of the two plates moves in the vertical direction while the second plate at the base is set to a fixed potential as shown in Figure 4.5 below. The upper plate is attached to four supporting corner posts by tethers that act as springs [32].

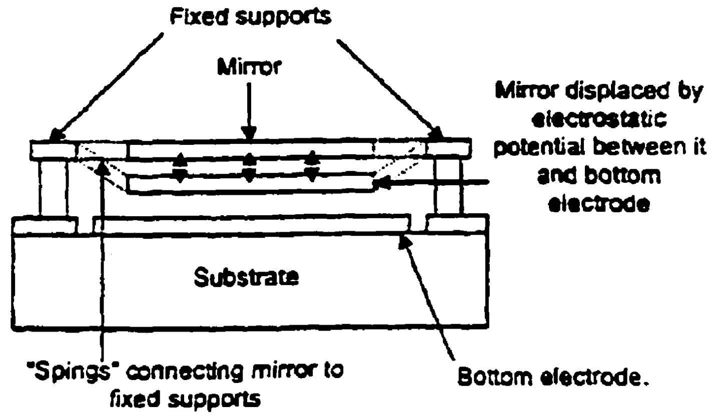

Figure 4.5: Schematic drawing of a micromirror structure. [43]

In order to avoid the onset of a phenomenon known as "pull-down", which will be discussed later in this section, knowledge of the mobile plate's location in the vertical Z-plane, for a given applied voltage V, is imperative. Firstly, the total electrostatic force for an ideal parallel plate capacitor [29] may be expressed as:

$$F_E = \frac{\varepsilon_0 E^2 A}{2} \qquad \text{Equation 4.19}$$

where ε_0 is the dielectric constant of free space, A is the area of the mirror, and E is the electric field intensity at any point in the space between the active surface and the bottom electrode. After accounting for the effects of electric field fringing and other losses related to the presence of etch holes in the mirror surface [38], the net electrostatic force, F_E, acting on the mirror in the direction of the bottom electrode may be written as:

$$F_E = \frac{\varepsilon_0}{2}[1 - \Delta f]\iint\left(\frac{V}{z_m(x,y)}\right)^2 dxdy \qquad \text{Equation 4.20}$$

where Δf is the total loss and $z_m(x,y)$ is a function that represents the vertical separation between the mirror and the bottom electrode at any point on the mirror surface [38]. Due primarily to mirror deformations, this function can be expected to be non-uniform. By equating the electrostatic force, of equation 4.20, with the summed restoring force of the four corner suspension springs, k, the distance between the mirror and the bottom electrode, d_f, may be isolated to result with the following equation [38]:

$$d_f = \frac{\varepsilon_0 V^2}{2k}(1 - \Delta f)\left(z_m^{-2}(x,y)dxdy\right) \qquad \text{Equation 4.21}$$

A phenomenon known as "pull-down", which is also present in literature as "pull-in", limits the performance of any parallel plate actuator by limiting the vertical travel distance to no more than 1/3 of the undeflected gap distance [41]. As the name implies, the suspended plate is "pulled down" to the substrate's surface should this vertical traveling distance be exceeded. Once a short circuit is created because of the contact with the electrically grounded substrate, controllable electrostatic deflection will no longer be possible. Due to the phenomenon's significance, attempts to characterize [39] and overcome pull-in by optimally balancing actuation speed and consumed energy [40] have been undertaken. In addition, extending the travel range of vertical electrostatic actuators to 3/5 of the undeflected gap distance has been analytically demonstrated through "leveraged bending" and "strain stiffening" methods [41].

Such improvements would greatly extend the applications of micromirrors in areas such as adaptive optics [42] and spatial light modulation [43]. Electrostatic MEMS are not limited to deflecting lightweight elements, such as a mirror, along the vertical Z-axis. Arrays of torsionally suspended electrostatic devices have successfully displaced macroscopic flat objects up to 5 μm, where each device was capable of outputting a force of 10 μN, through the generation of directional force fields [45].

4.4.2 Thermal Actuation

The two vertical actuation schemes that will be presented also rely upon the differential heating of two arms that are attached at a mobile end. The two unattached extremities are independently anchored, much like the lateral heatuator. However, instead of placing the polysilicon arms adjacent to one another, they are placed on top of one another such that lateral deflection may be converted into vertical motion.

4.4.2.1 Backward Bending Thermal Actuator

In the case of the backward bending vertical thermal heatuator [44] of Figure 4.6, the wider cold arm is located below the narrower hot arm. As the hot arm expands, it will drive the cold arm into the substrate. After the cold arm impacts the surface, the accumulating thermal energy can no longer be dissipated through actuation. As a result, the hot arm will heat up to a point after which the polysilicon will begin to reflow. As a result of this phase transformation, a permanently upward pointing bow, that decreases the effective length of the hot arm, will form as shown in Figure 4.7 on the following page. Therefore, when current is no longer applied to the system, the tip of the actuator will deflect back upwards and past its initial resting position. This actuation scheme is referred to as backbending. [46]

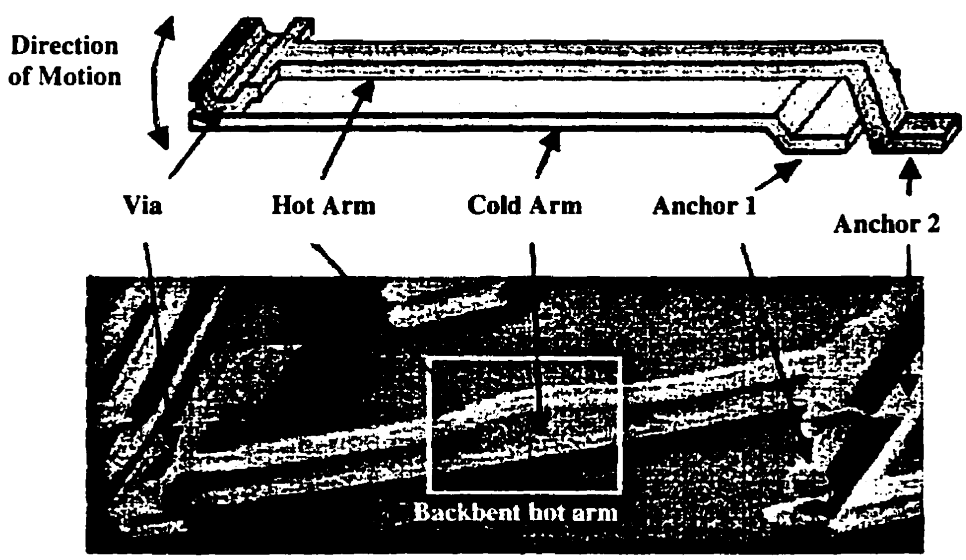

Figure 4.6: Vertical backbending thermal actuator. [47]

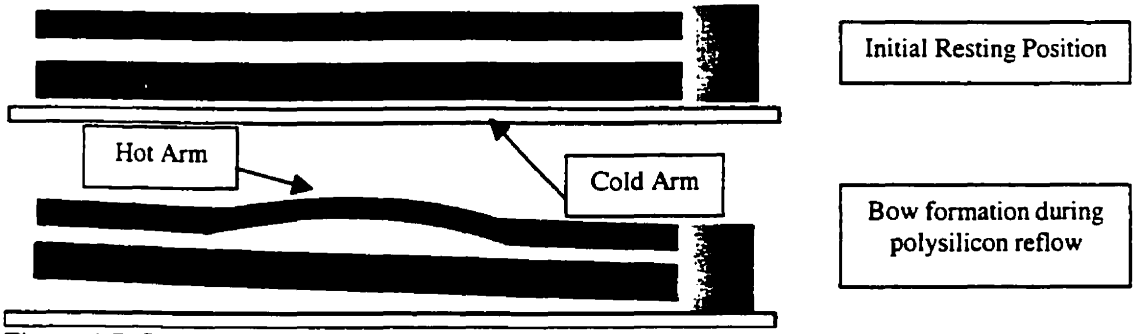

Figure 4.7: Schematic of the backbending phenomenon.

Another irreversible vertical actuation technique uses thermally induced surface tension in a calculated volume of solder to erect plates up to a desired angle [48]. Other reversible thermally based actuation approaches exist. The first is a bimorph assembly that consists of two arms, with no gap in between them, which are composed of two different materials [49]. Others strategies have been used to deflect objects in the vertical direction through the use of integrated thermally buckling serpentine structures [50] and beams [51]. All the previously discussed actuation schemes will displace an object in the positive z-direction. A newly proposed bimorph membrane-like MEMS is reported to bend a membrane by 50 μm and 15 μm in the positive and negative z-directions, respectively [52].

4.4.2.2 Forward Bending Thermal Actuator

The forward bending thermal actuator that we propose here, and for which a Report of Invention (ROI) has been filed, is a novel vertical deflection actuator [54]. The concept will be presented in this section while the testing results will be analyzed in chapter 6. The forward bending thermal actuator combines the operating principles of both the lateral thermal actuator and the backbending vertical thermal actuator. From the latter, it inherits the concept of stacking the arms instead of placing them adjacent to one another. However, in the case of the forward bending thermal actuator, the Hot Arm is placed below the Cold Arm, not above it, as shown in Figure 4.8. The objective being to allow for the implementation of an actuator that not only displaces its moveable tip upwards but moves vertically in a controlled and repeatable manner also.

Repeatable performance is insured, provided that the device's operating requirements and dynamic characteristics are known prior to applying any electrical stimulus. Any thermally actuated device will be permanently damaged if it overheats, through structural reflow. The thermal reflow of any polysilicon structure, which leads to backbending, is a function of the structure's geometry and the applied DC current. Hence, testing and use of any device must not exceed the point at which thermal energy begins to accumulate within the structure.

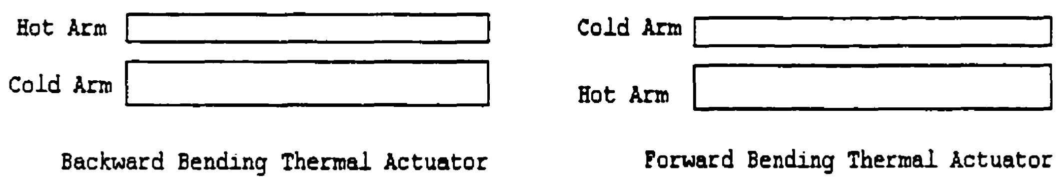

Figure 4.8: Cross sectional views of both the Backward and Forward bending heatuators.

This being said, the forward bending vertical thermal actuator will return back to its original zero position, without exhibiting any irreversible deformations, if it is operated within an acceptable current and voltage regime.

The similarities between this actuator and the lateral thermal actuator concerned the geometry of the Cold Arm. In essence, the idea of using a flexure was applied to make it easier for the underlying Hot Arm to push the Cold Arm upwards. The two layers of a typical forward bending thermal actuator are shown in Figure 4.9 to better illustrate the device geometry and operation.

The device has a hot arm length of 200 μm, cold arm length of 165 μm that is linked to a 35 μm long flexure. The hot arm and flexure widths equal 2 μm while that of the cold arm is 14 μm. The gap, g, between the hot and cold arm cannot be a design variable anymore because the process used determines it. The gap g equals 0.75 μm [55] as opposed to 2 μm. The hot arm thickness is 2.0 μm and that of the cold arm is 1.5 μm [56]. Note that these numbers were chosen to be almost identical to those used in the design of the lateral thermal actuator. This was done in order to investigate any correlation between the lateral and forward bending thermal actuators. As was the case with the lateral thermal actuator, these parameters may be modified to satisfy the needs of a given set of design criteria.

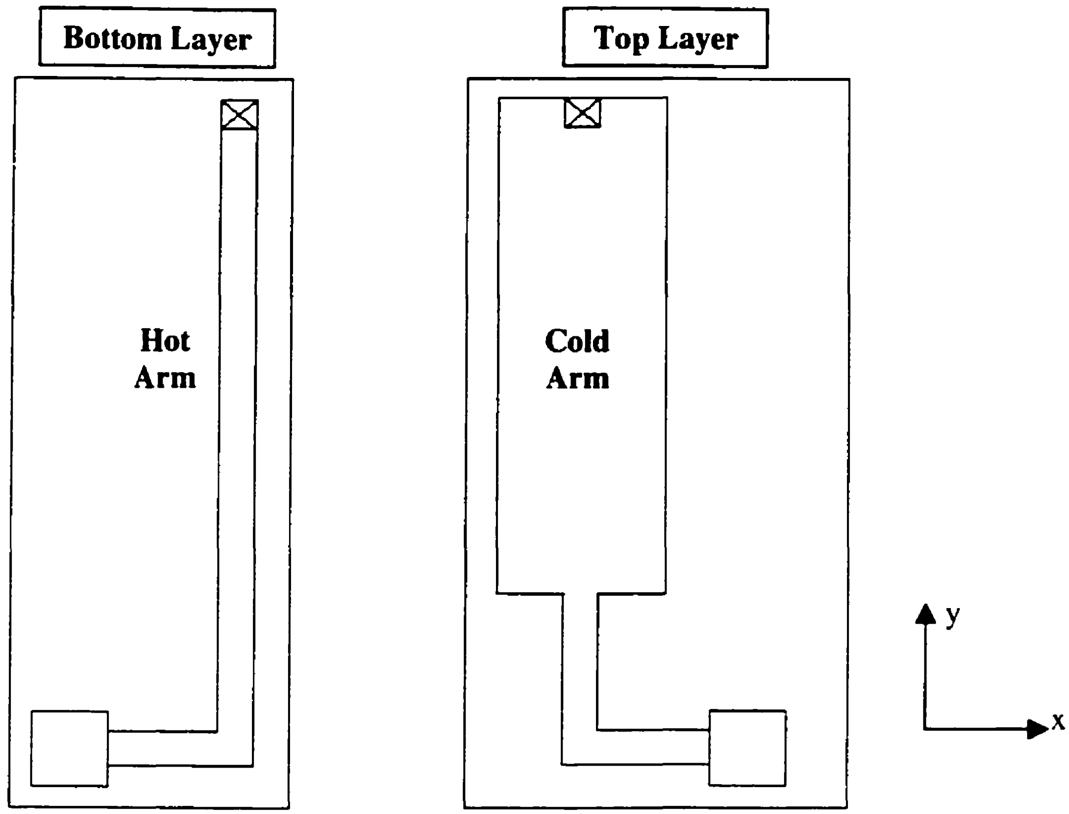

Figure 4.9: The bottom and top layers of a forward bending vertical thermal actuator.

The Forward Bending Vertical Thermal Actuator is expected to consume more power than its laterally moving counterpart due to cold arm's larger resistance to vertical motion. Although an attempt was made to compare a lateral and a vertical actuator of a common geometry to one another, it was not possible. Because the heat conduction paths in each case were not identical, the theoretical displacement and force versus current curves were dissimilar.

To investigate the theoretical operation, the lateral thermal actuator was simplified into three microbeam one-dimensional structures, the hot arm, cold arm, and flexure, which were each modeled independently until the actual force and displacement were calculated. In the same way, a model of the vertical thermal actuator will be established by using the same equations while replacing the geometry-dependant variables wherever necessary. These changes are caused because both the first and second structural layers are used. The vertical thermal actuator model will start, once again, with the assumption that under steady-state conditions, the heat power generated in the element is equal to the heat it outputs through conduction.

$$-k_p wh\left[\frac{dT}{dx}\right]_x + J^2 \rho wh \cdot \Delta x = -k_p wh\left[\frac{dT}{dx}\right]_{x+\Delta x} + S_V \cdot \Delta x w \frac{T - T_S}{R_{TV}} \qquad \text{Equation 4.22}$$

where T is the operating temperature, T_s is the substrate temperature, k_p is the thermal conductivity of polysilicon, J is the current density, S is the shape factor, R_T is the thermal resistance between the polysilicon microbeam and the substrate, and ρ is the thermally dependant resistivity of polysilicon. S and R_T are the only variables that are affected by the new geometry and have been renamed as S_V and R_{TV}, respectively.

$$R_{TV} = \frac{t_V}{k_V} + \frac{t_N}{k_N} \qquad \text{Equation 4.23}$$

and

$$S_V = \frac{h}{w}\left(\frac{2t_V}{h} + 1\right) \qquad \text{Equation 4.24}$$

where t_V and t_N are the elevation of the 1-D microbeam above the nitride and the thickness of the insulating nitride layer, respectively. The value of t_V will equal 2.50 μm when the first structural layer is used (POLY1), and equals 5.25 μm when using the second structural layer (POLY2).

The thickness of a microbeam element is specified by h, whereas w represents its width. The fabrication process used determines the values for h; the Multi-User MEMS Process (MUMPs) that was discussed in section 3.3.1 in this case. When POLY1 is used, h = 2.0 μm and equals 1.5 μm when using POLY2 [55]. Therefore, the values assigned to S_V and R_{TV} will now also depend upon the structural layer used, through t_V and t_N, in addition to the device geometry, through h and w. As a result, the shape factor and thermal resistance will be different for each microbeam element. The expressions are identical to those presented when the lateral thermal actuator was studied in section 4.3.2. As was mentioned earlier, the existence and nature of heat conduction paths between the hot and cold arms and between the vertical thermal actuator and the substrate influences greatly the device's range of vertical motion.

By placing the cold arm on the second layer, the value of t_V will increase by 2.75 μm, which will cause the ratio of S_V to R_{TV}, within the first term of equation 4.26, to grow.

$$T_\theta = T_S + \frac{J^2 \rho_0}{k_p m_V^2} \qquad \text{Equation 4.25}$$

$$m_V^2 = \frac{S_V}{k_p h R_{TV}} - \frac{J^2 \rho_0 \xi}{k_p} \qquad \text{Equation 4.26}$$

Hence, the value of the parameter *m is* directly related to the value of t_V. The larger value of m_{vc} will cause the average temperature of the cold arm, T_{CAV}, to decrease while that of the hot arm, T_{HAV}, remains unchanged. A larger temperature differential will result between the hot arm and cold arm of the vertical thermal actuator. Experimentally, a significant vertical deflection was expected because. the enhanced thermal difference implied a more efficient dynamic characteristics by definition.

The Forward Bending Vertical Thermal Actuator is predicted to be capable of supporting a load many times its own weight despite the fact that no arrayed vertical actuators were loaded with a mass and tested. The latter statement is based upon the performance of a similar thermally activated device [50] that is reported to have lifted a mass 1000 times its own by using electrothermal buckling effects. These operating characteristics are highly desirable and will augment the device's industrial potential.

Figure 4.10, on the next page, illustrates the arcing motion in the vertical plane, which was observed Therefore, this invention can achieve efficient, precise, variable, and repeatable displacement in the positive z-direction provided it is operated correctly.

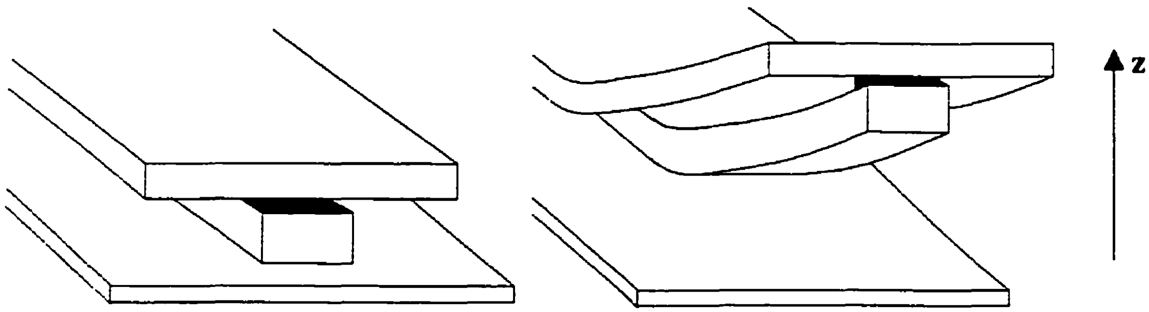

Figure 4.10: Schematic of an inactive and a vertically deflected forward bending heatuator.

It should be noted that certain applications might not be compatible with a device that moves along an arced path instead of one that is strictly perpendicular to the substrate. This non-rectilinear motion may cause the actuator's tip to slip along the target's surface until a point of equilibrium is reached between it and the other active vertical actuators. This is due to the fact that the vertical actuator transfers its kinetic energy purely through contact, without the use of any mechanical link between it and the target to be moved.

4.5 References

1. Advances in Actuators, A.P. Dorey and J. H. Moore, Sensors Series, Institute of Physics Publishing Bristol and Philadelphia, pp. 113-116, 1995.
2. IBID, 1, p. 114.
3. IBID, 1, p. 115.
4. W. S. N. Trimmer, "Microrobots and Micromechanical Systems", Sensors and Actuators, Vol. 19, No.3, pp. 267-287, September 1989.
5. W. C. Tang, T.-C. H. Nguyen, and R. T. Howe, "Laterally Driven Polysilicon Resonant Microstructures", Proceedings of Investigation of Micro Structures, Sensors, Actuators, Machines and Robots, pp. 53-59, 1989.
6. M.-H. Kiang, O. Solgaard, K. Y. Lau, and R. S. Muller, "Electrostatic Combdrive-Actuated Micromirrors for Laser-Beam Scanning and Positionning", Journal of Microelectromechanical Systems, Vol. 7, No. 1, pp. 27-37, March 1998.
7. A. P. Lee and A. P. Pisano, "Polysilicon Angular Microvibromotors", Journal of Microelectromechanical Systems, Vol. 1, No. 2, pp. 70-76, June 1992.
8. V. P. Jaecklin, C. Linder, N. F. de Rooij, J. M. Moret, R. Bischof, and F. Rudolf, "Novel Polysilicon Comb Actuators for XY-Stages", Micro Electro Mechanical Systems '92 Conference Proceedings, pp. 147-149, February 1992.
9. R. Legtenberg, A. W. Groenveld, and M. Elwenspoek, "Comb-Drive Actuators for Large Displacements", Journal of Micromechanics and Microengineering, Vol. 6, pp. 320-329, 1996.
10. W. A. Johnson and L. K. Warne, "Electrophysics of Micromechanical Comb Actuators", Journal of Microelectromechanical Systems, Vol. 4, No.1, pp. 49-59, 1995.
11. W. C. Tang, M. G. Lim, and R. T. Howe, "Electrostatic Comb Drive Levitation and Control Method", Journal of Microelectromechanical Systems, Vol. 1, No. 4, pp. 170-178, June 1992.
12. J.-L. Yeh, C.-Y. Hui, and N. C. Tien, "Electrostatic Model for an Asymmetric Combdrive", Journal of Microelectromechanical Systems, Vol. 9, No. 1, pp. 126-135, June 1992.

13. W. Ye, S. Mukherjee, and N. C. MacDonald, "Optimal Shape Design of an Electrostatic Comb Drive in Microelectromechanical Systems", Journal of Microelectromechanical Systems, Vol. 7, No. 1, pp. 16-26, March 1998.
14. M. A. Rosa, S. Dimitrijev, and H. B. Harrison, "Improved Operation of Micromechanical Comb-Drive Actuators Through the Use of New Angled Comb Finger Design", Journal of Intelligent Material Systems and Structures, Vol. 9, pp. 283-290, April 1998.
15. W.-T. Hsu and C. T.-C. Nguyen, "Geometric Stress Compensation for Enhanced Thermal Stability in Micromechanical Resonators", IEEE Ultrasonic Symposium, pp. 945-948, 1998.
16. S. G. Adams, F. M. Bertsch, K. A. Shaw, and N. C. MacDonald, "Independent Tuning of Linear and Nonlinear Stiffness Coefficients", Journal of Microelectromechanical Systems, Vol. 7, No. 2, pp. 172-180, June 1998.
17. T. Hirano, T. Furuhata, K. J. Gabriel, H. Fujita, Design, Fabrication, and Operation of Submicron Gap Comb-Drive Microactuators", Journal of Microelectromechanical Systems, Vol. 1, No. 1, pp. 52-59, March 1992.
18. R. R. A. Syms, B. M. Hardcastle, and R. A. Laws, "Bulk Micromachined Silicon Comb-Drive Electrostatic Actuators with Diode Isolation", Sensors and Actuators, A 63, pp. 61-67, 1997.
19. T. Akiyama, D. Colard, and H. Fujita, "Scratch Drive Actuator with Mechanical Links for Self-Assembly of Three-Dimensional MEMS", Journal of Microelectromechanical Systems, Vol. 6, No. 1, pp. 10-17, March 1997.
20. P. Langlet, D. Collard, T. Akiyama, and H. Fujita, "A Quantitative Analysis of Scratch Drive Actuation for Integrated X/Y Motion System", Proceedings of the International Conference on Solid-State Sensors and Actuators, pp. 773-776, June 1997.
21. J. R. Reid, V. M. Brihgt, and J. H. Comtois, "Force Measurements of Polysilicon Thermal Micro-Actuators",
22. Y. Fukuta, D. Collard, T. Akiyama, E. H. Yang, and H. Fujita, "Microactuated Self-Assembling of 3D Polysilicon Structures with Reshaping Technology", Proceedings of the Tenth Annual Workshop on MEMS, pp. 477-481, 1997.

23. P. Minotti, G. Bourbon, P. Langlet, and T. Masuzawa, "Arrayed Electrostatic Scratch Drive Acuators: Toward Visible Effects up to the Human Scale", Journal of Intelligent Materials Systems and Structures, Vol. 9, pp. 837-846, October 1998.
24. J. H. Comtois, V. M. Bright, and M. W. Phipps, "Thermal Microactuators for Surface-Micromachining Processes", SPIE, vol. 2642, pp. 10-21, 1995.
25. Personal conversation with Mr. Paul Kladitis of the University of Colorado.
26. Fundamentals of Heat and Mass Transfer, 3rd edition, F. P. Incropera and D. P. De Witt, John Wiley & Sons, New York, pp.108-114, 1990.
27. Q.-A. Huang and N. K. S. Lee, "Analysis and Design of Polysilicon Thermal Flexure Actuator", Journal of Micromechanics and Microengineering, Vol. 9, pp. 64-70, 1999.
28. Vector Mechanics for Engineers: Statics, F. P. Beer and E. R. Johnston Jr., McGraw Hill Inc., New York, pp. 429-432, 1990.
29. Engineering Electromagnetic Fields and Waves, 2nd edition, C. T. A. Johnk, John Wiley & Sons, New York, p. 244, 1988.
30. Q.-A. Huang and N. K. S. Lee, "Analytical Modeling and Optimization for a Laterally-Driven Polysilicon Thermal Actuator", Microsystem Technologies, Vol.5, No.3, pp.133-137, 1999.
31. J. H. Comtois, M. A. Michalicek, amd C. C. Barron, "Characterization of Electrothermal Actuators and Arrays Fabricated in a Four-Level, Planarized Surface-Micromachined Polycrystalline Silicon Process", Proceedings of the International Conference on Solid-State Sensors and Actuators, pp. 769-772, June 1997.
32. D. M. Burns and V. M. Bright, "Design and Performance of a Double Arm Polysilicon Thermal Actuator", SPIE Proceedings, Vol. 3224, pp. 296-306, 1997.
33. J. H. Comtois and V. M. Bright, "Surface Micromachined Polysilicon Thermal Actuator Arrays and Applications", Proceedings of the International Conference on Solid-State Sensors and Actuators, pp. 174-177, June 1996.
34. J. W. Judy, T. Tamagawa, and D. L. Polla, "Surface Micromachined Linear Thermal Microactuator", International Electron Devices Meeting Technical Digest, pp. 629-632, 1990.

35. L. Que, J.-S. Park, and Y. B. Gianchandani, "Bent-Beam Electro-Thermal Actuators for High Force Applications", Proceedings of the Twelfth IEEE International Conference on Micro Electro Mechanical Systems, pp. 552 –555, 1999.

36. J. R. Reid, V. M. Bright, and J. H. Comtois, "Arrays of Thermal Actuators Coupled to Micro-Optical Components", SPIE, Vol. 2685, pp. 74-82, 1996.

37. M. A. Michalicek, D. E. Sene, V. M. Bright, "Advanced Modeling of Micromirror Devices", Proceedings of Integrated Micro/Nanotechnology for Space Applications, NASA and Aerospace Press, pp. 214-229, October 1995.

38. M. A. Michalicek, V. M. Bright, J. H. Comtois, "Design, Fabrication, Modeling, and Testing of a Surface-Micromachined Micromirror Device", Proceedings of ASME, DSC Vol. 57-2, pp. 981-988, 1995.

39. O. Degani, E. Socher, A. Lipson, T. Leitner, D. J. Setter, S. Kaldor, and Y. Nemirovsky, "Pull-In Study of an Electrostatic Torsion Microactuator", Journal of Microelectromechanical Systems, Vol. 7, No. 4, pp. 373-379, December 1998.

40. L. M. Castañer and S. D. Senturia, "Speed-Energy Optimization of Electrostatic Actuators Based on Pull-In", Journal of Microelectromechanical Systems, Vol. 8, No. 3, pp. 290-298, September 1999.

41. E. S. Hung and S. D. Senturia, "Extending the Travel Range of Analog-Tuned Electrostatic Actuators", Journal of Microelectromechanical Systems, Vol. 8, No. 4, pp. 497-505, December 1999.

42. W. D. Cowan, M. K. Lee, B. M. Welsh, V. M. Bright, and M. C. Roggemann, "Surface Micromachined Segmented Mirrors for Adaptive Optics", Journal of Selected Topics in Quantum Electronics, Vol. 5, No. 1, pp. 90-101, Jan./Feb. 1999.

43. R. J. T. Bunyan, D. O. King, R. A. Wilson, and A. M. Scott, "Design, Modeling, and Evaluation of Micro-Mirrors", IEE Seminar on Microengineering, Modeling, and Design (Ref. No. 1999/052), pp. 3/1 -3/3, 1999.

44. V. M. Bright and W. D. Cowan, "Vertical Thermal Actuators for Micro-Opto-Electro-Mechanical Systems", SPIE, Vol. 3226, pp. 137-146, 1997.

45. K.-F. Böhringer, B. R. Donald, and N. C. MacDonald, "Single-Crystal Silicon Actuator Arrays for Micro Manipulation Tasks", Proceedings of the Ninth Annual International Workshop on Micro Electro Mechanical Systems, pp. 7-12, 1996.

46. J. R. Reid, J. H. Comtois, V. M. Bright, "Automated Assembly of Flip-Up Micromirrors", International Conference on Solid-State Sensors and Actuators, pp. 347-350, June 16-19, 1997.
47. V. M. Bright, University of Colorado, "Surface Micromachined Optical Systems", Power Point presentation, Slide No. 22, 2000, http://mems.colorado.edu/c1.res.ppt/ppt/oe.review/ppt.htm?.
48. R. R. A. Syms, "Equilibrium of Hinged and Hingeless Structures Rotated Using Surface Tension Forces", Journal of Microelectromechanical Systems, Vol. 4, No. 4, pp. 177-184, December 1995.
49. W. Riethmüller, W. Benecke, "Thermally Excited Silicon Microactuators", IEEE Transactions on Electron Devices, Vol. 35, No.6, pp.758-763, June 1988.
50. L. Lin, S.-H. Lin, "Vertically Driven Microactuators by Electrothermal Buckling Effects", Sensors and Actuators, A 71, pp. 35-39, 1998 Elsevier Science S.A. .
51. T. Seki, M. Sakata, T. Nakajima, M. Matsumoto, "Thermal Buckling Actuator for Micro Relays", 1997 International Conference on Solid-State Sensors and Actuators, pp. 1153-1156 , June 16-19, 1997.
52. C. Hsu and W. Hsu, "A Two-Way Memebrane-Type Micro-Actuator with Continuous Deflections", Journal of Micromechanics and Microengineering, No. 10, pp. 387-394, 2000.
53. P. Krulevitch, A. P. Lee, P. B. Ramsey, J. C. Trevino, J. Hamilton, and M. A. Northrup, "Thin Film Shape Memory Alloy Microactuators", Journal of Microelectromechanical Systems, Vol. 5, No. 4, pp. 270-282, December 1996.
54. F. S. J. Michael, "Forward Bending Vertical Thermal Actuator", Report of Invention submitted to the McGill University Office of Technology Transfer (OTT) on March 27^{th}, 2000, Ref. No 00101, 20 pages.
55. D. A. Koester, R. Mahadevan, A. Shishkoff, and K. W. Markus, "MUMPS™ Design Handbook", Cronos Integrated Microsystems, p.1, May 1999.
56. IBID, 52, p.10.

5 The Selection of a Fabrication Process and an Actuation Scheme

5.1 Introduction

Prior to presenting the actuator designs that may go on to enable the X-Y- θ and X-Y-θ-Z lenslet positioning stages, a fabrication process must be selected. Once that decision has been made, the fabrication-imposed limitations upon the design of all subsystems will be known. Moreover, the actuation technologies must also be selected to ensure their compatibility with the previously picked manufacturing process. For completeness, a schematic of the packaged lenslet positioning MEMS will be presented.

5.2 Schematic of the Packaged Lenslet Positioning MEMS

To motivate the chosen fabrication processes and actuation schemes, a schematic of the packaged lenslet array positioning MEMS is shown in Figure 5.1.

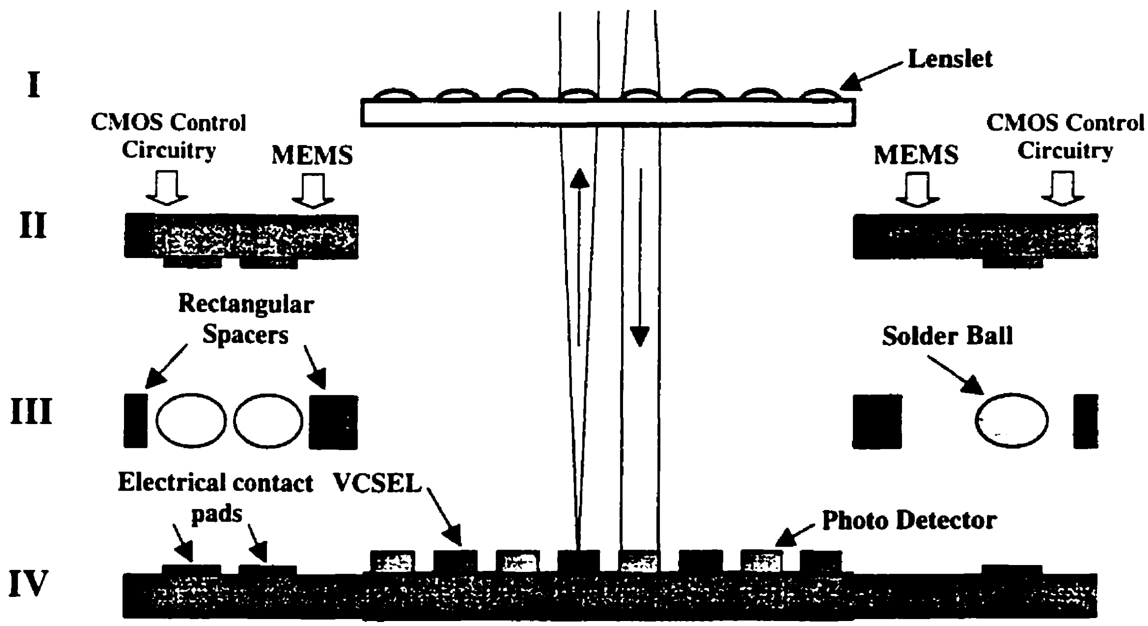

Figure 5.1: Schematic diagram of the proposed lenslet positioning MEMS.

The roman numerals to the left-hand side of the schematic refer to the four major functional layers of the lenslet positioning MEMS. The schematic is laid out in a top-down fashion with the lenslet array [I] at the top followed by the alignment structures [II], the 40.0 ± 2.0 μm metallic spacers [III] and the VCSEL/PD array [IV]. The remainder of the system's components will be revisited in section 7.3 entitled "Packaging and Assembly".

5.3 Fabrication Processes

Three fabrication processes will be required to completely manufacture functional layers II and III. Firstly, the LIGA technique of section 3.2.3, will be used to form the 40.0 ± 2.0 μm high metallic spacers that will provide the vertical actuators with a higher starting, or reference, plane relative to the substrate. Simultaneously, the rectangular hole at the center of layer III, through which light travels, will be formed. Further more, electrically conductive solder bumps, or balls, will align the layers relative to one another while relaying data between the electrical contact pads on layers II and IV.

Next, the lenslet aligning MEMS and their accompanying CMOS control circuitry will be fabricated by combining the SUMMiT V and the iMEMS processes discussed in sections 3.3.2 and 3.3.3, respectively. SUMMiT V will allow the designer to have access to four releasable structural layers while iMEMS will electrically interconnect CMOS circuitry to the MEMS in a single fabrication run. Consequently, eliminating the need to use more than one fabrication process, through the use of iMEMS, will offset the cost of requesting a high layer count.

5.4 Actuation Schemes

For any actuator to be a candidate, it must be able to firstly structurally support the lenslet array's static weight. Despite the lack of a finite element model (FEM) analysis package, such as ANSYS, the load bearing capability of a given MEMS actuator was evaluated. Next, to align the lenslet array optimally, motion in the X, Y, and Z planes must be accomplished in a controlled and repeatable fashion. These factors govern the selection of a useful actuator.

5.4.1 Lateral and Rotational Actuation

Although gravity is not a significant force at this microscopic scale, the deposition of a macroscopic object, of relatively significant weight, on the proposed MEMS will impair its operation. The lenslet array will push the actuation arms, which transfer the force generated by the actuator arrays to the target, into the substrate. In addition, the individual thermal actuators and a 250 x 250 μm^2 load, shown in Figure 5.2 below, were well released and could be moved with a probe tip. The diagonal beam across the center of the load was designed to keep the load on the wafer once the load had been released.

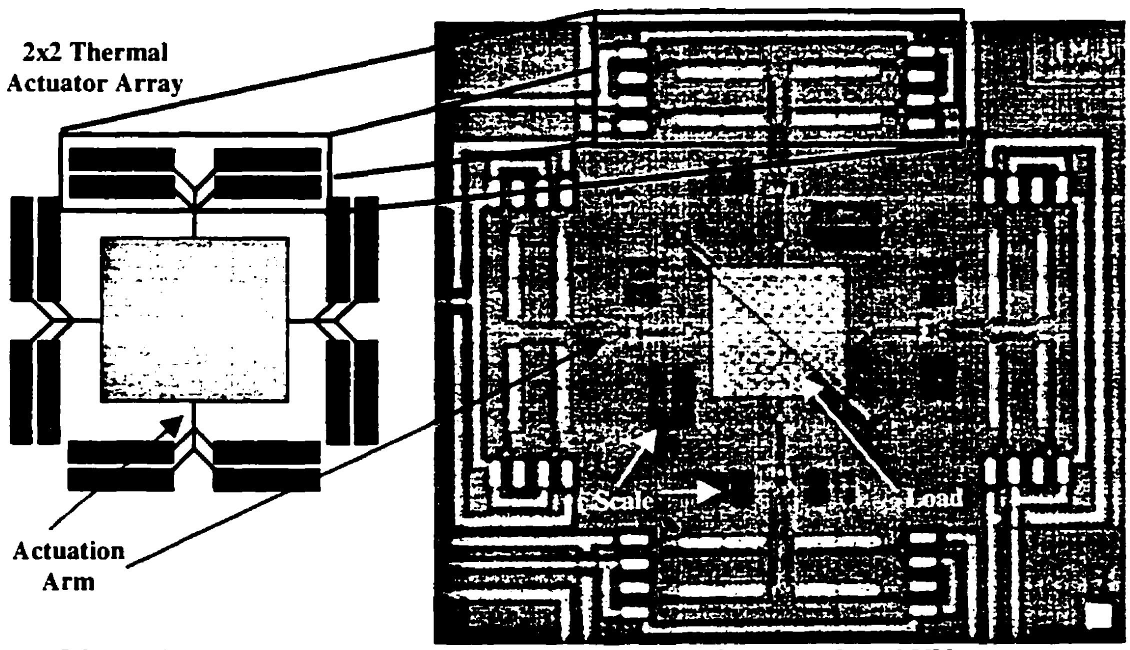

Figure 5.2: A schematic (left) and the layout (right) of a thermal actuator based XY stage.

However, an unloaded array of thermal actuators was unable to bend forward when a current was applied as shown in Figure 5.3. The actuators that are uncoupled to the actuation arm moved laterally when a stimulus was applied while the coupled pair on the left-hand side remained immobile. Although this may have been due to stiction, an unseen fracture in one of the numerous constituent electrically conductive serially interconnected segments of the 2 x 2 thermal actuator array, or an incorrectly designed actuation arm are probably the sources of failure. Based on these observations, thermal actuation should not be used to displace the lenslet array in the X-Y plane. Rotational motion was not observed due to non-functional thermal actuator arrays.

(a)

(b)

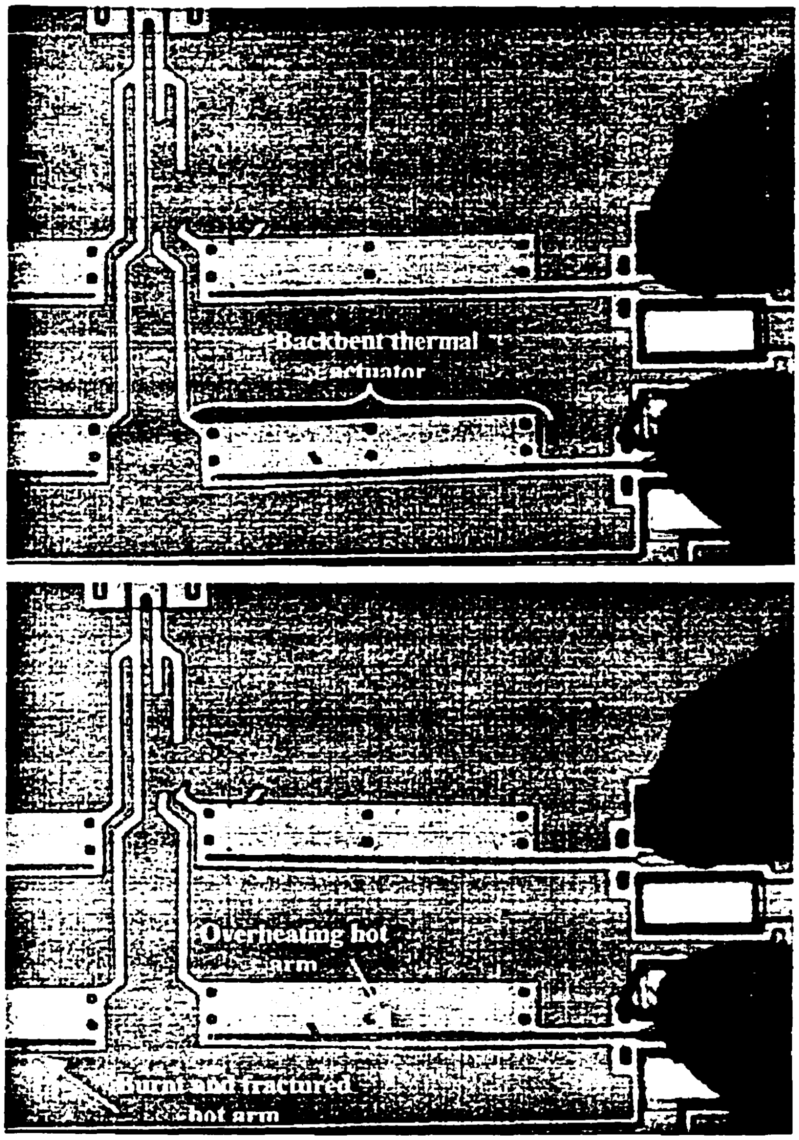

Figure 5.3: Decoupled 2x2 thermal actuator array (a) at rest and (b) in motion.

Controlled unequal deflections in the X and Y directions would have been the approach used. Details regarding the latter degree of freedom will be presented in section 6.3. Thermal actuators, presented in section 4.3.2, were originally chosen foremost because they are stable and exhibit very repeatable performance curves. Moreover, high actuation speed was unnecessary and no significant amount of hysteresis was noted during the cycling of individual lateral heatuators as will be demonstrated in the next chapter. Despite these desirable characteristics, the lateral thermal actuator was found to be unable to sustain and displace the weight of the 32.3 mg lenslet array.

A suitable replacement for the lateral thermal actuator should still be based upon thermal operating principles. Such an actuator has been demonstrated by Böhringer et al.

The MEMS was designed specifically to displace macroscopic objects in the XY plane and rotationally. It used a micromachined bimorph organic ciliary array to displace silicon pieces that were 0.55 mm or 0.10 mm thick and of varying geometries [1].

5.4.2 Vertical Actuation

In this case, thermally excited MEMS will be the actuation strategy of choice for reasons mentioned in the last section. Although it is the first time the vertical forward bending thermal actuator has been tested, it will be the device used to displace the lenslet in the positive z-direction. It has potential and currently meets displacement expectations without having been optimized or modeled. The experimental data gathered is presented in section 6.4.

Should the need for a reliable and tested solution be immediate, the backbending thermal actuator of section 4.4.2.1 is a reliable option. However, this scheme must be used cautiously since the backbending phenomenon is irreversible. Secondly, thermally excited clamped beams may be used to repeatedly displace the lenslet by up to 25 μm perpendicularly to the substrate [2]. Since the chip was designed assuming that thermal actuators would be used to implement all four degrees of freedom (X, Y, θ, Z), the next two chapters present experimental data that was gathered for the lateral and vertical thermal actuators only.

5.5 References

1. J. W. Suh, R. B. Darling, K. F. Böhringer, B. R. Donald, H. Baltes, and G. T. A. Kovacs, "CMOS Integrated Ciliary Actuator Array as a General-Purpose Micromanipulation Tool for Small Objects", Journal of Microelectromechanical Systems, Vol. 8, No. 4, pp. 483-496, December 1999.
2. T. Seki, M. Sakata, T. Nakajima, and M. Matsumoto, "Thermal Buckling Actuator for Micro Relays", Solid-State Sensors and Actuators Conference Proceedings, pp. 1153-1156, 1997.

6 Decoupled Actuation Analysis

6.1 Introduction

Both the lateral and vertical thermal actuators were tested. Unloaded lateral thermal actuators were tested in order to investigate the deflection versus current relationship using a particular device geometry. Eighty percent of devices tested exhibited a significant amount of stiction at startup only. This issue was resolved by gently moving the actuator manually using a probe tip before powering up the MEMS. Scales were used to measure lateral deflection where the bars within the scale were 2.0 μm wide and 2.0 μm apart from one another.

6.2 Lateral Motion in the X-Y Plane

All lateral heatuators that were tested were identical to the one shown in Figure 6.1(a) on the next page. The device was 200 μm in length where the lengths of the device's three major components were 35 μm, 165 μm, and 200 μm for the flexure, cold arm, and hot arm, respectively. In addition, the widths of the flexure, cold arm, and hot arm were 4 μm, 28 μm, and 4 μm, respectively. The width of the cold arm was wider than that of the hot arm by a factor of seven for reasons already mentioned in section 4.3.2. The gap between the hot and cold arms was maintained at 2 μm. The three squares located along the center of the cold arm are called dimples. They reduce stiction between the substrate and the cold arm by connecting them locally only. The actuator must then relieve these sources of local sticition by breaking the bond to the substrate and dragging the dimple along throughout its lateral motion.

The lateral heatuator could be stimulated with either a DC voltage or a DC current. When the lateral thermal actuator was tested using voltage, the device was found to oscillate by ±0.5 μm for approximately two seconds at random locations and times along its arced path. Following this, the actuator recoiled to a location that was up to 2.0 μm behind its location prior to the onset of the oscillations. As expected, this decrease in lateral deflection coincided with a 1.0 mA drop in current drawn by the device under test

(DUT). Next, the actuator returned to its original deflected location without any external intervention.

However, when a DC current was applied, the actuator's operation was more controllable and repeatable. Furthermore, sub-micron displacements were routinely observed particularly when the device's deflection was being reduced from a point of maximum deflection back down to its starting position. Figure 6.1(a) and (b) show a heatuator at rest and one that is deflected by 5.0 μm whereas Figure 6.1(c) illustrates the consequences of driving too much current through the device; backbending.

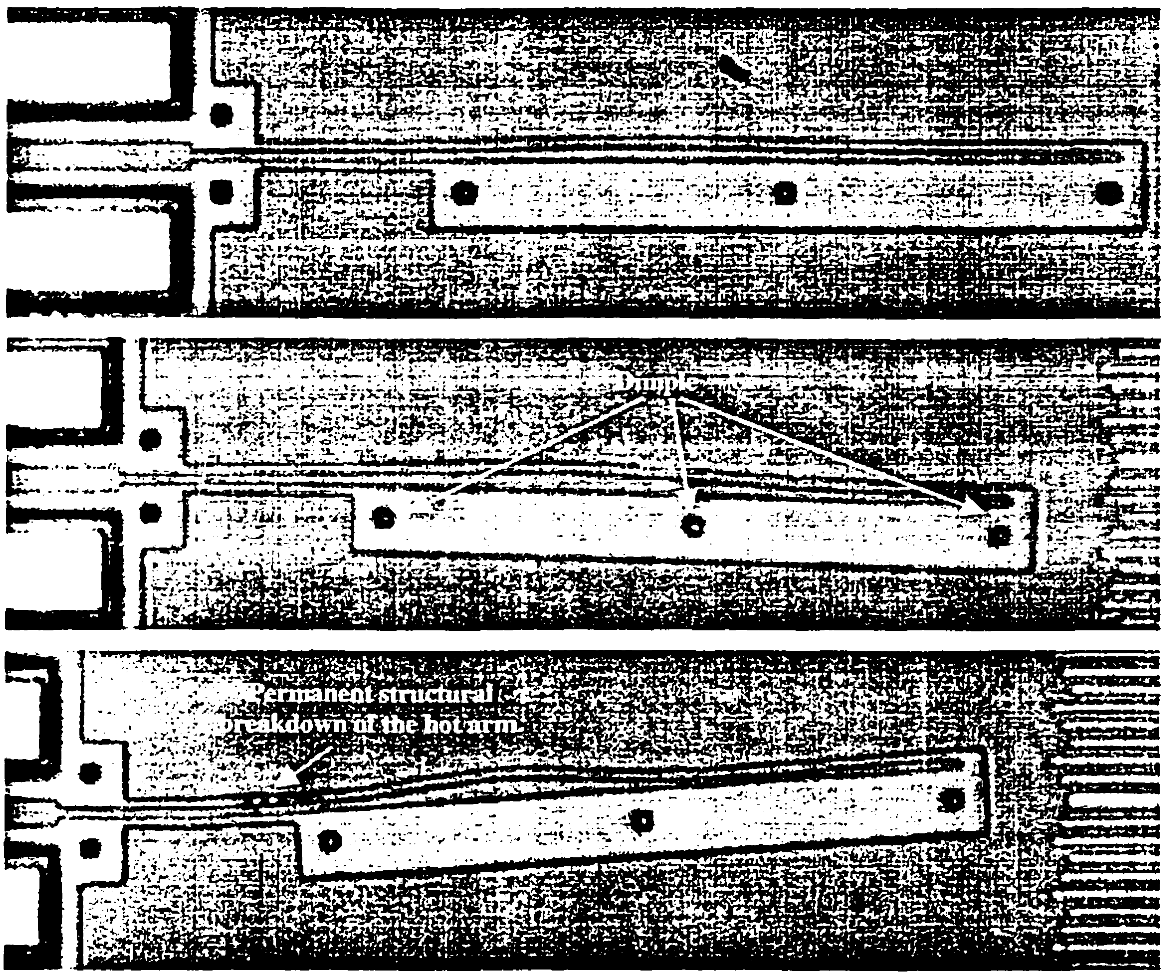

Figure 6.1: A thermal actuator (a) at rest, (b) deflected by 6.0±0.5 μm, and (c) backbent by 14.0±0.5 μm.

Firstly, one device was cycled three times to identify any variation in its displacement curve and in so doing assess the repeatability of its lateral motion. The resulting curves are shown in Figure 6.2 next.

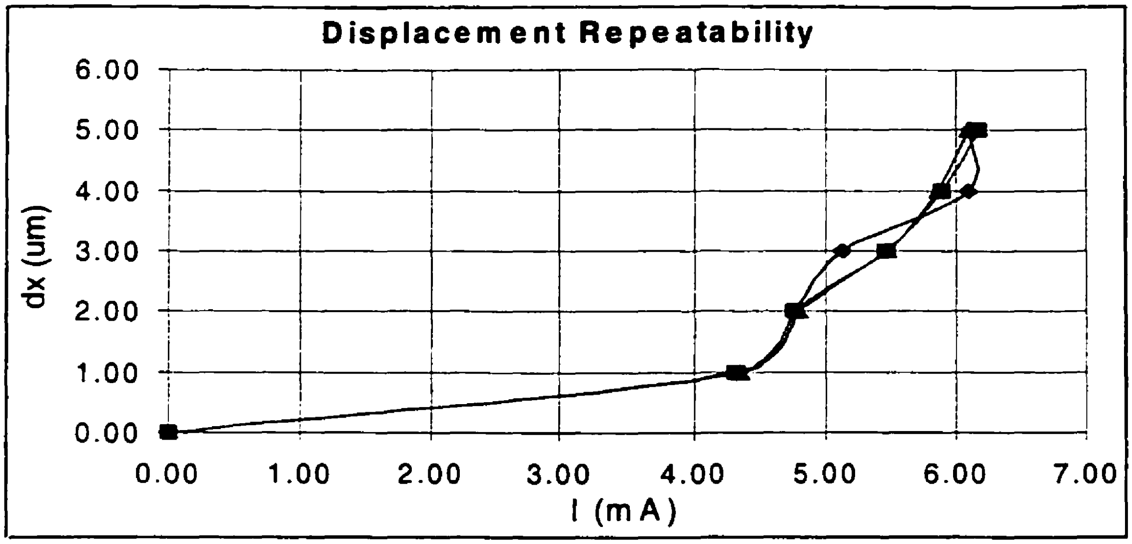

Figure 6.2: Three displacement cycles of the same lateral thermal actuator.

The lateral heatuator's motion is very repeatable to within 0.5 μm. This minor deviation is negligeable because it equals the uncertainty with which the deflection was measured. Three other independent thermal actuators were cycled to yield curves, that were superimposed upon those that were just presented, to examine the difference in performance between one another.

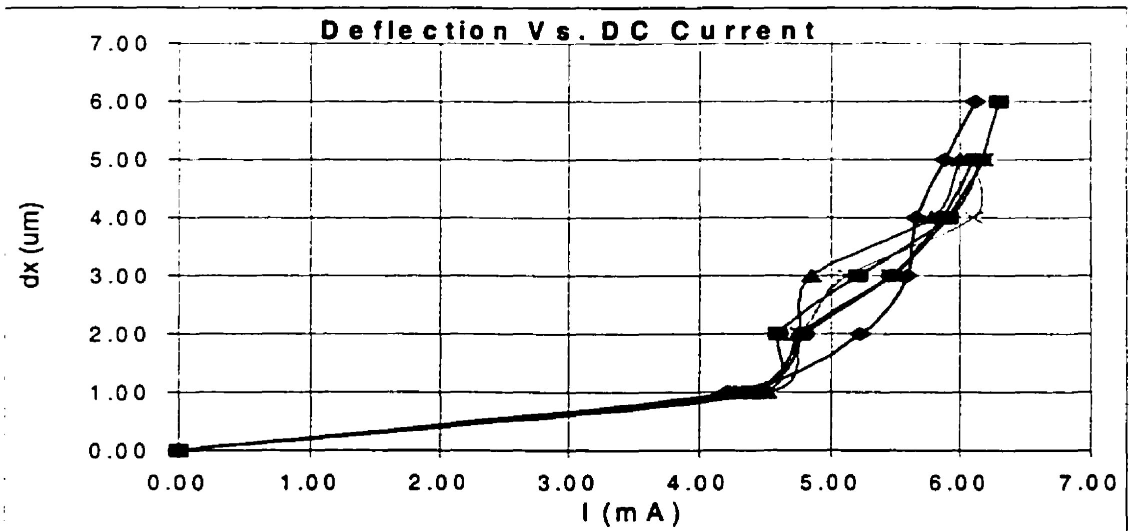

Figure 6.3: Six deflection versus current curves of four independent lateral thermal actuators.

As shown in Figure 6.3, the behaviors of these devices were comparable to one another despite the fact that the devices resided on different dies. However a given actuator may have required up to 0.5 mA more than another to reach the same point along their respective displacement curves. Consequently, controlling an array of actuators will become more challenging. Because a given device may draw more current than another, assuming that all thermal actuators of a common geometry require the same amount may backbend one device while another remains stationary. The average performance of the thermal actuators that were tested is shown in Figure 6.4.

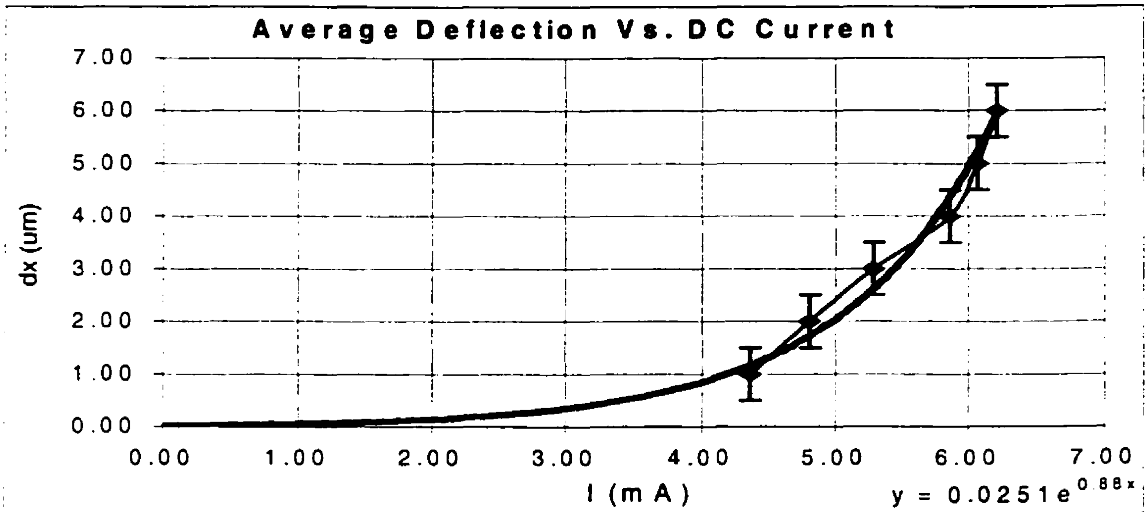

Figure 6.4: Best-fit average deflection versus applied current of four independent thermal actuators with an uncertainty of ±0.5 μm.

As per work published by Comtois et al. [1], the dynamic performance of a heatuator followed an exponential curve. Despite the correlation with what was observed, the expected maximum deflection of 10.0 μm was not reached. Instead, the lateral thermal actuator backbent after a 6.0 μm deflection and did not posess the same dynamic characteristics therafter. The latter was due to the 4.0 μm think hot arm and flexure. The formulae and expressions noted in [1] assume 2.0 μm thicknesses for the two aforementioned components. The added width increased the stiffness of the actuator. As a result, for the actuator's tip to deflect by a comparable amount, more current was required. Graphically, the exponentialy evolving curve was shifted to the right when a wider hot arm and flexure were used.

The observed maximum deflection of 6.0 μm was confirmed experimentally in [1] for devices with hot arms widths equal to 4.0 μm. To achieve the desired deflection of

10.0 μm, the widths of the hot arm and flexure must be reduced by a factor of two. As a result of the higher current requirements, the power consumed was as high as 34.0 mW, which was 9.0 mW greater than conventional thermal actuators [1], as illustrated in Figure 6.5b.

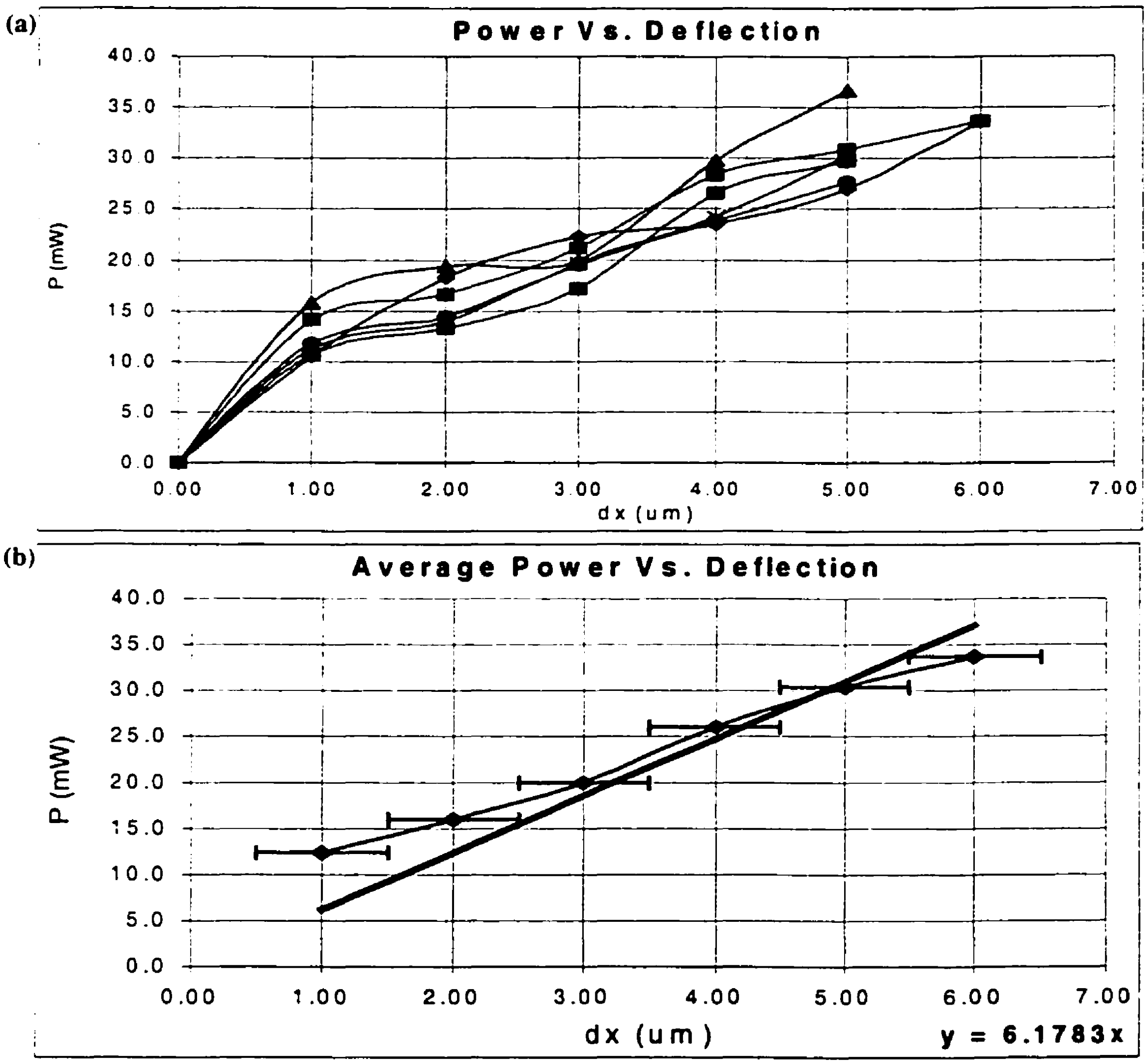

Figure 6.5: The (a) power and (b) average power dissipation versus deflection of four heatuators with an uncertainty of ±0.5 μm.

More importantly than power consumed is whether or not hysteresis was present. Earlier, an actuator was cycled one way only. But if an actuator is to be used reliably within a feedback mechanism, its motion must be equally predictable in either direction.

Based upon the results displayed in Figure 6.6, hysteresis did not exceed 0.5 μm. As a result, the lateral thermal actuator may be used within a feedback loop knowing that it is capable of returning to its last location with no significant amount of hysteresis.

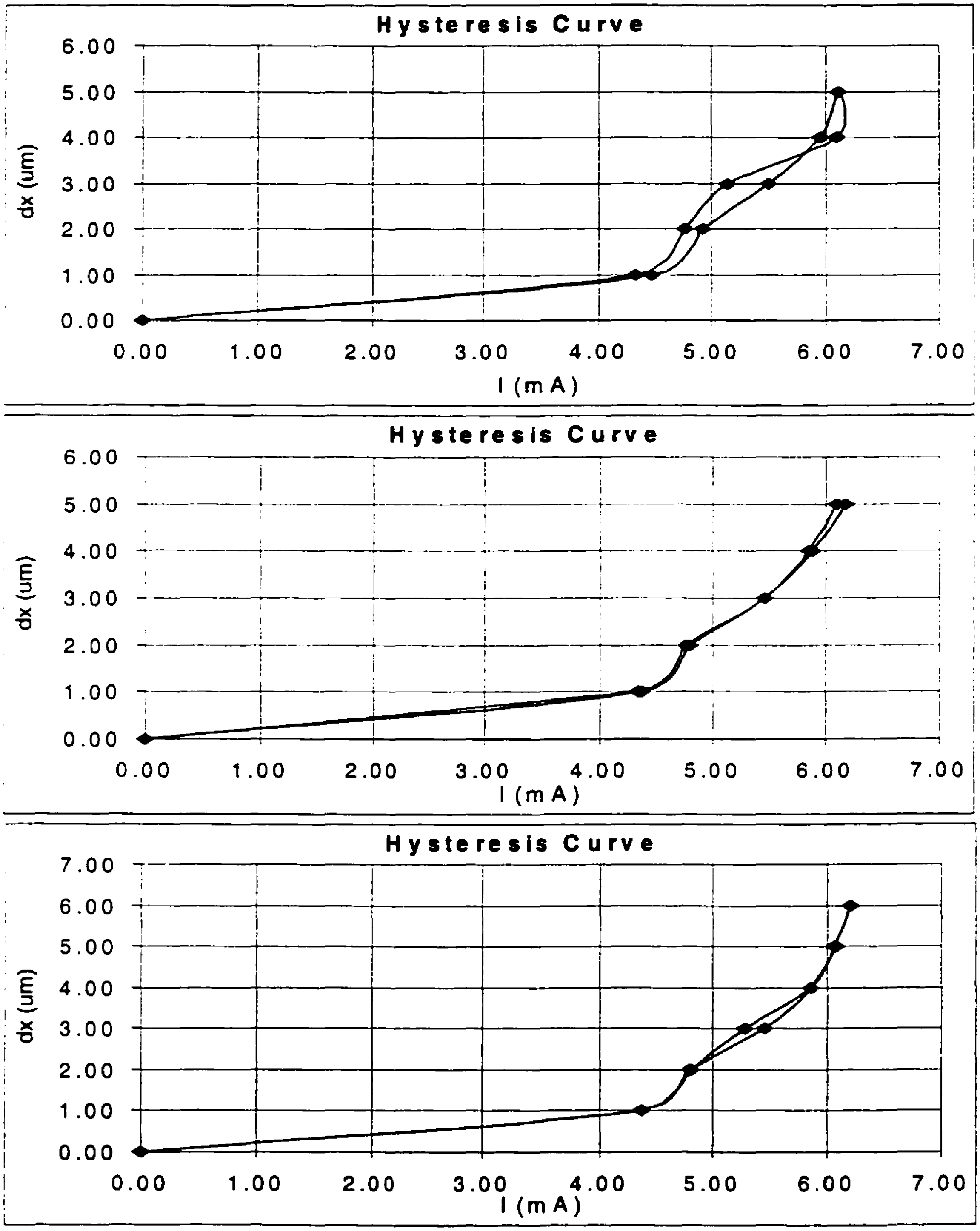

Figure 6.6: Hysteresis curves for three independent lateral thermal actuators.

Figure 6.7 and Figure 6.8 illustrate clearly the damaging effects of using an unmonitored amount of DC current. The dark speckled regions of the hot arm and flexure are indicative of misuse and were the areas that began to overheat before any other in the structure. The damage did not occur instantaneously but rather took a few seconds during which the hot arm was observed to emit a bright red glow. The local storage of heat may have been brought upon by stiction or by exceeding the device's load bearing ability, which inhibited motion. In the next section, observations regarding the thermal actuator's load bearing ability will be discussed.

(a) (b)

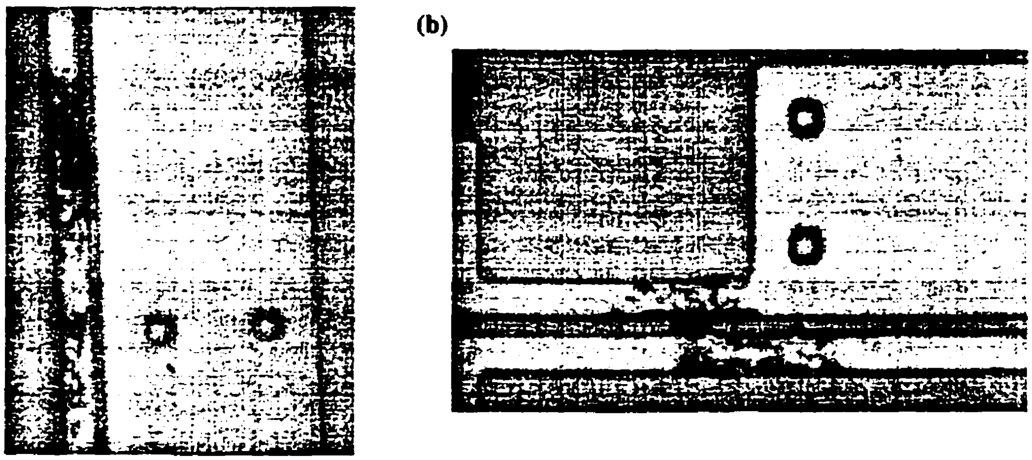

Figure 6.7: An overheated (a) hot arm and (b) both a hot arm and flexure that have begun to breakdown.

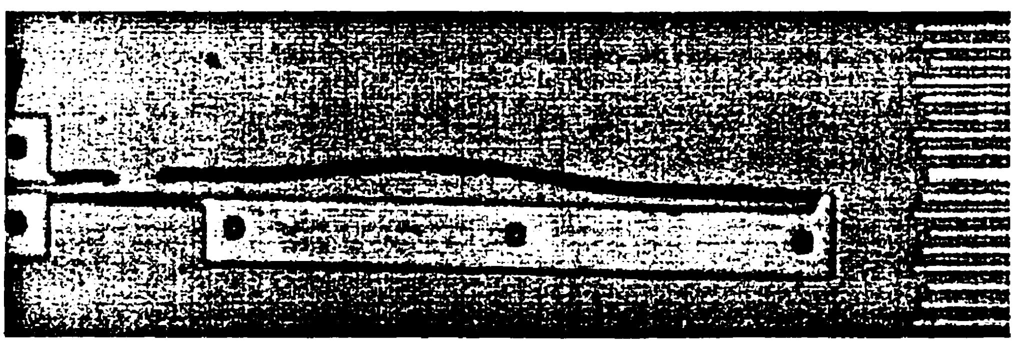

Figure 6.8: Thermal actuator with a broken hot arm due to thermally induced structural breakdown.

6.3 Rotational Motion (θ) in the X-Y Plane

Before the strategy for rotational motion is presented, a note must be made about the layout of all 2x2 lateral thermal actuator arrays. The reader may note that one pad on each side of any 2x2 array was left floating. The latter was an error that occurred during layout that was overcome by using two additional probes to provide the necessary electrical input to the DUT.

The center of rotation will be the geometrical center of the lenslet array. Rotation of such an object may be accomplished by firstly modeling its periphery as a series of point masses. When each of the latter is displaced by different increments along both the X and Y axes, a diagonal trajectory will result. By controlling the value of each point mass' incremental displacement along these two axes, and hence the diagonal path taken, the cumulative result will be a rotation of the targeted object as explained in Figure 6.9 below.

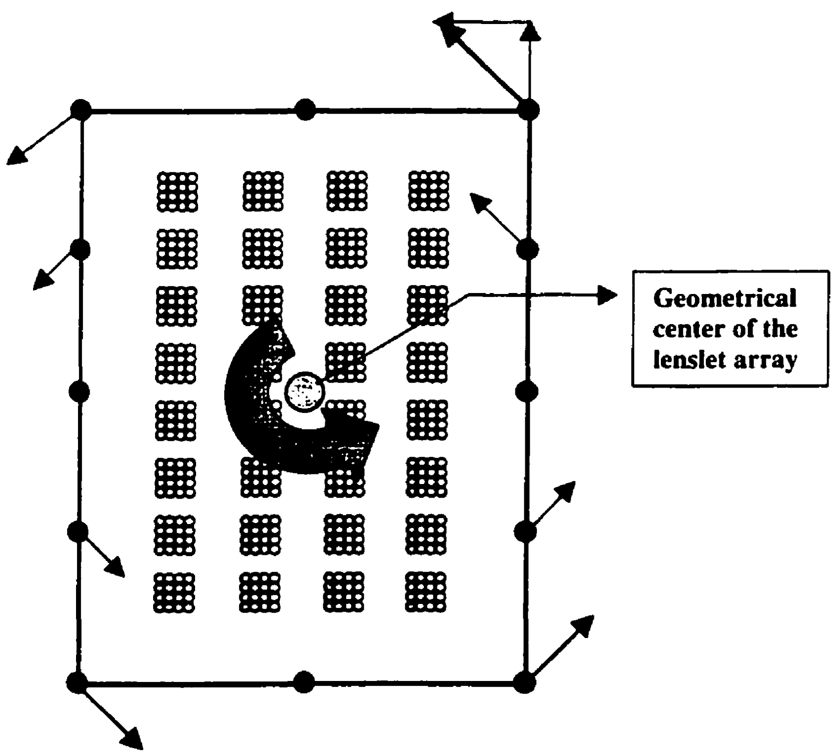

Figure 6.9: Implementation of rotational motion using controlled increments in X and Y to describe the proper diagonal trajectory as per the direction of rotation.

The length of the arrows is proportional to the contribution to rotation made by the MEMS at that location. For a given angle of rotation θ, the ratio of the arc length l, to the radial distance from the center of rotation r is constant. Therefore, as the point of motion approaches the center of the object, r will decrease. In order to preserve the value of θ, l must decrease also, which is represented by the length of the arrow.

Two options exist for transferring the lateral motion of a thermal actuator array to the load. The actuation arm could be attached to the load or be coupled to it through a hammer-like impacting motion as illustrated in Figure 6.10a and Figure 6.10b, respectively.

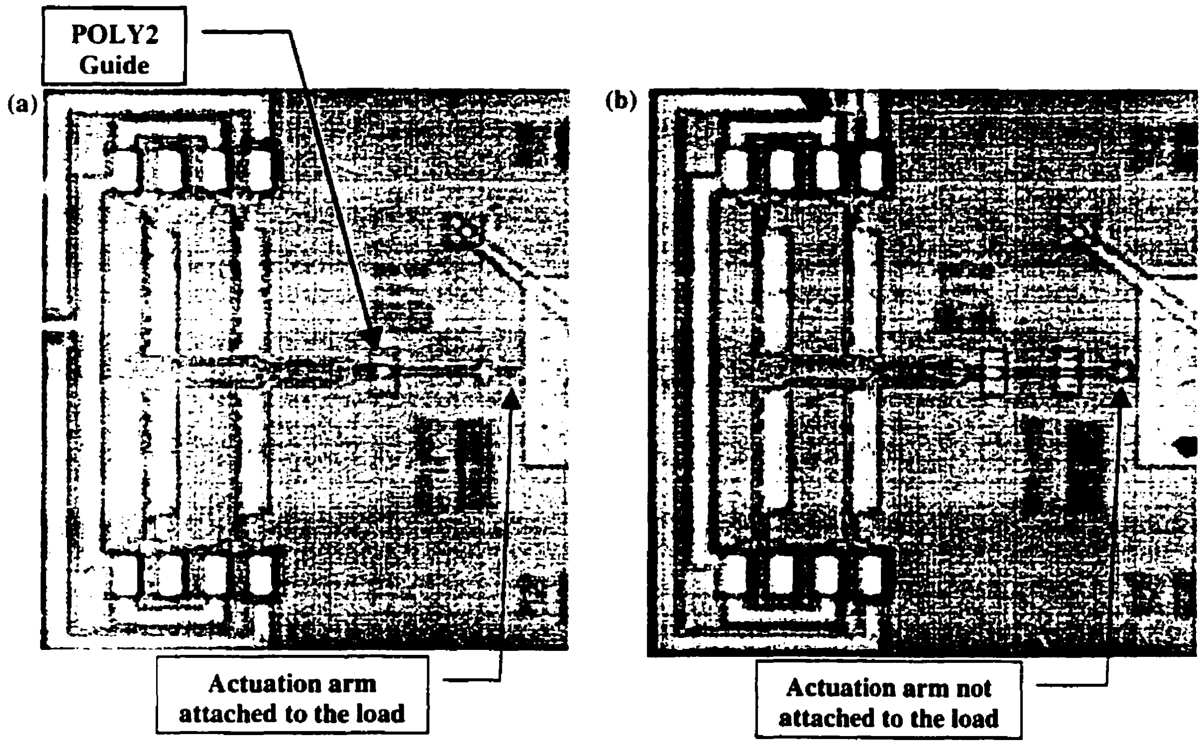

Figure 6.10: 2x2 thermal heatuator array with actuation arms that are (a) attached and (b) detached from the load.

Using the "impact drive" mechanism allows all the generated momentum to be coupled to the load instead of dissipating it to displace other inactive actuation arms that are attached to the load. Inactive devices will act as springs and cause the actuator array to require more power than would have been necessary otherwise.

The thermal actuator array was not successfully operated because the output force was not sufficient enough to drive an unloaded actuation arm in addition to overcoming stiction. The actuation arm was constructed using the first structural layer POLY1, and the arm guide using the second layer, POLY2. Two attempts were made to manually relieve the stiction between the actuation arm and the guide using probes as shown in Figure 6.11. In the first case, a probe pushed one arm and in the next attempt, two probe tips were used in the hope of displacing the actuation arm joint from under the guide. In fact, the difference in tone along the actuation arms is indicative of the magnitude of the pressure that was being applied by the probe tips.

Despite the significant force applied, the actuation arm remained immobile. The latter observation accounted for the thermal actuator arrays repeatedly overheating and breaking.

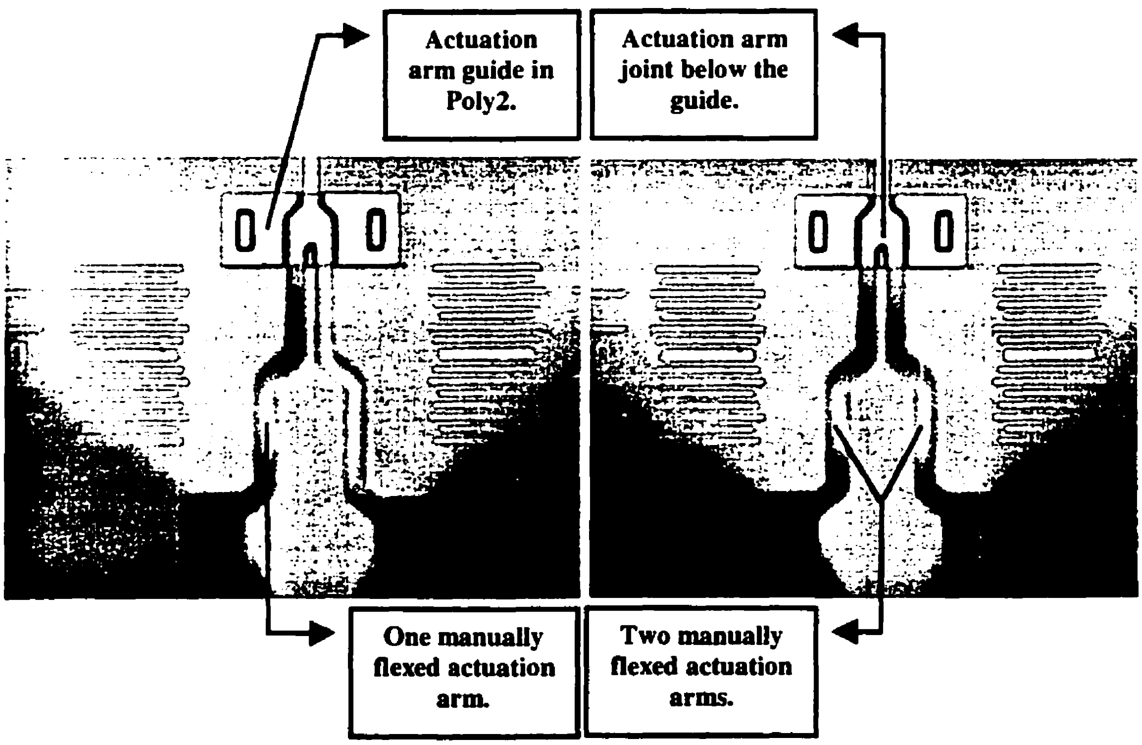

Figure 6.11: Actuation arms flexing under the lateral pressure due to stiction between the guide and the actuation arm joint.

6.4 Vertical Motion (Z)

Contrary to the lateral heatuator, the vertical heatuator responded much better to a voltage driven source. Therefore, all the plots were generated as a function of applied voltage rather than the customary DC current. The vertical actuator that is studied in this section is shown in Figure 6.12.

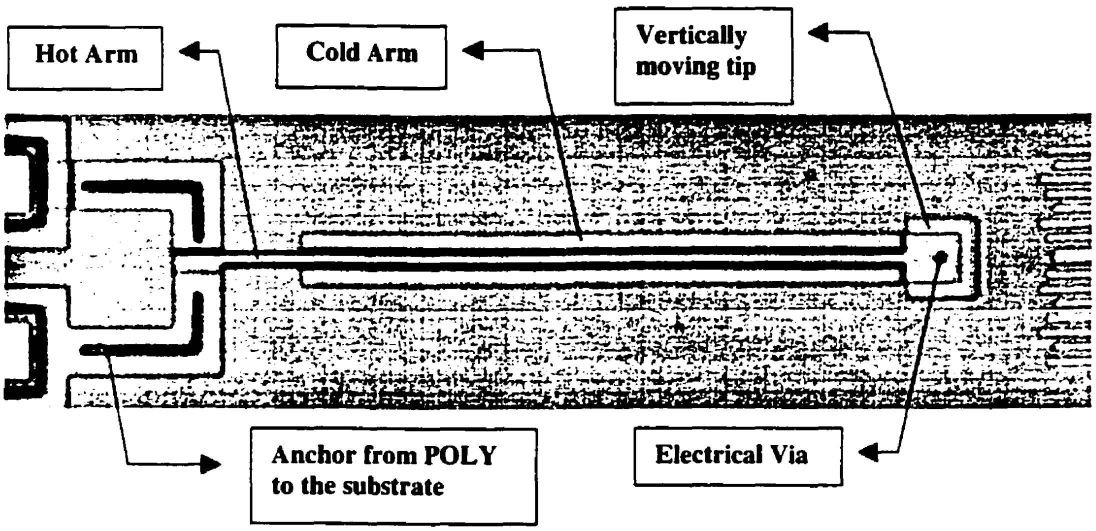

Figure 6.12: A picture of the vertical thermal actuator.

As per the original design discussed in section 4.4.2.2, the hot arm was located beneath the wider cold arm such that the hot arm deflected the cold arm upwards, away from the substrate. According to Figure 6.12, it would appear as though the hot arm was located above the cold arm. Due to the fact that the cold arm layer was 1.5 μm thick [2], the microscope's light passed through it and revealed the underlying hot arm. The latter was further confirmed by the fact that the anchors, which lay under structures and attached them to the substrate, were also visible as pointed out in Figure 6.12.

During testing, only one quarter of all randomly selected devices worked. In addition, as a vertical thermal actuator was cycled, backbending was observed to become increasingly significant. Consequently, the usable vertical deflection range decreased with every additional cycle. Unlike the lateral thermal actuator, backbending also occurred when the vertical actuator's position was maintained at a non-zero location along the positive Z-axis. Due to the inevitable onset of the latter, a given vertical actuator was cycled only once in an attempt to demonstrate the device's dynamic characteristics without allowing backbending to become a factor. The displacement versus applied voltage curves of four independent vertical thermal actuators are shown in Figure 6.13a followed by the best-fit average curve in Figure 6.13b. The evolution of these curves followed an exponential trend, as was the case with the lateral thermal actuators.

(a)

(b)

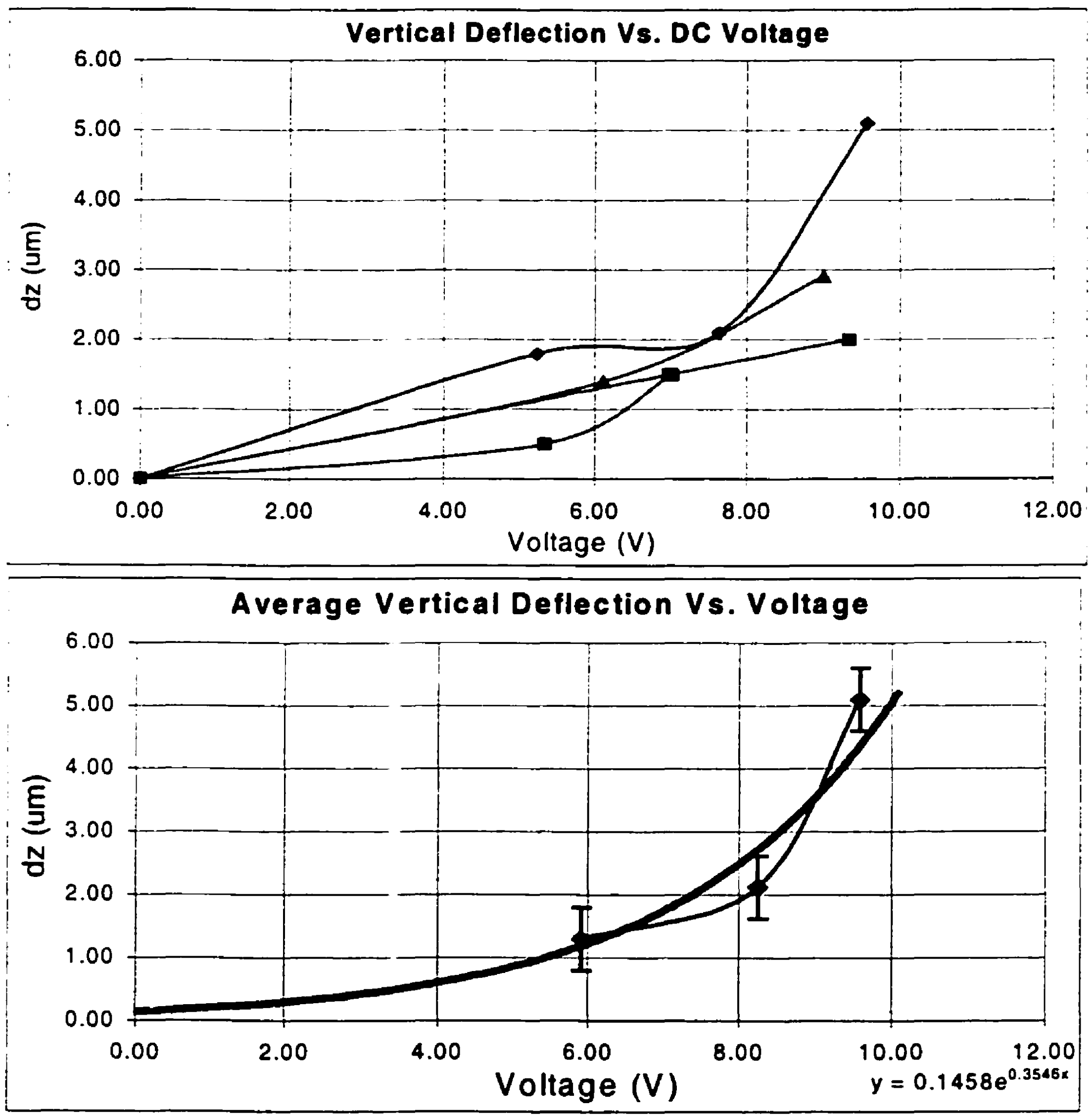

Figure 6.13: The (a) actual and (b) average vertical deflection versus applied voltage curves of four independent vertical thermal actuators with an uncertainty of ±0.5 μm.

The vertical deflection occurred slowly until approximately 7.0 V. The actuator then moved vertically by another 3.0 μm when an additional 2.6 V was applied. Sub-micron motion was readily observed but difficult to measure for reasons that will be mentioned shortly. The relative non-uniformity of the curves was due to the method used to measure the vertical displacement.

The vertical motion was measured using a "focus/defocus" method. For this method to work, two points of reference were required. The first had to be immobile, such that it could be used as an absolute focussing plane of reference and another that was located on the object, which was expected to go out of focus. The scale on the POLY0 layer was used as the absolute reference. The edge of the vertical actuator that was closest to the scale was used as the second reference object. The vertical actuator was deemed to have moved if and only if it went out focus. The focussing apparatus had a resolution of 1.0 μm [3]. Due to human error in conserving the original focus and clarity of the point of reference on the vertical actuator after it had moved vertically, the uncertainty of all measurements was ±0.5 μm.

Figure 6.14, on the next page, displays the three possible operating scenarios. In the first case, Figure 6.14a, the vertical actuator was at rest since both the stationary and mobile points of reference were on the same focal plane. An active vertical actuator is show in Figure 6.14b, where the mobile tip was considerably out of focus relative to the scale. After the vertical actuator was pushed to its deflection limit of 5.1 μm, it backbent as shown in Figure 6.14c. The mobile tip was in better focus than in the previously discussed case and since no voltage was applied, backbending was the only other explanation.

In order to produce a maximum vertical deflection of 5.1 μm, a single actuator was noted to require 9.58 V at 4.73 mA; approximately 45 mW. For a comparable deflection, almost twice as much power was required to move the vertical actuator than the lateral heatuator. The latter was further demonstrated when the best-fit linear functions for each device's average power consumption curves were compared. The ratio of the vertical actuator's average power consumption function, Figure 6.16, to that of the lateral actuator, Figure 6.5b, equaled 1.68. The power versus displacement curves for the four previously examined actuators are graphed in Figure 6.15.

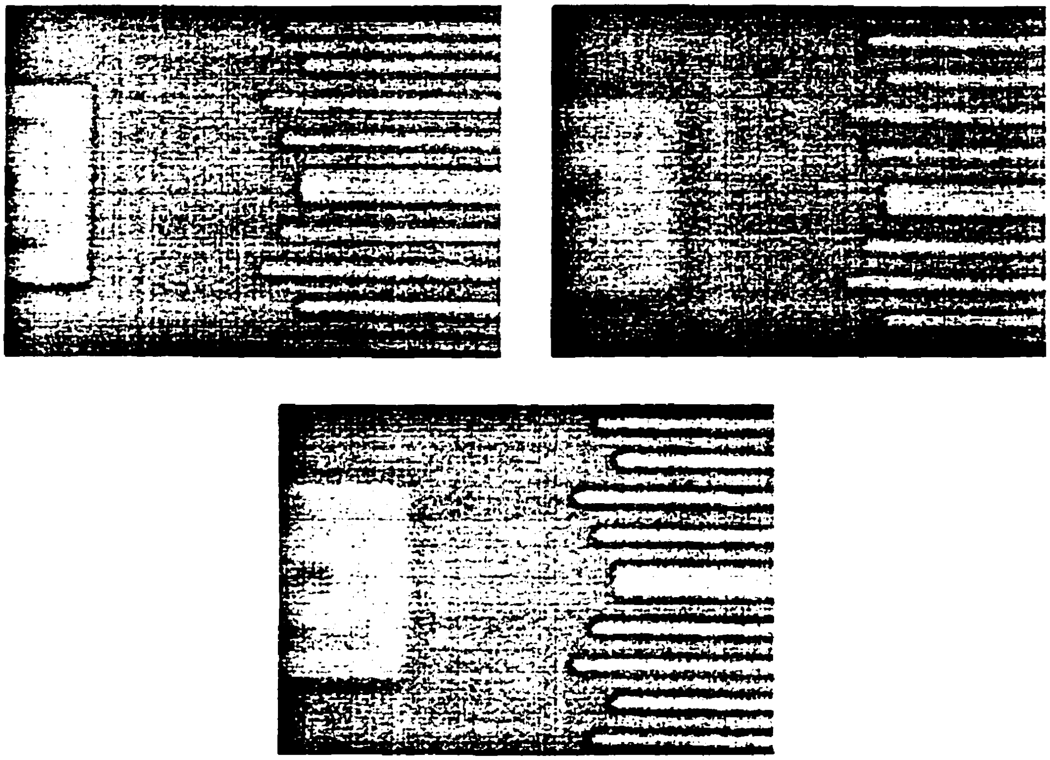

Figure 6.14: The vertical thermal actuator's tip (a) at rest, (b) deflected upwards, and (c) backbent.

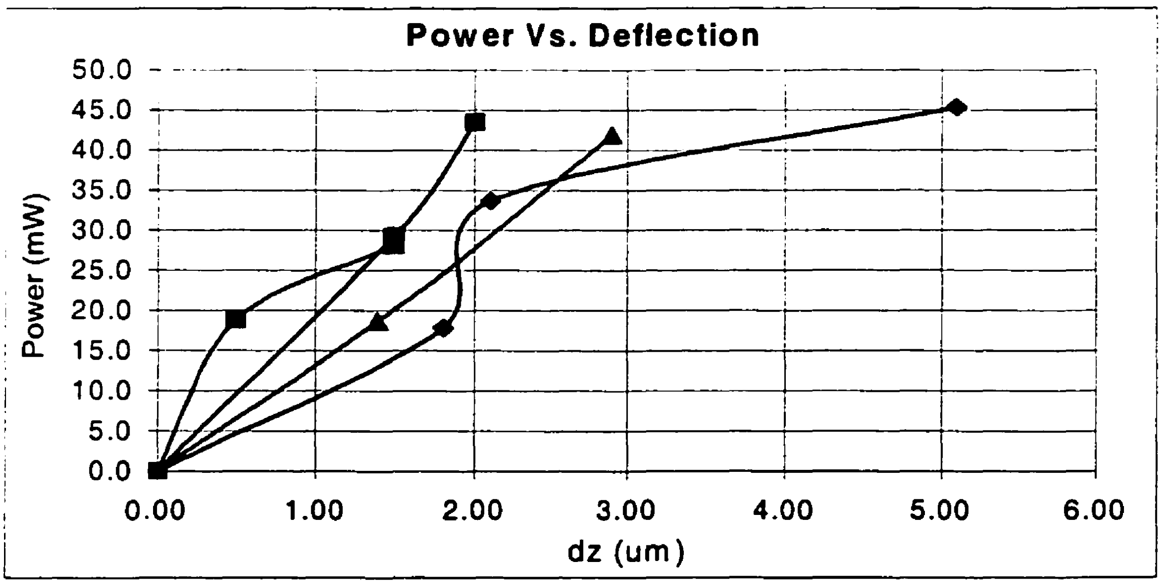

Figure 6.15: The power versus deflection curves of four independent vertical actuators.

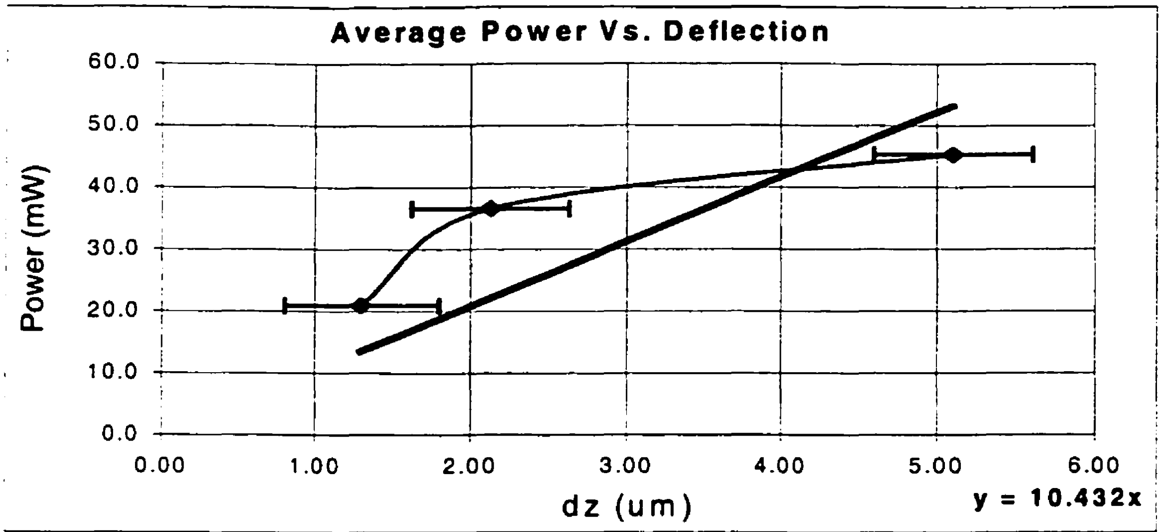

Figure 6.16: Average power versus deflection with an uncertainty of ±0.5 μm.

The average power consumption profile of a vertical thermal actuator was generated and is shown in Figure 6.16. The actuation voltage, and hence power consumed, increased rapidly initially. The 2.3 μm to 5.1 μm operating window was where the vertical actuator operated optimally. Within this operating region, the actuator's tip deflected an additional 1.0 μm per 2.67 mW on average as opposed to 1.0 μm per 16.8 mW in the 0.0 μm to 2.3 μm range of motion. On average, approximately 10.4 mW were required per additional micron of vertical displacement. Moreover, Figure 6.17 demonstrates that the vertical actuator had very little hysteresis.

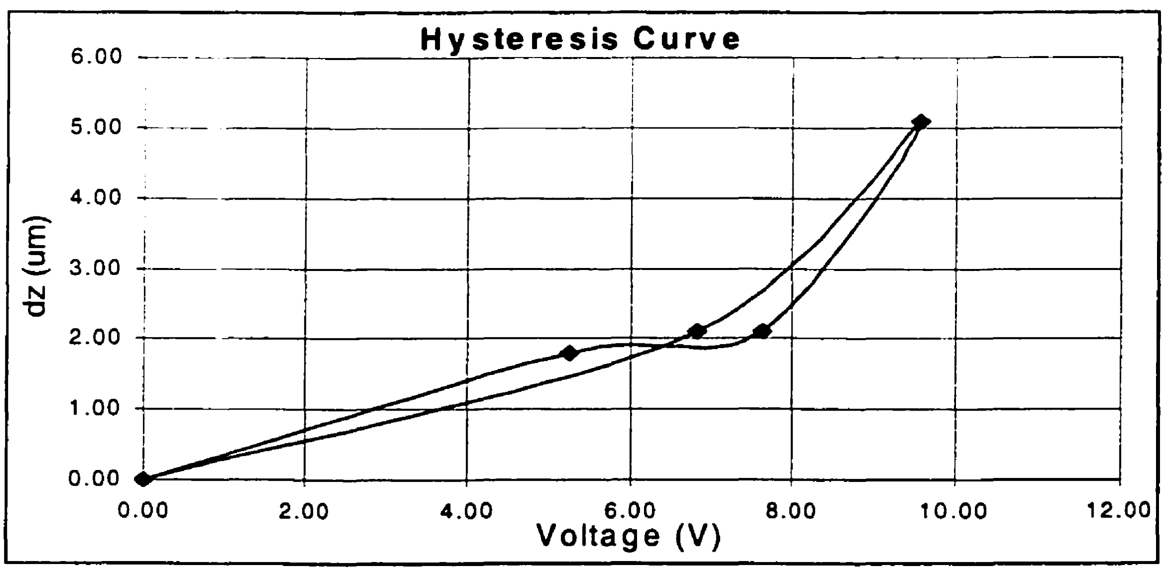

Figure 6.17: Hysteresis curve for a vertical thermal actuator after one cycle.

However, a vertical deflection of no more than 4.0 μm could be observed without backbending the actuator. This was due primarily to the heatuator's bi-level architecture. The gap between the hot and cold arms was 0.75 μm. This relatively smaller gap established a path of low thermal resistance between the actuator's two layers. Furthermore, the hot arm was in the middle of the cold arm's thermal conduction pathway to the substrate. Consequently, the heat generated in the hot arm migrated more easily to the cold arm and, in so doing, decreased the effective temperature difference between them. In order to correct the mathematical model of the vertical actuator, more experimental work must be conducted to determine the compounded effect(s) of geometrical variations of the cold arm and its location, relative to the hot arm, upon the device's efficiency.

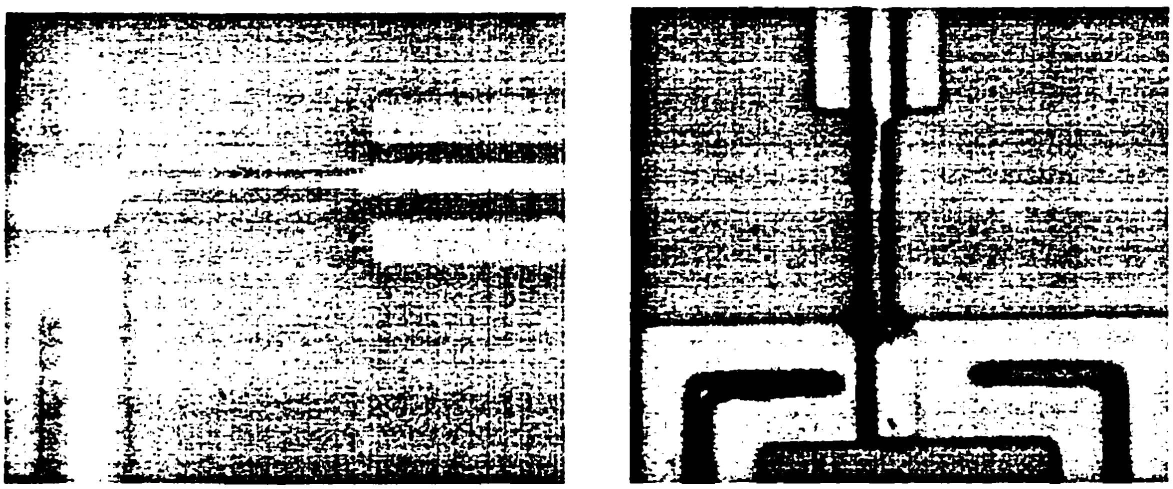

Figure 6.18: Hot arms and flexures that have become thinner due to overheating.

When the operating limits of the vertical actuator were exceeded, backbending and structural failure were observed. Figure 6.18 exemplifies the consequences of overheating the hot arm and flexure of a vertical thermal actuator. Due to overheating, the thinnest structures acted as fuses and slowly began to be consumed by heat. Had the power supply not been disabled, the structure would have been severed from the power supply pads permanently. Regardless, once the device's structure has decayed to this stage, it is no longer useful because the hot arm will burn up before it expands sufficiently to yield a useful deflection. Due to stiction, thermal energy accumulated once a voltage was applied. The result was the structural failure of the vertical thermal actuator under test due to overheating.

Further modeling and testing will reveal the currently unknown factors that influence the occurrence of backbending. The latter work will allow for the creation of an optimized vertical actuator geometry. Next, interferometric measurement techniques should be utilized to better evaluate the sub-micron vertical deflection capabilities and limitations of this actuator through fringe analysis [4]. After the device has been modeled and an accurate measurement method has been established, new designs based on the fundamentals of the vertical thermal actuators structure will emerge. They are expected to extend and advance the MEMS' optimal operating window from the 2.0 μm to 5.0 μm range into the 5.0 μm to 10.0 μm one.

6.5 References

1. J. H. Comtois, V. M. Bright, and M. W. Phipps, "Thermal Microactuators for Surface-Micromachining Processes", SPIE, vol. 2642, pp. 10-21, 1995.
2. D. A. Koester, R. Mahadevan, A. Shishkoff, and K. W. Markus, "MUMPS™ Design Handbook", Cronos Integrated Microsystems, p.10, May 1999.
3. Technical Data Sheet for the Finescope FS-60FC, Bulletin No. 1194-378. Ditributed by MTI Corporation for Mitutoyo Corporation.
4. H. Komatsu, "Interferometry: Principles and Applications of Two-Beam and Multiple-Beam Interferometry", Nikon Technical Bulletin, provided by Mr. Marcel Dubé of Nikon Canada Inc., 28 pages, 1989.

7 Lenslet Positioning Stages

7.1 The [X - Y – θ] Stage

7.1.1 Discussion

The displacement of macroscopic objects by microscopic mechanisms has been a challenging topic of research ever since MEMS were defined. Since then, schemes using directional force fields [1, 2, 3] and thermally actuated ciliary arrays [4] have been proposed. This chapter will present the development of an alternate positioning scheme by combining the decoupled actuation strategies that were presented in Chapter 6. Since the maximum deviation from the lenslet array's optimal location in the X-Y plane is 10 μm, the lateral actuators as well were designed to exhibit a maximum deflection of 10 μm.

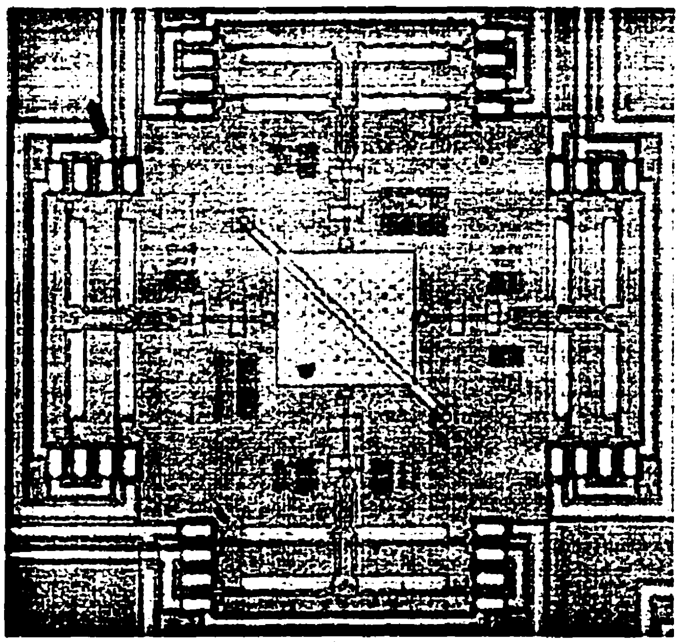

Figure 7.1: An X-Y-θ node that uses impact actuation.

Figure 7.1 shows a single X-Y-θ lenslet positioning "node" that utilizes a hammer-like impacting method to displace the central square support post. This structure will be duplicated at various locations along the periphery of the lenslet array in order to collectively support the 32.3 mg optical element; hence the term "node".

The square support was traversed by a beam, which was anchored on either end. It was used to ensure that the otherwise free plate would not move significantly during shipping. As was noted earlier, neither the desired maximum deflection nor the expected deflection was observed due to device geometry and stiction, respectively.

7.1.2 Implementation and Control Strategy

Alignment in the X-Y plane and rotationally will be accomplished using two of the lenslet's original features [5]. The fiducial marks, recalled in Figure 7.2, will allow the user to perform a coarse alignment when initially depositing the lenslet array onto the MEMS to within ±10 μm of its final aligned location.

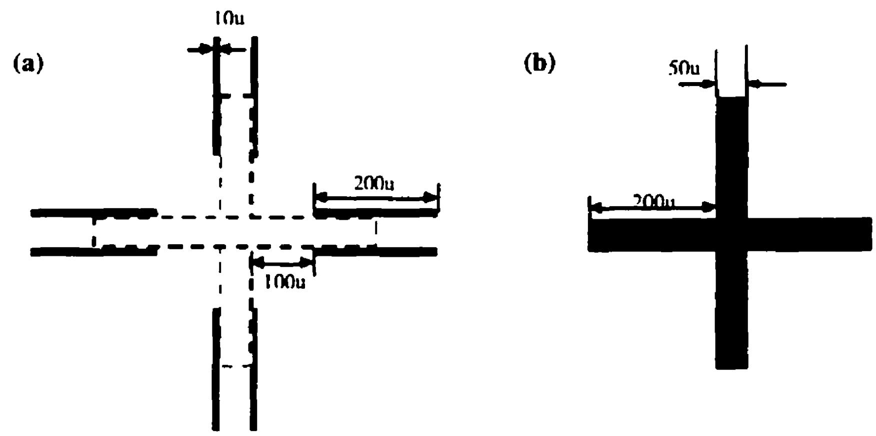

Figure 7.2: Fiducial marks as they appear on the (a) lens array and (b) optoelectronic chip. [5]

Next, the MEMS at the periphery of the lenslet array will take over and complete the alignment task. To accomplish this, the second alignment feature shown in

Figure 7.3 will be used. It is based upon landing a spot of light onto a target by using diffractive optics. Considering that the diameter of an individual lens of a given cluster on the lenslet array is 120 μm [5], each alignment spot will always fall onto its corresponding photo detector, after being redirected by an off-axis diffractive lens. Position-Sensitive Detectors (PSD) will replace each of the four targets on the original optoelectronic chip to enable feedback between it and the MEMS. PSDs with four quadrants should be used such that motion in both the X and Y planes may be monitored. The data required to compute the latter will be provided by four signal lines labeled, X_1, X_2, Y_1, and Y_2 as per Figure 7.4.

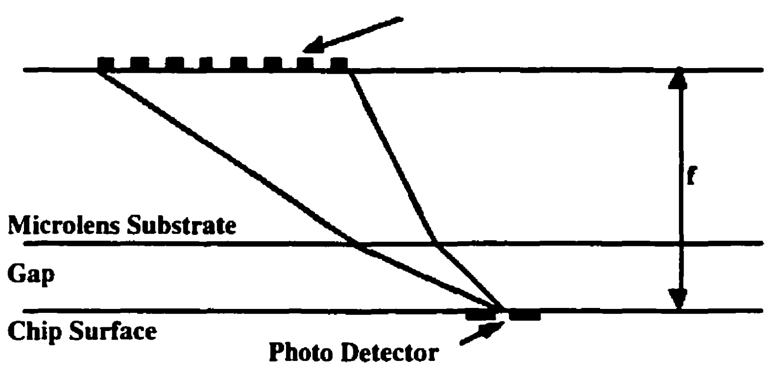

Figure 7.3: Single throw off-axis lens and photo detector. [based on 5]

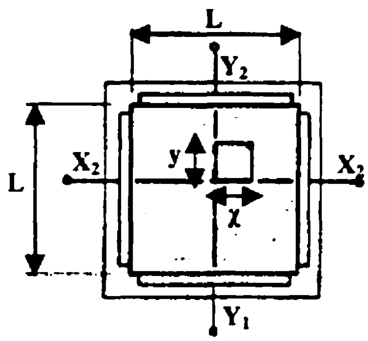

$$\frac{X_2 - X_1}{X_1 + X_2} = \frac{2\chi}{L}$$

$$\frac{Y_2 - Y_1}{Y_1 + Y_2} = \frac{2y}{L}$$

Figure 7.4: Position-Sensitive Detector (PSD). [6]

The control circuitry and feedback mechanisms will be based primarily upon signal comparison via subtraction. When the lenslet is moved in X, Y, and θ, the measured values for X_1, X_2, Y_1, and Y_2 will change accordingly. The objective of this closed loop control system is to position the diffracted spot of light onto the PSD's center by equating X_1 to X_2 and Y_1 to Y_2. When the MEMS are used, this iterative process will use the difference between the current set of values for X_1, X_2, Y_1, and Y_2 to calculate the spot's current location and to generate the necessary rectifying control signals.

The actuators will be active and respond to such control signals until the responses from each of the four quadrants of a given PSD, equal to within 5.0%, an experimentally determined nominal value. The latter reference will have had been previously determined experimentally following the fabrication of the optoelectronic chip.

This closed loop control mechanism was described solely in terms of its basic requirements and theoretical operation. Further characterization of the selected actuation schemes is necessary to adequately account for slippage, between the actuating devices and its target, in addition to non-linear effects such as hysteresis and backbending.

7.2 The [X - Y - θ – Z] Stage

7.2.1 Discussion

The position of the lenslet array along the Z-axis is critical to obtaining a collimated beam, originating from a VCSEL, and properly focussing an incoming beam onto a photo detector. The addition and control of a degree of freedom in the vertical direction (Z) will be accomplished by building upon the X-Y-θ stage of the last section. The forward bending vertical thermal actuator of section 4.4.2.2 functions but cannot be used confidently yet until it has been completely modeled and tested further. Although electrostatic means of controllably [7] displacing an object vertically exist, the buckling beam actuator [8] is recommended due to its simplicity and reliability.

7.2.2 Implementation and Control Strategy

The alignment of the lenslet array in the Z-direction will commence after alignment in the X-Y plane is complete. At that time, the vertical actuators will collectively move the lenslet array vertically. As a result, the lateral actuation nodes will no longer be in physical contact with the lenslet array. The closed loop control mechanism will be implemented with the aid of the interferometric features [5], which are show in Figure 7.5 and presented initially in section 2.2. Interference between incident plane waves and reflected waves, from a mirror on the chip's surface, will result with interference fringes. If the alignment is not good, the reflected wavefront will be non-planar and hence closely spaced interference fringes will be observed. On the other hand, widely spaced fringes will be observed if the alignment is good due to a planar reflected wavefront. A fringe analysis software package, such as Intelliwave [9], will capture and analyze these patterns. The resulting control signals will be electrically relayed back to the MEMS alignment system.

The system will be aligned in the Z-direction when the interference pattern consists of widely spaced fringes. Therefore the vertical alignment process will continue until the inter-fringe gap value of the captured interference pattern approximately equals a previously determined reference inter-fringe gap.

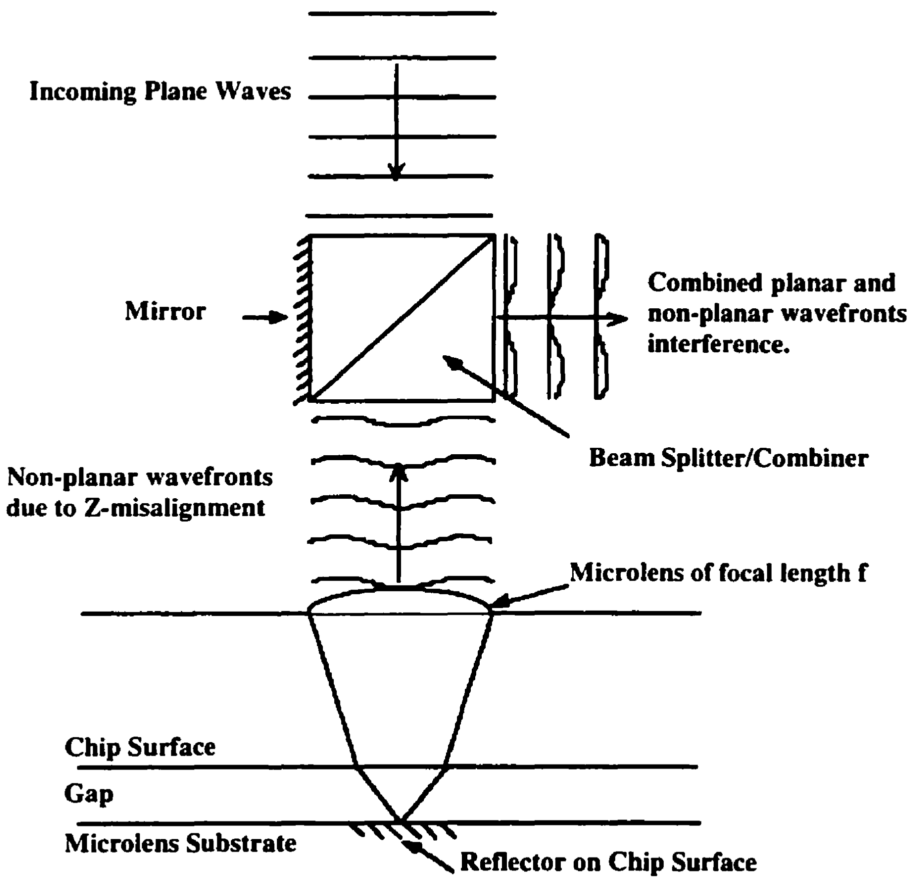

Figure 7.5: Arrangement for interferometric method [5].

7.3 Packaging and Assembly

7.3.1 Introduction

Packaging MEMS is fundamentally different from packaging microelectronics alone. Often, different microelectronic chips can be enclosed within a standard package. This effectively isolates them from the outside world. In contrast, MEMS may need to be in intimate contact with their surrounding environment, in order to react to a given external stimulus such as pressure, while simultaneously isolating other internal structures. There exist primarily three packaging philosophies: (1) Electronics First (University of California, Berkley), (2) MEMS in the Middle (Analog Systems), and (3) MEMS First (Sandia National Laboratories) [1].

Although the order in which the MEMS and the accompanying CMOS circuitry are fabricated may differ, electrically connecting both sub-systems is a common challenge. One proven solution is to extend the idea of Multichip Modules (MCM) to MEMS by replacing one of the chips in a CMOS MCM by a MEMS chip [11]. Depositing the MEMS onto the CMOS circuitry [11] or the electrical interconnects onto the dies [11, 12] have been successfully demonstrated. Alternatively, MEMS and the peripheral electronics may be joined by flip-chip soldering bonding the electronics onto the MEMS [13] or by riveting the two separately fabricated layers together [14].

In all three fundamental packaging approaches, the customer's needs greatly influence both the package's size and shape. On the other hand, the designer is responsible for addressing issues such as the choice of materials, thermal management, internal alignment, and the implementation of a suitable assembly process. Furthermore, immunity to noise, vibration, shock, and strain are particularly challenging concerns. Lastly, whether or not a MEMS is hermetically sealed and the choice of sealant is application dependent. Due to the complexity and interdependence of these issues, MEMS packages are highly customized and account for around 80% of the device's final cost. More importantly, packaging problems are linked to approximately 80% of the failures in production devices. [1,15] Therefore, for a Microelectromechanical System to find a niche in today's market, it must be well packaged in addition to operate reliably.

7.3.2 The Package and its Components

The schematic of the fully packaged lenslet aligning MEMS, shown in Figure 7.6, was presented for the first time in section 5.2. At this point, it is necessary to understand the role of each component in addition to discussing the inter-layer bonding strategy and the overall assembly process.

The proposed lenslet array alignment system is composed of four layers. Layer I is the lenslet array and layer IV contains the VCSEL/PD chip. Contact pads will be placed on the second layer's bottom surface and the fourth layer's top surface for reasons that will be discussed shortly. The required control circuitry will be placed on layers II and IV. Layers II and III both have rectangular cavities at their respective centers in order to establish a path, between the lenslet array and the VCSEL/PD chip, through which light may travel undisturbed.

The various MEMS that will go on to displace the lenslet array, will reside on the top surface of layer II. Layer III implements the spacer that is required to assist the vertically actuating MEMS in placing the lenslet array at its optimal location along the Z-axis. The need for a 40.0 ± 2.0 μm metallic spacer is due to the lenslet array's relatively large working distance. It is on the order of tens of microns, which is greater than the few microns worth of vertical motion a single MEMS device can provide.

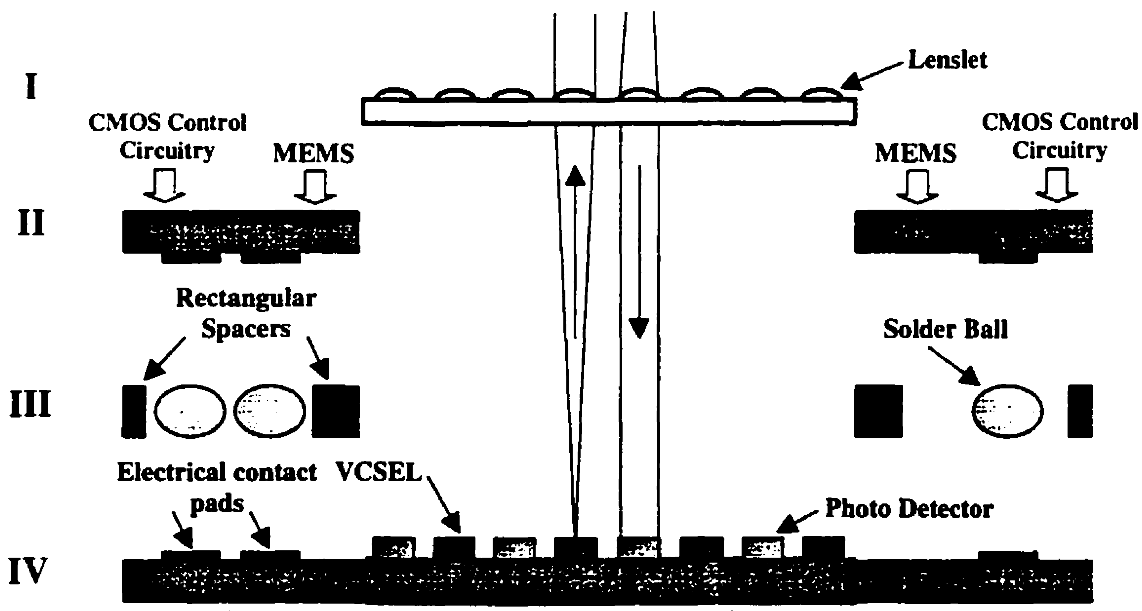

Figure 7.6: Schematic diagram of the proposed lenslet positioning MEMS.

The top view of layer III, in Figure 7.7 below, reveals that the two rectangular spacers are linked together. The latter two structures were bridged to facilitate the assembly process. Most importantly though, to the package's functionality, are the solder balls shown in Figure 7.6 and denoted by the abbreviation "SB" in Figure 7.7.

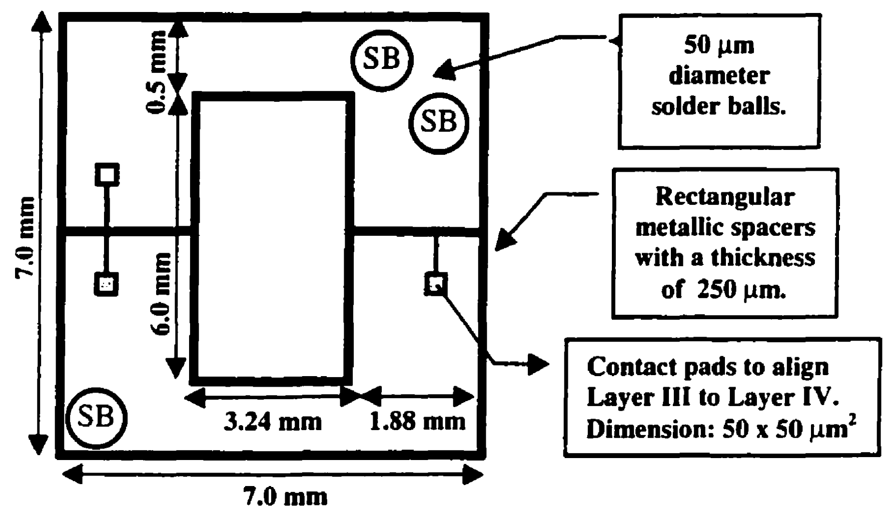

Figure 7.7: Top view of Layer III of the lenslet array positioning package.

7.3.3 Package Assembly Process

Techniques such as localized silicon fusion [16], eutectic bonding [16], and diffusion bonding [17] have been demonstrated but they do not electrically interconnect the aforementioned package's three last layers. They do not implement any type of interlayer alignment scheme either. Microscopic solder balls, on the other hand, have been used to align two parallel plates with sub micron precision by using solder surface tension as the assembly mechanism [18]. The solder self-alignment process is illustrated in Figure 7.8. The square contact pads present in Figure 7.7 allow the user to initially position layer III with layer IV. The solder balls were schematically shown to reside in layer III to clarify their role and emphasize their importance. In reality, they are initially deposited onto layer IV. The triangular arrangement of these solder balls aligns the combination of layers III and IV to layer II. The triangular formation is intentional since it explicitly implements a mechanical polarization scheme whereby only one orientation of each layer will result with all three solder balls landing upon their respective contact pads. In addition to precisely aligning the layers, the dried solder effectively attaches layers II, III and IV. After the solder has cooled, layers II through III will have had been aligned and solidly attached.

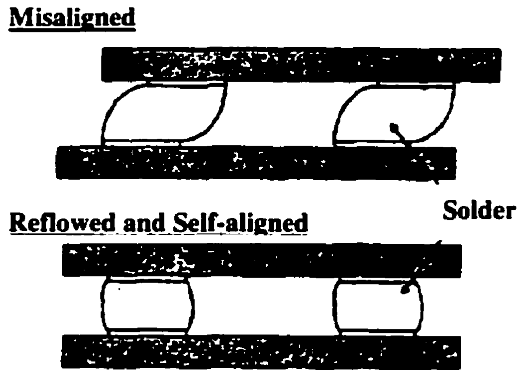

Figure 7.8: Illustration of the solder self-alignment mechanism. [18]

The decision to use solder balls justifies the presence of the contact or bond pads, mentioned earlier, on the bottom of layer II and the top of layer IV. By flip-chip bonding the layers onto one another, solder self-alignment can be implemented. These contact surfaces may be used as alignment nodes [19] but must also act as electrical connections [13] that will relay data, generated by control circuitry, between layers II and IV. Such a bonding mechanism has been developed by Oh et al. through the use of conductive polymers. Unlike solder, a polymer retains its shape when it is heated and does not flow like a liquid. The polymer bumps were rendered electrically conductive by using silver flake filler materials in the matrix of the polymer material. A high bump alignment precision of 5.0 μm is achievable while maintaining a low bonding temperature of 170°C. [20]

In order to avoid damaging the MEMS on surface II, a relatively low bonding temperature is desirable despite the fact that the MEMS structures were observed to withstand the epoxy curing process. It consisted of baking a MEMS populated chip carrier at 150°C for 30 minutes. By the same token, a low melting point for the solder will avoid the requirement of more costly epoxy curing hardware or services.

At this point, the lenslet array alignment MEMS package has been defined. All that remains is to deposit the lenslet array onto the MEMS and allow the control and feedback mechanisms complete the alignment process.

7.4 References

1. K. F. Böhringer, B. R. Donald, L. E. Kavraki, and F. Lamiraux, "Part Orientation with One or Two Stable Equilibria Using Programmable Force Fields" IEEE Transactions on Robotics and Automation, Vol. 16, No.2, pp. 157-170, April 2000.
2. J. E. Luntz, W. Messner, and H. Choset, "Discrete Actuator Array Vectorfiled Design for Distributed Manipulation", IEEE Transactions on Robotics and Automation, Vol. 3, pp. 2235-2241, May 1999.
3. J. E. Luntz, W. Messner, and H. Choset, "Open-Loop Orientability of Objects on Actuator Arrays", IEEE Transactions on Robotics and Automation, Vol. 3, pp. 2242-2248, May 1999.
4. J. W. Suh, R. B. Darling, K. F. Böhringer, B. R. Donald, H. Baltes, and G. T. A. Kovacs, "CMOS Integrated Ciliary Actuator Array as a General-Purpose Micromanipulation Tool for Small Objects", Journal of Microelectromechanical Systems, Vol. 8, No. 4, pp. 483-496, December 1999.
5. McGill University Photonic Systems Group, "Demo 1: Microlens array specifications and alignment features", February 1999.
6. J. J. Wagner, "Operating Principle and Features of PSD", Stanford University, http://www-cdr.stanford.edu/MADEFAST/catalogs/hamamatsu/psd-principle.html.
7. G. K. Fedder and R. T. Howe, "Multimode Digital \control of a Suspended Polysilicon Microstructure", Journal of Microelectromechanical Systems, Vol. 5, No. 4, pp. 283-297, December 1996.
8. T. Seki, M. Sakata, T. Nakajima, M. Matsumoto, "Thermal Buckling Actuator for Micro Relays", 1997 International Conference on Solid-State Sensors and Actuators, pp. 1153-1156 , June 16-19, 1997.
9. Intelliwave software package specifications by Engineering Synthesis Design Inc. http://www.engsynthesis.com/IntelliWaveFrame.htm, 2000.
10. C. B. O'Neal, A. P. Malshe, S. B. Singh, W. D. Brown, and W. P. Eaton, "Challenges in the Packaging of MEMS", International Symposium of Advanced Packaging Materials, pp. 41-47, 1999.

11. J. T. Butler, V. M. Bright, and J. H. Comtois, "Advanced Multichip Module Packaging of Microelectromechanical Systems", Proceedings of the International Conference on Solid-State Sensors and Actuators, pp. 261-264, 1997.
12. W. Daum, W. E. Burdick Jr., and R. A. Fillion, "Overlay High-Density Interconnect: A Chips-First Multichip Module Technology", Computer, Vol. 26, Issue 4, pp. 23-29, March 1993.
13. A. Singh, D. A. Horsley, M. B. Cohn, A. P. Pisano, and R. T. Howe, "Batch Transfer of Microstructures Using Flip Chip Solder Bonding", Journal of Microelectromechanical Systems, Vol. 8, No. 1, pp. 27-33, March 1999.
14. B. Shivkumar and C.-J. Kim, "Microrivets for MEMS Packaging: Concept, Fabrication, and Strength Testing", Journal of Microelectromechanical Systems, Vol. 6, No. 3, pp. 217-225, September 1997.
15. G. Beardmore, "Packaging for Microengineered Devices, Lessons from the Real World", IEE Colloquium on Assembly and Connections in Microsystems (Digest No. 1997/004), pp. 2/1 -2/8, 1997.
16. Y. T. Cheng, L. Lin, and K. Najafi, "Localized Silicon Fusion and Eutectic Bonding for MEMS Fabrication and Packaging", Journal of Microelectromechanical Systems, Vol. 9, No. 1, pp. 3-9, March 2000.
17. T. R. Christensen and D. T. Schmale, "A Batch Wafer Scale LIGA Assembly and Packaging Technique Via Diffusion Bonding", Twelfth IEEE International Conference on Micro Electro Mechanical Systems, pp. 476-481, 1999.
18. K. F. Harsh, P. E. Kladitis, M. A Michalicek, J. Zhang, W. Zhang, A. Tuantranont, V. M. Bright, and Y. C. Lee, "Solder Self-Alignment for Optical MEMS", Procceedings of the Twelfth Annual IEEE Lasers and Electro-Optics Society , Vol. 2, pp. 860-861, 1999.
19. N. Koopman, S. Nangalia, and V. Rogers, "Fluxless No-Clean Assembly of Solder Bumped Flip Chips", Proceedings of the 46th Electronic Components and Technology Conference, pp. 552-558, 1996.
20. K. W. Oh, and C. H. Ahn, "A New Flip-Chip Bonding Technique Using Micromachined Conductive Polymer Bumps", IEEE Transactions on Advanced Packaging, Vol. 22, No. 4, pp. 586-591, November 1999.

8 MEMS: Current Needs and Future Challenges

8.1 Motivation

Microelectromechanical Systems (MEMS) are currently diffusing into numerous industries while their candidature to resolve many unanswered engineering issues increases steadily. However, technological advances, instead of the global market, have provided the driving force behind the research of MEMS fundamental principles and fabrication processes [1]. Amidst the rapid progress and recognition the field of MEMS is experiencing, Mr. Trimmer asks, "why has human interest in the small taken so long to develop?"[2] The answer to this question points out both the weaknesses, such as the low yield of current microfabrication techniques, while highlighting the areas of research and development that must be supported if MEMS are to thrive in today's market and tomorrow's economy.

In order to further pinpoint the limitations of current MEMS technologies, be it fabrication or otherwise, it is imperative to specify profitable short-term commercial applications [3]. Due to the wide applicability of MEMS [4,5] , it becomes very tempting for a young company, created to satisfy these newly identified niches, to be over-aggressive by over-extending their research and development capabilities to satisfy the specific needs of one customer as opposed to those of a global economy. These startups must focus their research on a specific product instead of producing numerous marginally functional ones. [4] In any case, a good product alone does not guarantee a company's survival. Rather, fulfilling the need(s) of a large audience and good marketing are required.

8.2 Commercializing MEMS

The obstacles to successfully introducing a MEMS device into the market can be placed in one of two categories, business or technological. Business related difficulties must be addressed immediately if MEMS-related service providers are to recognize the unique needs of the MEMS industry and if MEMS designers are to acknowledge the need for proper marketing. MEMS do not follow a "VLSI mindset" because there is no single fundamental MEMS device or component from which all subsequent devices can be formed. Every MEMS is unique, much like an Application Specific Integrated Circuit (ASIC), and requires specialized treatment. [6]

Two key business issues that are directly affected, by this characteristic feature of all MEMS, are time-to-market and market volume. Because the development cycle tends to be long, due in part to a lack of specialized hardware and services, the time-to-market of existing MEMS products tends to be about ten years. As a result, the incurred development costs can only be recovered if a large market exists. Although such a market is difficult to locate, it is not fictitious because the original design process was set in motion by the identification of a need. Hence the necessity for a reinforcing entity that can assist MEMS designers with introducing a MEMS product into the market within a shorter time frame is justified.

The MEMS industry infrastructure must be tailored to overcome the adverse affects of a Microelectromechanical Systems' distinctiveness upon the two previously mentioned business issues. [6] To enable the mass-production of MEMS [7], companies that provide MEMS-specific services [8] must be created. Next, the development of more robust fabrication processes through reliability studies should be conducted [9,10]. In order to satisfy the handling requirements of a mainstream fabrication line, enhanced packaging [11,12] and testing [13,14] techniques become necessary. Most importantly, an adequate understanding of the theory governing the interactions between the various energy domains and the variables to be measured, in the surrounding environment, must be acquired if well modeled MEMS CAD packages [15] are to be made available.

Within the next ten years, the definition of a Microelectromechanical System will evolve from one where one packaged device relays measured data to one where millions of networked inter-communicating MEMS send collected and analyzed data, from a large area, to a user. These are known as Distributed Sensor Networks (DSN) [17, 18]. Aside from functioning correctly, these microscopic instruments must process, synchronize, and communicate data [16]. Next, the location of each MEMS must be determined either relative to one another or in an absolute fashion via feedback from the device itself. Thirdly, power management is an issue that each MEMS will have to address independently. Lastly, the determination of a useful deployment strategy will depend directly upon the proper characterization of the packaging, be it hand-placed, air-dropped, or munition-launched. [18]

When these future applications and needs are considered, the current barriers associated with improving fabrication processes, service availability, packaging technologies, and CAD tools are put into perspective. The MEMS industry must be granted access to services and technologies that will open the doors for intense research and development. These efforts will in turn yield solutions that will eventually make the fabrication, testing, and packaging of a MEMS device as repeatable and dependable as that of a conventional CMOS chip.

8.3 References

1. A. B. Frazier, R. O. Warrington, and C. Freidrich, "The Miniaturization Technologies: Past, Present, and Future", IEEE Transactions of Industrial Electronics, Vol. 42, No. 5, pp. 423-430, 1995.
2. W. Trimmer, "Grand in Purpose Insignificant in Size", Proceedings of Micro Electro Mechanical Systems, IEEE, Tenth Annual International Workshop on MEMS, pp. 9-13, 1997.
3. H. Fujita, Proceedings of Micro Electro Mechanical Systems, IEEE, Tenth Annual International Workshop on MEMS, pp. 1-7, 1997.
4. K. Peterson, "What Lies Ahead?", 8th International Conference on Solid-State Actuators, and Eurosensors IX, pp. 894-897, 1995.
5. K. D. Wise, "Microelectromechanical Systems: Interfacing Electronics to a Non-Electronic World", International Electron Devices Meeting, pp. 11-18, 1996.
6. E. Peeters, "Challenges in Commercializing MEMS", IEEE Computational Science and Engineering , Vol. 4 Issue 1, pp. 44-48, 1997.
7. K. W. Markus, "Developing Infrastructure to Mass-Produce MEMS", IEEE Computational Science and Engineering , Vol. 4 Issue 1, pp. 49-54, 1997.
8. W. Ehrfeld, V. Hessel, K.-P. Kämper, M. Lacher, A. Picard, M. Schmidt, and Ch. Schulz, "Market Oriented Development and Production of Microdevices", Proceedings of the 19th International Conference on Microelectronics, Vol. 1, pp. 71-79, 1997.
9. D. M. Tanner, "Reliability of Surface Micromachined MicroElectroMechanical Actuators", Proceedings of the 19th International Conference on Microelectronics, pp. 97-104, May 2000.
10. D. M. Tanner, J. A. Walraven, K. A. Helgesen, L. W. Irwin, D. L. Gregory, J. R. Stake, and N. F. Smith, "MEMS Reliability in a Vibration Environment", IEEE Proceedings of the International Reliability Physics Symposium, pp. 139-145, 2000.
11. C. B. O'Neal, A. P. Malshe, S. B. Singh, W. D. Brown, and W. P. Eaton, "Challenges in the Packaging of MEMS", International Symposium of Advanced Packaging Materials, pp. 41-47, 1999.

12. G. Beardmore, "Packaging for Microengineered Devices, Lessons from the Real World", IEE Colloquium on Assembly and Connections in Microsystems (Digest No. 1997/004), pp. 2/1 -2/8, 1997.
13. S. Mir, B. Charlot, and B. Courtois, "Extending Fault-Based Testing to Microelectromechanical Systems", Proceedings of the European Test Workshop, pp. 64-68, 1999.
14. B. Courtois, J. M. Karam, S. Mir, M. Lubaszewski, V. Szekely, M. Rencz, K. Hofmann, and M. Glesner, "Design and Test of MEMS", Proceedings of the Twelfth International Conference on VLSI Design, pp. 270-275, 1999.
15. S. D. Senturia, "CAD Challenges for Microsensors, Microactuators, and Microsystems", Proceedings of the IEEE, Vol. 86, No. 8, pp. 1611-1626, 1998.
16. L. E. Larson, "Microwave MEMS Technology for Next-Generation Wireless Communications – Invited Paper", IEEE International Microwave Symposium, Vol. 3, pp. 1073 –1076, 1999.
17. A. A. Berlin and K. J. Gabriel, "Distributed MEMS: New Challenges for Computation", IEEE Computational Science and Engineering , Vol. 4 Issue 1, pp. 12-16, 1997.
18. J. Agre and L. Clare, "An Integrated Architecture for Cooperative Sensing Networks", Computer, Vol. 33, Issue 5, pp. 106-108, 2000.

9 Conclusions

This thesis has presented various MEMS manufacturing technologies and actuation strategies while focussing on the design of an X-Y-θ and X-Y-θ-Z MEMS based alignment system. To accomplish this, actuators that will displace the lenslet in the X, Y, and Z directions were specified. Actuators were designed, manufactured using the MUMPs™ fabrication process, and tested. Thermal actuators were initially chosen and tested but the required maximum deflection of 10 μm was not observed due to a flexure that was 4.0 μm thick, rather than 2.0 μm. Regardless, stiction prevented motion when the thermal actuators were used in an array. A novel thermally operated vertical actuator was tested and is predicted to be capable of moving the optical element along the positive Z-axis. It exhibited backbending and consumed 45 mW when it was deflected to a vertical maximum of 5.1 μm. The forward bending vertical thermal actuator shows great promise because it is expected to displace significant loads in a repeatable and controllable fashion. In fact, both lateral and vertical actuators showed no important amount of hysteresis when cycled while routinely moving with sub-micron precision.

The proposed MEMS alignment assembly will consist of primarily four functional layers. The first is the lenslet array and the second layer will contain the lenslet positioning MEMS. It will be electrically and structurally aligned to the underlying third and fourth layers by solder bumps. The third layer will be a metallic spacer that will assist the vertical actuators in placing the lenslet array at the appropriate focal plane. The fourth layer contains the optoelectronic chip and the control circuitry that will govern the operation of the MEMS based alignment system.

The MEMS and any local CMOS circuitry on the second layer will be fabricated via the IMEMS process. It allows both mechanical and electrical structures to be simultaneously and reliably manufactured. Thermal actuation techniques in general require a relatively high amount of power to displace a load and consume energy so long as they are in a deflected position. Consequently, the X-Y-θ and X-Y-θ-Z lenslet array alignment assemblies must be glued once the lateral and vertical actuators have reached a point of operational equilibrium in order to justify the use of thermal actuation methods.